A PKN HYDRAULIC FRACTURE MODEL STUDY AND FORMATION PERMEABILITY DETERMINATION

A Thesis

by

JING XIANG

Submitted to the Office of Graduate Studies of
Texas A&M University
in partial fulfillment of the requirements for the degree of

MASTER OF SCIENCE

December 2011

Major Subject: Petroleum Engineering

A PKN HYDRAULIC FRACTURE MODEL STUDY AND FORMATION PERMEABILITY DETERMINATION

A Thesis

by

JING XIANG

Submitted to the Office of Graduate Studies of
Texas A&M University
in partial fulfillment of the requirements for the degree of

MASTER OF SCIENCE

Approved by:

Chair of Committee,	Ahmad Ghassemi
Committee Members,	Stephen A. Holditch
	Vikram Kinra
Head of Department,	Stephen A. Holditch

December 2011

Major Subject: Petroleum Engineering

ABSTRACT

A PKN Hydraulic Fracture Model Study and Formation Permeability Determination.

(December 2011)

Jing Xiang, B.S., China University of Petroleum

Chair of Advisory Committee: Dr. Ahmad Ghassemi

Hydraulic fracturing is an important method used to enhance the recovery of oil and gas from reservoirs, especially for low permeability formations. The distribution of pressure in fractures and fracture geometry are needed to design conventional and unconventional hydraulic fracturing operations, fracturing during water-flooding of petroleum reservoirs, shale gas, and injection/extraction operation in a geothermal reservoir. Designing a hydraulic fracturing job requires an understanding of fracture growth as a function of treatment parameters.

There are various models used to approximately define the development of fracture geometry, which can be broadly classified into 2D and 3D categories. 2D models include, the Perkins-Kern-Nordgren (PKN) fracture model, and the Khristianovic-Geertsma-de. Klerk (KGD) fracture model, and the radial model. 3D models include fully 3D models and pseudo-three-dimensional (P-3D) models. The P-3D model is used in the oil industry due to its simplification of height growth at the wellbore and along the fracture length in multi-layered formations.

In this research, the Perkins-Kern-Nordgren (PKN) fracture model is adopted to simulate hydraulic fracture propagation and recession, and the pressure changing history. Two different approaches to fluid leak-off are considered, which are the classical Carter's leak-off theory with a constant leak-off coefficient, and Pressure-dependent leak-off theory. Existence of poroelastic effect in the reservoir is also considered.

By examining the impact of leak-off models and poroelastic effects on fracture geometry, the influence of fracturing fluid and rock properties, and the leak-off rate on the fracture geometry and fracturing pressure are described. A short and wide fracture will be created when we use the high viscosity fracturing fluid or the formation has low shear modulus. While, the fracture length, width, fracturing pressure, and the fracture closure time increase as the fluid leak-off coefficient is decreased.

In addition, an algorithm is developed for the post-fracture pressure-transient analysis to calculate formation permeability. The impulse fracture pressure transient model is applied to calculate the formation permeability both for the radial flow and linear fracture flow assumption. Results show a good agreement between this study and published work.

DEDICATION

To my Family

ACKNOWLEDGEMENTS

I would like to express my deep and sincere gratitude to my advisor, Dr. Ahmad Ghassemi, for his support, guidance, encouragement, and patience, throughout the completion of this research project. Dr. Ghassemi introduced me to the field of petroleum rock mechanics and provided me with the opportunity to learn and do research on hydraulic fracturing. I especially thank him for his patience in carefully reviewing the manuscript of this thesis. I also thank Dr. Stephen A. Holditch and Dr. Vikram Kinra for kindly serving as committee members and reviewing the thesis.

I would also like to thank my family. They supported me throughout the course of completing my study. Thanks also go to my friends and colleagues, and the department faculty and staff, for making my time at Texas A&M University a great experience. I would especially like to thank my friends and colleagues, including Jun Ge, Jian Huang, and Chakra Rawal. I really appreciate their help with my study.

I thank God for empowering and guiding me throughout the completion of the degree.

NOMENCLATURE

a = the crack half length

A = the vertical cross-sectional area

c = the reservoir diffusivity coefficient

C_{fD} = the dimensionless fracture conductivity

C_l = fluid leak-off coefficient

C_p = the compressibility of the pore and pore fluid system

c_w = the ‘diffusivity coefficient’

E = the Young's modulus of the material

E' = $E/(1-\nu^2)$

erf = the error function

$E_1(x)$ = the exponential integral

$f(t^*)$ = an evolutional function

G = the shear modulus

h_f = the fracture height

k = the permeability

K = the constitutive constant for a power law fluid

k_f = the fracture permeability

K_{Ic} = the fracture toughness for mode I

K_{IIc} = the fracture toughness for mode II

K_{IIIc} = the fracture toughness for mode III

L = the fracture half length

ΔL = the small segment length

$\dot{L}$ = the length change rate

L_D = dimensionless fracture length

L_e = the equivalent fracture length

L^k = the fracture length at time t^k

$\dot{L}^k$ = the change rate of the fracture length at time t^k

L^{k+1} = the fracture length at time t^{k+1}

$\dot{L}^{k+1}$ = the change rate of the fracture length at time t^{k+1}

L_m = the maximum length

M_c = the fracture compliance

m_p = the slope of G-function curve

n = the power law index /the number of source segments

N = the number of point nodes

p = the net stress

Δp = the net pressure

p_D = dimensionless fracture pressure

p_f = the fluid pressure

p_i^k = the fracture pressure at point θ_i at time t^k

p_i^{k+1} = the fracture pressure at point θ_i at time t^{k+1}

p_i = the intercept pressure

p_0 = the virgin pore pressure

q = the average flow rate per unit height of fracture

$q_{i+1/2}^k$ = the average flow rate at point $\theta_{i+1/2}$ at time t^k

$q_{i+1/2}^{k+1}$ = the average flow rate at point $\theta_{i+1/2}$ at time t^{k+1}

Q_0 = the injection rate

r = the radial distance

t = the time since pumping starts

Δt = the post-fracture closure time

t^* = a dimensionless fracture surface exposure time since the fluid arrival

t_c = the fracture closure time

Δt_c = the critical time step

t_D = dimensionless time

t_h = the line source Horner time

t_H = the Horner time

Δt^{k+1} = the time step at time t^{k+1}

t_p = shut-in time

t_s = pumping (shut-in) time

u = the fluid leak-off velocity accounting for both of the fracture walls

u_i^k = the fluid leak-off velocity at point $\theta_{i+1/2}$ at time t^k

u_i^{k+1} = the fluid leak-off velocity at point $\theta_{i+1/2}$ at time t^{k+1}

v_c^{k+1} = the fracture volume (per unit height) at time t^{k+1}

v_l^{k+1} = the leak-off volume at time t^{k+1}

v_{inj}^{k+1} = the volume of fluid injected at time t^{k+1}

w = the average width of the fracture

$\dot{w}$ = the width change rate

w_D = dimensionless fracture width

w^e = the fracture width controlled by net stress

w_m = the maximum fracture width

w^p = the fracture width controlled by net pressure

w_i^{k+1} = the fracture width at point θ_i at time t^{k+1}

w_i^k = the fracture width at point θ_i at time t^k

x_f = fracture half length

β = shape factor

β_l = the ratio of fluid loss area to fracture area

β^{k+1} = shape factor at time t^{k+1}

β_s = $\frac{2n+2}{2n+3}$

γ = the surface energy per unit area of the crack

η = poroelastic coefficient

θ = the moving coordinate

κ = the mobility coefficient

μ = the viscosity

ν = the Poisson's ratio

σ_c = the critical stress

σ_0 = the minimum in-situ stress

τ_a = the fracture tip arrival time at a point A

τ_d = the fracture closure time at point A

τ_i^{k+1} = the fracture tip arrival time at point θ_i at time t^{k+1}

$\tau_o(x')$ = the total fracture exposure time at the location x'

$\tau(x)$ = the fracture tip arrival time at the location x

ϕ = the porosity of the rock

ψ = the coefficient depending on the fracture cross section geometry

∇^2 = Laplace's operator

TABLE OF CONTENTS

Page

Page

Page

LIST OF FIGURES

Page

Page

Page

LIST OF TABLES

Page

1. INTRODUCTION

1.1 Hydraulic Fracturing

Hydraulic fracturing is a well stimulation treatment routinely performed on oil and gas wells in low-permeability layers to increase productivity. Special fracturing fluids are pumped at high pressure into the reservoir intervals to be treated, causing a vertical fracture to open. The wings of the fracture extend away from the wellbore in opposite directions according to the original stresses within the formation. Proppant, such as sands of a particular size, is mixed and pumped together with treatment fluid into the fracture to keep it open after the treatment is complete. Hydraulic fracturing creates high-conductivity channel within a large area of formation and bypasses any damage that may exist in the near-wellbore area (Schlumberger Oilfield Glossary).

The technique of hydraulic fracturing has been widely used in the oil industry during the last 50 years. Two of the most important applications of this technology are hydrocarbon well stimulation to increase oil and gas recovery (Economides and Nolte 2000; Veatch 1983a, 1983b) , and geothermal reservoir stimulations (Legarth et al. 2005; Murphy 1983; Nygren and Ghassemi 2006). More than 70% of gas wells and 50% of oil wells in North America are stimulated using hydraulic fracturing (Valko and Economides 1995). Mini-Hydraulic fracturing can also be applied to estimate the in situ stress (Roegiers et al. 1989), leak-off coefficient (Nolte 1979; Nolte and Economides 1989), and formation permeability (Abousleiman et al. 1994; Gu et al. 1993).

This thesis follows the style of *SPE Journal.*

It is important to control the propagation of induced fracture because the cost of hydraulic fracturing operation is high. Fracture should be restrained in the target layers, by preventing them from expanding to adjacent formation. Therefore, it is necessary to simulate the fracture propagation to provide an estimate of fracture geometry before the real operation.

During the process of a hydraulic fracturing, the pumping rate is maintained at a higher rate than the fluid leak-off rate, and the newly created fracture will continue to propagate and grow in the formation until shut-in.

Geertsma (Geertsma and Klerk 1969) considered the potential of poroelastic effects for influencing hydraulically-driven fracture propagation. Cleary (Cleary 1980) suggested that poroelastic effects can be expressed as “back-stress”. Settari included poroelastic effects through a similar approximation (Settari 1980).

Abousleiman derived the pressure-dependent leak-off equation (Abousleiman 1991) instead of the Carter’s leak-off theory, and simulated the PKN hydraulic fracturing history based on the Detournay’s previous work.

Boone, Detournay and Abousleiman evaluated the effects of poroelasticity and the stress intensity factor at fracture tip by the influence function $f(t^*)$ (Abousleiman 1991; Boone and Detournay 1990; Detournay et al. 1990).

Abousleiman and Gu et al. developed the post-fracture pressure-transient theory to calculate the formation permeability (Abousleiman 1991; Abousleiman et al. 1994; Gu et al. 1993), based on the foundation done by Carslaw and Jaeger (Carslaw and Jaeger 1956). It’s a procedure known as “impulse fracture test”, which is an

injection/falloff test designed for determining the formation permeability. The test consists of the injection of a small amount of fluid into the formation to create a short fracture, and then the valve is shut off with the fluid locked in. And the pressure falloff data is monitored beyond the fracture closure to estimate the formation permeability.

1.2 Mechanics of Hydraulic Fracturing

Hydraulic fracturing operation is complicated as it involves fluid and solid mechanics, fluid flow in fracture and diffusion processes (fluid and thermal), and fracture propagation. Furthermore, all of the responses are coupled and depend on each other.

1.2.1 Fluid Leak-off

The type of fracturing fluids used in different fracturing jobs may vary greatly in components, which alters their mechanical properties. In this thesis, Newtonian and Power Law fluid will be used in modeling.

Fracturing fluid in opened fractures is in direct contact with fracture surfaces, and the pressure that is exerted on a formation forces the fracturing fluid into the reservoir through the fracture surfaces. The fluid may flow into the pore spaces in the rock or open new cracks and propagate it into the formation under the fluid flow pressure.

The standard industry leak-off theory was developed by Carter and Settari (Carter 1957; Settari 1985). This approach uses a constant fluid leak-off coefficient C_l to characterize the fluid leak-off rate. However, the fluid spurt loss is not taken into

account. Furthermore, the rate of fluid leak-off into a formation is considered independent of the pressure on fracture/reservoir face and only is a function of time since the beginning of pumping and the fracture arrival time at a location. In this thesis, the pressure dependent leak-off situation derived from the theory proposed by Carslaw and Jaeger and used by (Abousleiman 1991) is used.

1.2.2 Linear Elastic Fracture Mechanics

Fracture mechanics deals with the stability of preexisting cracks and their propagation. Historically, Griffith (Griffith 1921, 1924) laid a foundation for fracture mechanics; he applied the energy balance theory to fracture propagation, considering that the total energy consumed in various parts of the fracturing process is constant. For the opening mode crack (*I*), Griffiths' theory predicts that the critical stress σ_c, which is applied remotely in direction perpendicular to fracture length (Fig. 1.1), needed to propagate the crack is given by the following equation:

$$\sigma_c = \sqrt{\frac{2E\gamma}{\pi a}} \quad \text{.....(1.1)}$$

where E is the Young's modulus of the material, γ is the surface energy per unit area of the crack, and a is crack half length. The quantity $\sigma\sqrt{\pi a}$ is postulated as a material parameter called ‘fracture toughness’. The mode I fracture toughness is defined as

$$K_{Ic} = \sigma_c \sqrt{\pi a} \quad \text{.....(1.2)}$$

which is determined experimentally. Similar quantities of K_{IIc} and K_{IIIc} can be determined for mode *II* and mode *III* loading conditions.

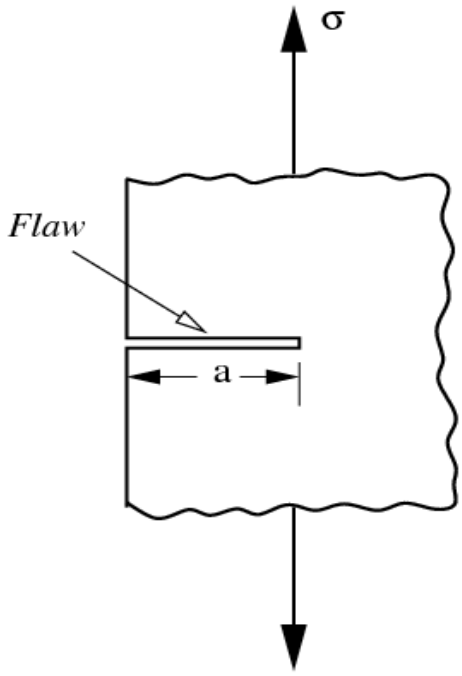

Fig. 1.1 Model (I) crack of a half length in a material.

1.3 Fracture Propagation Models

Several key papers published in the last 50 years laid a foundation for hydraulic fracture modeling on condition of different assumptions, such as two-dimensional fracture model (Abé et al. 1976; Geertsma and Klerk 1969; Khristianovitch and Zheltov 1955; Nordgren 1972; Perkins and Kern 1961) and three dimensional models (Settari and Cleary 1986; Simonson et al. 1978; Warpinski and Smith 1989).

1.3.1 PKN Model

Perkins and Kern (Perkins and Kern 1961) developed equations to compute fracture length and width with a fixed height. Later Nordgren (Nordgren 1972) improved this model by adding fluid loss to the solution, hence, this model is commonly called PKN model. The PKN model assumes that fracture toughness could be neglected, because the energy required for fracture to propagate was significantly less than that required for fluid to flow along fracture length, and the plane strain behavior in the vertical direction, and the fracture has a constant height, and propagates along the horizontal direction (Fig. 1.2).

From the aspect of solid mechanics, when the fracture height, h_f, is fixed and is much smaller than its length, the problem is reduced to two-dimensions by using the plane strain assumption. For the PKN model, plane strain is considered in the vertical direction, and the rock response in each vertical section along the x-direction is assumed independent on its neighboring vertical planes. Plain strain implies that the elastic deformations (strains) to open or close, or shear the fracture are fully concentrated in the vertical planes sections perpendicular to the direction of fracture propagation. This is true if the fracture length is much larger than the height.

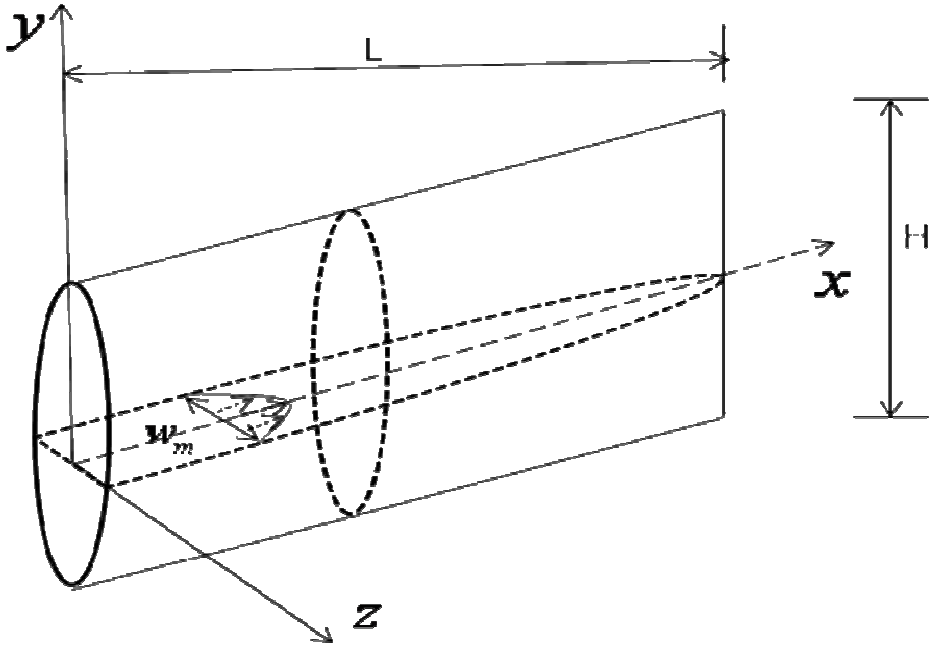

Fig. 1.2 PKN fracture schematic diagram.

From the aspect of fluid mechanics, fluid flow problem in PKN model is considered in one dimension in an elliptical channel. The fluid pressure, p_f, is assumed to be constant in each vertical cross section perpendicular to the direction of propagation.

1.3.2 KGD Model

KGD model was developed by Khristianovitch and Zheltov (Khristianovitch and Zheltov 1955) and Geertsma and de Klerk (Geertsma and Klerk 1969). It considers fracture mechanics effects on the fracture tip, and simplifies the solution by assuming that the flow rate in the fracture is constant and the pressure is also constant along the majority of the fracture length, except for a small region close to the tips. In this model,

plane strain is assumed to be in horizontal direction i.e., all horizontal cross sections act independently. This holds true only if fracture height is much greater than fracture length. Also, since it assumes that the fracture width does not change along the fracture face all section are identical. The model also assumes that fluid flow and fracture propagation are in one dimension (Fig.1.3).

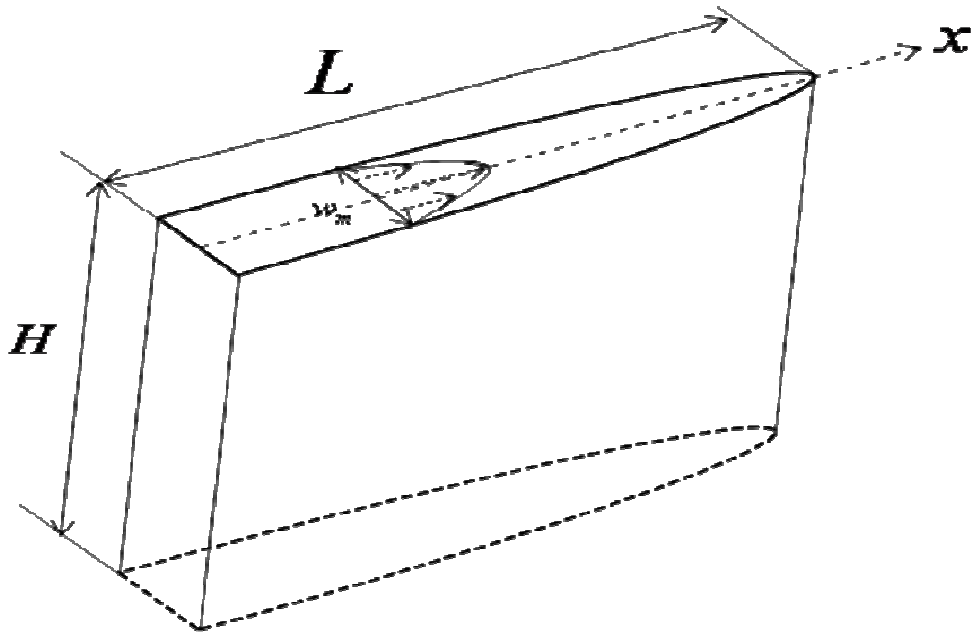

Fig. 1.3 KGD fracture schematic diagram.

In summary, KGD model has six assumptions: 1) the fracture has an elliptical cross section in the horizontal plane; 2) each horizontal plane deforms independently; 3) fracture height, h_f , is constant; 4) fluid pressure in the propagation direction is determined by flow resistance in a narrow rectangular, vertical slit of variable width; 5) fluid does not flow through the entire fracture length; and 6) cross sections in the vertical

plane are rectangular (fracture width is constant along its height) (Geertsma and Klerk 1969).

1.3.3 Penny-Shaped or Radial Model

In this model, the fracture is assumed to propagate within a given plane and the geometry of the fracture is symmetrical with respect to the point at which fluids are injected (Fig. 1.4). A study of penny-shaped fracture in a dry rock mass was carried out by Abé et al. (Abé et al. 1976). In their study, they assumed a uniform distribution of fluid pressure and constant fluid injection rate.

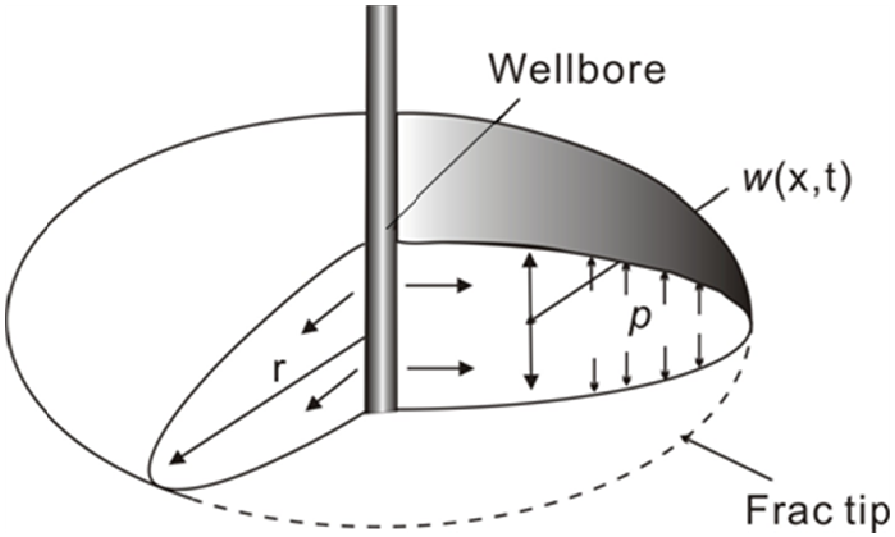

Fig. 1.4 Geometry of a penny-shaped or radial model.

1.3.4 Comparison between 2D Models

The following Table 1.1 makes comparison of the three types of 2D hydraulic fracture models.

Table 1.1 Comparison between traditional 2D hydraulic fracture models

Model	Assumptions	Shape	Application
PKN	Fixed Height, Plain Strain in vertical direction	Elliptical Cross Section	Length »Height
KGD	Fixed Height, Plain Strain in horizontal direction	Rectangle Cross Section	Length «Height
Radial	Propagate in a given plane, Symmetrical to the wellbore	Circular Cross Section	Radial

1.3.5 Three-dimensional and Pseudo Three-dimensional Models

The 2D fracture models discussed in the previous sections have been reasonably successful in practical simulation with a simplified calculation. However, they have limitations in that it is required to specify fracture height and/or assume radial fracture geometry to perform them. To solve that problem, pseudo-3D models are formulated by removing the assumption of constant and uniform height (Morales 1989; Settari and Cleary 1986). Instead, the height in pseudo-3D models is a function of position along the fracture and simulation time. Different from 2D models, a vertical fluid flow component is added in pseudo-3D models, and fracture lengths must be much greater than fracture heights. The even more complex fully 3D models are introduced to handle fractures of arbitrary shape and orientation by removing the assumptions in Pseudo-3D models.

1.4 Poroelasticity

During the propagation of a hydraulic fracture, fracturing fluids loss into the permeable formation causing the pore pressure to increase in the reservoir matrix, which in turn will cause dilation of the rock around the fracture (Fig. 1.5). This will, in turn, reduce the width of the fracture. Rock deformation also causes pore pressure to increase. Often the design of hydraulic fracturing and the stress analysis must take into account the influence of pore pressure increase caused by leak off. The first detailed study of the coupling between fluid pressure and solid stress fields was described by Biot (Biot 1941). In poroelastic theory, a time dependent fluid flow is incorporated by combining the fluid mass conservation with Darcy's law; the basic constitutive equations relate the total stress to both the effective stress given by deformation of the rock matrix and the pore pressure arising from the fluid. Biot's theory of poroelasticity has been reformulated by a number of investigators (Geertsma 1957; Rice and Cleary 1976).

Geertsma(Geertsma and Klerk 1969) considered the potential of poroelastic effects on hydraulically-driven fracture propagation. However, Geertsma concluded that these effects were not significant in practical situations. Cleary suggested that poroelastic effects can be expressed as "back-stress" (Cleary 1980). Settari included poroelastic effects through a similar approximation (Settari 1980). Ghassemi and Roegiers (Ghassemi et al. 1996) presented a coupled poroelastic model using the 3D displacement discontinuity method.

A poroelastic PKN hydraulic fracture model based on an explicit moving mesh algorithm was developed by Boone, Detournay, and Abousleiman et al. (Abousleiman

1991; Boone and Detournay 1990; Detournay et al. 1990). In the latter two, the poroelastic effects, induced by leak-off of the fracturing fluid, were treated in a manner consistent with the basic assumptions of the PKN model. This model is formulated in a moving coordinates system and solved by using an explicit finite difference technique.

Abousleiman derived the pressure-dependent leak-off equation(Abousleiman 1991) instead of the Carter's leak-off theory, and simulated the PKN hydraulic fracturing history based on the Detournay's previous work.

Boone, Detournay and Abousleiman evaluated the effects of poroelasticity and the stress intensity factor at fracture tip by the influence function $f(t^*)$ (Abousleiman 1991; Boone and Detournay 1990; Detournay et al. 1990).

Abousleiman and Gu et al. developed the post-fracture pressure-transient theory to calculate the formation permeability (Abousleiman 1991; Abousleiman et al. 1994; Gu et al. 1993) , based on the foundation done by Carslaw and Jaeger (Carslaw and Jaeger 1956). It's a procedure known as "impulse fracture test", which is an injection/falloff test designed for determining the formation permeability. The test consists of the injection of a small amount of fluid into the formation to create a short fracture, and then the valve is shut off with the fluid locked in. And the pressure falloff data is monitored beyond the fracture closure to estimate the formation permeability.

This thesis builds on the numerical modeling by Jun Ge (Jun 2009) who developed a poroelastic PKN model for the propagation phase without pressure dependent leakoff.

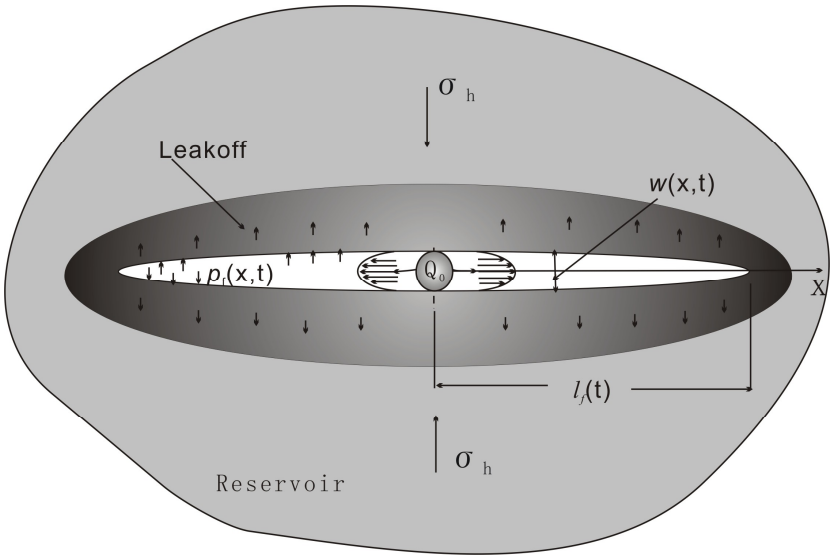

Fig. 1.5 Mechanics of poroelasicity.

1.5 Post-fracture Pressure-Transient Analysis

Pressure transient analysis has been used successfully to estimate reservoir and fracture properties. Early studies concerning the pressure transient behavior of vertically fractured wells include Muskat who used an analytic fractured well model that assumes steady-state flow conditions to investigate pressure distributions and fluid entry patterns in the vicinity of a vertical fracture (Muskat 1937); van Pollen et al. (Poollen et al. 1958) and Prats (Prats 1961) assumed steady-state conditions considering the response of both finite and infinite conductivity fractures (defined as equation (1.3)).. Prats also introduced the concepts of dimensionless fracture conductivity and effective wellbore radius for vertically fractured wells. The dimensionless fracture conductivity is defined as:

$$C_{fD} = \frac{k_f w}{k x_f} \quad \text{.....(1.3)}$$

where k_f is the fracture permeability, w is fracture width, k is the reservoir permeability, and x_f is the fracture half length.

The theory for post-fracture pressure-transient analysis was proposed by Abousleiman and Gu et al. 1994 based on the work by (Abousleiman 1991; Abousleiman et al. 1994; Gu et al. 1993). The methodology is used to interpret an impulse fracture test (an injection/falloff test) to determine the formation permeability and reservoir pore pressure. In this test, a small volume fluid around 10 m^3 injected to the formation to create a short fracture, and then the well is shut-in and pressure is recorded. The pressure falloff after closure is used to derive formation permeability and reservoir pressure. The advantage of this test is that a hydraulic fracture can pass the near wellbore damaged area, so the true formation is exposed to flow transients. Consequently, the permeability and reservoir pressure determined using this theory is potentially much more accurate.

This analysis of this test is based on the distribution of sources of variable intensity along the fracture trajectory. It calculates the formation permeability and reservoir pressure by analyzing the pressure transient during both the linear fracture flow regime in early time, and the radial flow regime at a long time.

1.6 Research Objectives

The objectives of this study are:

1) To model 2D hydraulic fracturing propagation history by coupling fluid flow and rock mechanics, as well as the poroelastic effects on fracture geometry and pressure distribution inside the fracture.
2) To study the influence of pressure inside the fracture on fluid leak-off rate and further on fracture propagation history.
3) To analyze post-fracture pressure-transient curve and then to estimate the formation permeability.

1.7 Sign Convention

Most published papers concerning poroelasticity consider tensile stress as positive. However, in rock mechanics, compressive stresses are generally considered as positive for the convenience of engineering use. In this thesis, in order to be consistent with the rock mechanics literature, all equations are presented using the compression positive convention. This sign convention is adopted for the remainder of this thesis unless otherwise specified.

2. A PKN HYDRAULIC FRACTURE SIMULATION WITH CONSTANT LEAKOFF COEFFICIENT

2.1 Introduction

The Perkins-Kern and Nordgren hydraulic fracture model (PKN) is widely used in the oil and gas industry to design fracture treatments. Its vertical plane strain assumption is physically more acceptable than other models for height-contained fractures, where the fracture length is considerably greater than the fracture height. In this thesis, I developed a PKN model based on the work published by Detournay et al. 1990, which considered poroelasticity with constant leakoff coefficient using moving coordinate scheme. Then, I extended it to consider pressure dependent leak-off similar to Abousleiman (Abousleiman 1991). And finally develop algorithms for reservoir permeability determination using the results of a mini-frac test.

2.2 Governing Equations

In accordance with PKN model, the fracture has a constant height H, elliptic vertical cross-section with the maximum width w_m at the center. And it propagates in horizontal x direction (see Fig. 1.2). Given the injection rate (Q_o) at the wellbore, the fluid properties, the mechanical properties of the rock, the magnitude of the minimum in-situ stress (σ_o), the virgin pore pressure of the formation (p_o), and the leak-off coefficient C_l, it is required to determine the pressure history in the borehole (fracture inlet), as well as the fracture width and length history over time. The mathematical

model for this problem is described below.

2.2.1 Fluid Momentum

The fluid pressure in a fracture is assumed to be uniform over the cross sections of the fracture, varying only in horizontal direction along with fracture propagation. The momentum equation for laminar flow of a power fluid is shown as following:

$$\frac{\partial p_f}{\partial x} = -\frac{2Kq\left|q\right|^{n-1}}{\psi^n w^{2n+1}} \quad \text{.....(2.1)}$$

where p_f is the fluid pressure in the fracture, $q = Q/H$ is the average flow rate per unit height of fracture, $w = A/H$ is the average width of the fracture, *A* is the vertical cross-sectional area, *K* is the constitutive constant for a power law fluid, *n* is the power law index and ψ is the Shape factor dependents on the geometry of the fracture cross section (Nolte 1979):

$$\psi = \frac{n}{2(2n+1)H}\int_{-H/2}^{+H/2}\left(\frac{w_y}{w}\right)^{\frac{2n+1}{n}} dy \quad \text{.....(2.2)}$$

where w_y is the width of the fracture at the vertical coordinate *y*. For an elliptic cross section, the equation is shown as following (Detournay et al. 1990):

$$\psi = \frac{n}{2(2n+1)}\frac{\Gamma\left(\frac{4n+1}{2n}\right)}{\Gamma\left(\frac{5n+1}{2n}\right)}\left(\frac{2}{\sqrt{\pi}}\right)^{\frac{3n+2}{n}} \quad \text{.....(2.3)}$$

2.2.2 Local Fluid Mass Balance

Considering fluid leak-off, fracture volume change, and fluid injection, the local fracturing fluid mass balance is written as (described in Appendix (A.2)):

$$\frac{\partial q}{\partial x}+\frac{\partial w}{\partial t}+u=0 \quad \text{.....(2.4)}$$

where u is the fluid leak-off velocity accounting for both sides of the fracture walls.

2.2.3 Leak-off Equation

The classical Carter leak-off theory (Howard and Fast 1957) is adopted here

$$u=\frac{2C_l}{\sqrt{t-\tau(x)}} \quad \text{.....(2.5)}$$

where C_l is the leak-off coefficient, t is the time since pumping starts, and τ is the arrival time of fracture tip at location x.

2.2.4 Pressure-width Relation

The fracture width w consists of two components: w^e which is controlled by net stress $p=p_f-\sigma_o$, and w^p which is controlled by net pressure $\Delta p=p_f-p_o$. p_f is fluid pressure, σ_o is the minimum in situ stress, and p_o is the virgin pore pressure.

$$w=w^e+w^p \quad \text{.....(2.6)}$$

The net stress effect is approximated as being purely elastic (Boone and Detournay 1990; Detournay et al. 1990):

$$w^e=M_c(p_f-\sigma_o) \quad \text{.....(2.7)}$$

where $M_c = \pi(1-\nu)H/4G$ is the fracture compliance, and ν is the Poisson's ratio, G is the shear modulus, or else M_c should be found from an elastic analysis in plane strain. The net pressure controlled poroelastic effect can be described as (Boone and Detournay 1990; Detournay et al. 1990):

$$w^p = -2\eta\Delta p M_c f(t^*) \quad \text{.....(2.8)}$$

where η is a poroelastic coefficient whose theoretical value ranges from $0 \le \eta \le 1/2$, and $f(t^*)$ is an evolutional function which varies between 0 and 1 as t^* approaching 0 and ∞respectively (Fig. 2.1), used to evaluate the effects of poroelasticity. The symbol t^* denotes as a dimensionless fracture surface exposure time since the fluid arrival which is defined as :

$$t^* = \frac{4c[t-\tau(x)]}{H^2} \quad \text{.....(2.9)}$$

where c is the diffusivity coefficient. For PKN model, the evolutional function $f(t^*)$ is generally dependent on the elastic contrast between permeable and impermeable layers. In case of identical elastic properties existing in the reservoir and barriers, the following expression for $f(t^*)$ was derived (Boone and Detournay 1990) as :

$$f(t^*) = \frac{4}{\pi}\int_0^\infty erfc\left(\frac{y}{2\sqrt{t^*}}\right) g(y)\,dy \quad \text{.....(2.10)}$$

where

$$g(y) = 1 - \sqrt{\frac{y}{2}}\sqrt{\sqrt{4+y^2}-y} \quad \text{.....(2.11)}$$

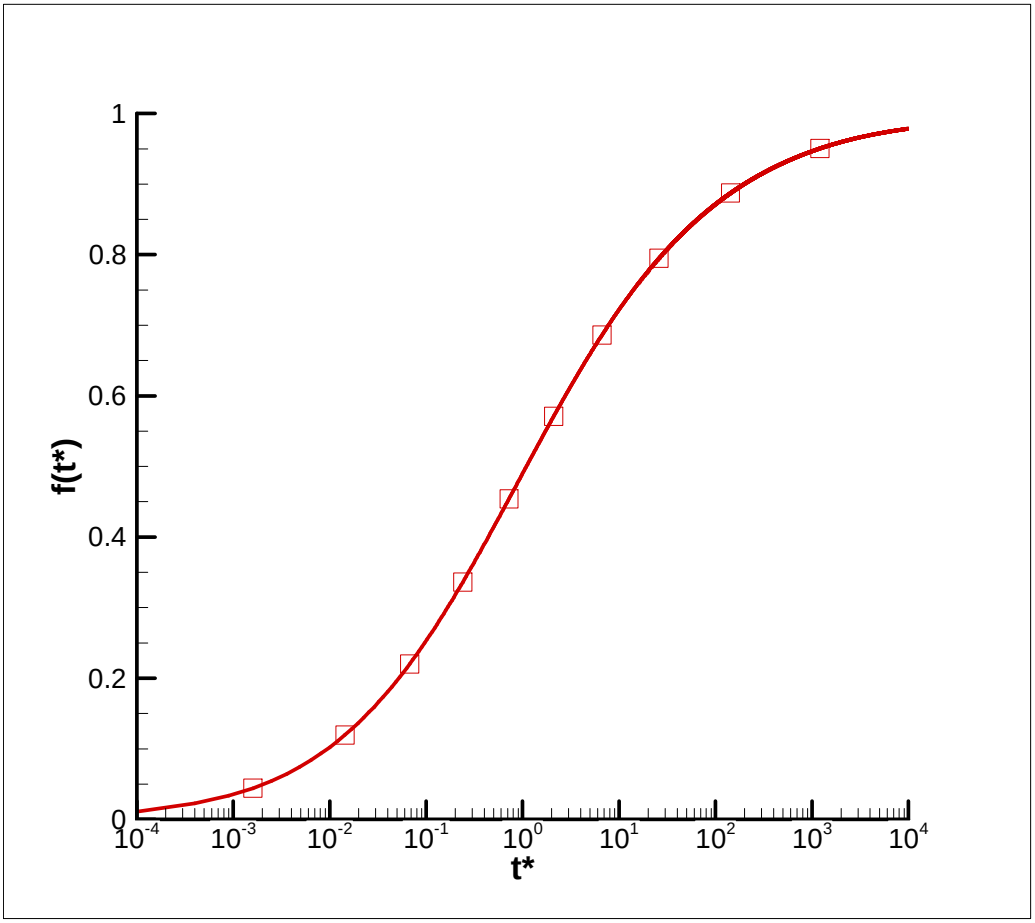

Fig. 2.1 Poroelastic evolutional function.

By substituting (2.7) and (2.8) into (2.6), the pressure-width equation is obtained:

$$p = \frac{w}{M_c} + 2\eta\lambda_p f(t^*) \quad \text{.....(2.12)}$$

2.2.5 Global Mass Balance Equation

The foregoing equations apply in the range of $0 \le x \le L$. The fracture length L is a function of time, which can be derived from a global mass balance consideration. The basic principle of the global mass balance equation is that, the volume of the fracture is

equal to the volume of fluids pumped into the fracture minus the volume of cumulative leak-off fluid:

$$\int_0^{L(t)} w(x,t)dx + \int_0^t \int_0^{L(t')} u(x,t')dxdt' = \int_0^t q_0(t')dt' \quad \text{.....(2.13)}$$

2.2.6 Initial and Boundary Conditions

The boundary conditions used to solve the above equation system indicate the flow state at two fracture end points. At the fracture inlet, the flow rate is equal to the injection rate; and at the fracture tip, the 'net stress' is zero. They are expressed as the following equation:

$$\begin{aligned} q(0,t) &= q_o(t); t > 0 \\ p(L,t) &= 0; t > 0 \end{aligned} \quad \text{.....(2.14)}$$

And the initial conditions indicate the initial state at time $t = 0$. Both fracture length and fracturing pressure are zero at time $t = 0$. They are expressed as the following equation:

$$L(0) = 0,\ p(0,0) = 0 \quad \text{.....(2.15)}$$

2.3 Moving Coordinate System

The governing partial differential equations described in the preceding section are defined on a range of $0 \le x \le L(t)$, which varies during fracture growth. An algorithm based on usual spatial discretization (used by Qiang Zhang (Qiang 2001) needs be adjusted every time step because of the changing fracture length during

simulation. However, one can use a moving coordinate, θ to make the re-meshing unnecessary. The moving coordinate is expressed as:

$$\theta = x / L(t) \quad \text{.....(2.16)}$$

which has a range of [0, 1]. This algorithm allows one to use a constant number of nodes to discretize the variable fracture length throughout the solution procedure. Nilson and Griffiths (Nilson and Griffiths 1983) implemented the moving coordinate system and a finite difference scheme to solve a KGD fracture model. The PKN fracture model is based on an explicit finite difference scheme, which is coupled with an adaptive technique for calculating the optimum time step.

To convert the parameter from x to θ with the foregoing transformation (2.16), spatial and time derivatives transformation are required (Nilson and Griffiths 1983):

$$\left.\frac{\partial}{\partial x}\right|_t = \frac{1}{L}\left.\frac{\partial}{\partial \theta}\right|_t \quad \text{.....(2.17)}$$

and

$$\left.\frac{\partial}{\partial t}\right|_x = \left.\frac{\partial}{\partial t}\right|_\theta - \theta\frac{\dot{L}}{L}\left.\frac{\partial}{\partial \theta}\right|_t \quad \text{.....(2.18)}$$

where the length change rate $\dot{L} = dL / dt$.

Using the transformation described above, the equations (2.1), (2.4), (2.5), an (2.12) are reformulated as the following equations:

$$\frac{1}{L}\frac{\partial p}{\partial \theta} = -\frac{2Kq\left|q\right|^{n-1}}{\psi^n w^{2n+1}} \quad \text{.....(2.19)}$$

$$\dot{w} = \frac{\theta\dot{L}}{L}\frac{\partial w}{\partial \theta} - \frac{1}{L}\frac{\partial q}{\partial \theta} - u \quad \text{.....(2.20)}$$

$$u(\theta,t)=\frac{2C_l}{\sqrt{t-\tau(\theta,t)}} \quad \text{.....(2.21)}$$

$$p(\theta,t)=\frac{w}{M_c}+2\eta\lambda_p f\left(\frac{4c(t-\tau(\theta,t))}{H^2}\right) \quad \text{.....(2.22)}$$

since $x=\theta L(t)$ and $dx=L(t)d\theta$, equation (2.13) is written as :

$$L\int_0^1 w(\theta,t)d\theta+\int_0^t L(t')\int_0^1 u(\theta,t')d\theta dt'=\int_0^t q_0(t')dt' \quad \text{.....(2.23)}$$

with boundary and initial conditions as the following

$$\begin{aligned} &q(0,t)=q_o(t);\ p(1,t)=0;t>0\\ &L=0;\ p=0;\ \text{at } t=0 \end{aligned} \quad \text{.....(2.24)}$$

The five equations above contain five unknowns *p(θ,t), q(θ,t), w(θ,t), L(t)* and *u(θ,t)*. In addition, the fracture arrival time *τ(θ,t)* at a moving point $x=\theta L(t)$ is unknown. However, it can be computed from the inverse of fracture length-time relation, $\tau(\theta,t)=L^{-1}\left(\theta L(t)\right)$ (described in the Appendix (A. 4)).

Attention should be paid to mesh discretization, in which 10 to 15 grid points are acceptable for this problem (Abousleiman 1991), and the nodes are distributed according to a geometric progression (described in the Appendix (A. 3)), which increases their density at both ends of the fracture, near the fracture tip and the wellbore to account for the high pressure gradients in propagation as well as in fracture recession (see Fig. 2.2). A system of $n-1$ auxiliary mid-nodes $i+1/2$ is also introduced to calculate the flux q to avoid infinite flux values at the fracture tip. In the following section, the discrete values are denoted by a subscript corresponding to the nodal number and a superscript

corresponding to the time-step. Such as, $w_i^k = w(\theta_i, t^k)$, $q_{i+1/2}^k = q(\theta_{i+1/2}, t^k)$, $L^k = L(t^k)$, etc.

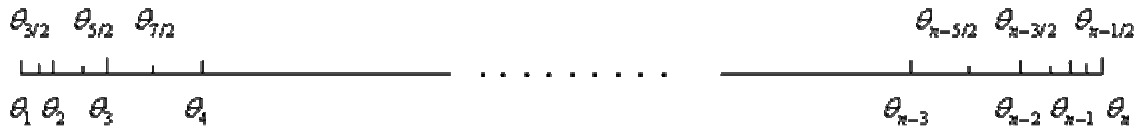

Fig. 2.2 Mesh discretization.

2.4 Discrete Equations

Using finite difference scheme, the governing equations are expressed in terms of discrete variables. With the forward Euler difference (see Fig. 2.3) in time, the local fluid mass balance equation (2.20) can be written as:

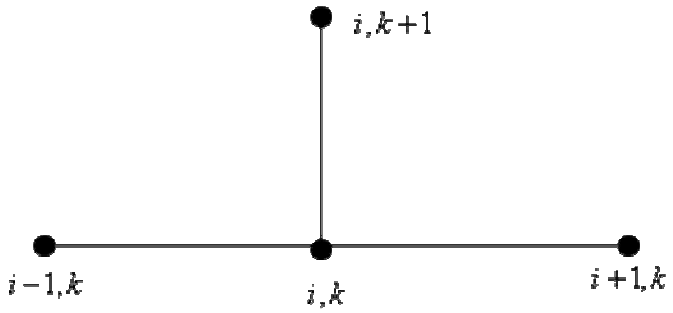

Fig. 2.3 The explicit forward finite difference scheme at time step *k*.

$$w_i^{k+1} = w_i^k + \Delta t^{k+1}\left[\left(\frac{\theta_i \dot{L}^k}{L^k}\frac{w_{i+1}^k - w_i^k}{\theta_{i+1} - \theta_i}\right) - \frac{2}{L^k}\left(\frac{q_{i+1/2}^k - q_{i-1/2}^k}{\theta_{i+1} - \theta_{i-1}}\right) - u_i^k\right];\ i = 2, N\text{-}2 \ldots.(2.25)$$

where $\Delta t^{k+1} = t^{k+1} - t^k$. Note that an upwind differentiation scheme is adopted for $\frac{\partial w}{\partial \theta} = \frac{w_{i+1}^k - w_i^k}{\theta_{i+1} - \theta_i}$, in order to reduce the 'advection error' associated with the moving mesh. At node $n-1$ the forward difference formula for $\frac{\partial w}{\partial \theta}$ is unstable during simulation and a backward difference formula is used instead:

$$w_{N-1}^{k+1} = w_{N-1}^k + \Delta t^{k+1}\left[\left(\frac{\theta_{N-1} \dot{L}^k}{L^k}\frac{w_{N-1}^k - w_{N-2}^k}{\theta_{N-1} - \theta_{N-2}}\right) - \frac{2}{L^k}\left(\frac{q_{N-1/2}^k - q_{N-3/2}^k}{\theta_N - \theta_{N-2}}\right) - u_{N-1}^k\right];\ i = N\text{-}1$$

…….(2.26)

At the first and the last node, equation (2.25) is specialized as

$$w_1^{k+1} = w_1^k - \Delta t^{k+1}\left[\frac{2}{L^k}\frac{q_{3/2}^k - q_o^k}{\theta_2} + u_1^k\right] \ldots\ldots\ldots\ldots\ldots\ldots\ldots\ldots\ldots\ldots\ldots\ldots..(2.27)$$

$$w_N^{k+1} = 0 \ldots\ldots\ldots\ldots\ldots\ldots\ldots\ldots\ldots\ldots\ldots\ldots\ldots\ldots\ldots\ldots\ldots\ldots\ldots\ldots\ldots\ldots...(2.28)$$

For a receding fracture, the derivative at node *i* should be replaced by the backward difference form $\frac{\partial w}{\partial \theta} = \frac{w_i^k - w_{i-1}^k}{\theta_i - \theta_{i-1}}$ (described in Appendix (A.8)):

$$w_i^{k+1} = w_i^k + \Delta t^{k+1}\left[\left(\frac{\theta_i \dot{L}^k}{L^k}\frac{w_i^k - w_{i-1}^k}{\theta_i - \theta_{i-1}}\right) - \frac{2}{L^k}\left(\frac{q_{i+1/2}^k - q_{i-1/2}^k}{\theta_{i+1} - \theta_{i-1}}\right) - u_i^k\right];\ i = 2, N\text{-}1 \ldots..(2.29)$$

The equation (2.29) is specialized for the first and last node during recession, which is the same as equation (2.27) and (2.28).

The pressure-width equation (2.22) becomes

$$p_i^{k+1} = \frac{w_i^{k+1}}{M_c} + 2\eta\lambda_p f\left(\frac{4c(t^{k+1} - \tau_i^{k+1})}{H^2}\right); i = 1, N \quad \text{.....(2.30)}$$

In which the fracture arrival time is evaluated as (described in the Appendix (A.4))

$$\tau_i^{k+1} = L^{-1}(\theta_i L^k) \text{.....(2.31)}$$

The fluid momentum equation (2.18) is discretized as

$$q_{i+1/2}^{k+1} = \text{sign}\left(p_i^{k+1} - p_{i+1}^{k+1}\right)\psi\left[\frac{\left(w_{i+1}^{k+1} + w_i^{k+1}\right)^{2n+1}}{2^{2n+2} K L^k}\left|\frac{p_{i+1}^{k+1} - p_i^{k+1}}{\theta_{i+1} - \theta_i}\right|\right]^{1/n}; i = 1, N-1$$

.....(2.32)

where *sign* () denotes the sign of argument.

The leak-off equation (2.21) becomes

$$u_i^{k+1} = \frac{2C_l}{\sqrt{t^{k+1} - \tau_i^{k+1}}}; i = 1, N-1 \quad \text{.....(2.33)}$$

For a propagating fracture the leak-off velocity at the fracture tip is infinite according to equation (2.33) because $\tau_n^{k+1} = t^{k+1}$. For the purpose of evaluating the fluid leak-off volume lost by the tip element (as needed in (2.23)), the average fluid leak-off between nodes $N-1/2$ and N is assigned to the last node.

$$u_N^{k+1} = \frac{4C_l}{\sqrt{t^{k+1} - \tau_{N-1/2}^{k+1}}}, i = N \text{.....(2.34)}$$

To update the fracture length L, we will examine the global mass balance equation (2.23). At $k+1$ time step it is written as

$$v_c^{k+1} + v_l^{k+1} = v_{inj}^{k+1} \quad \text{.....(2.35)}$$

v_c^{k+1} stands for fracture volume (per unit height), v_l^{k+1} is leak-off volume, and v_{inj}^{k+1} is the volume of fluid injected, at time t^{k+1}. The fracture volume is evaluated as

$$v_c^{k+1} = \beta^{k+1} w_1^{k+1} L^{k+1} \quad \text{.....(2.36)}$$

where β is a shape factor, which is used to calculate the volume of a fracture:

$$\beta^{k+1} = \frac{\theta_2}{2} + \sum_{i=2}^{N-1} \frac{(\theta_{i+1} - \theta_{i-1}) w_i^{k+1}}{2 w_1^{k+1}} - \frac{(1 - \theta_{N-1}) w_{N-1}^{k+1}}{6 w_1^{k+1}} \quad \text{.....(2.37)}$$

The volume of fluid injected v_{inj}^{k+1} is the summation of fluid volume injected during every time step, and the volume of fluid lost to the formation v_l^{k+1} is the summation of the fluid leak-off volume along the entire fracture length during every time step, and they are respectively calculated as:

$$v_{inj}^{k+1} = \sum_{j=1}^{k+1} q_0^j \Delta t^j = v_{inj}^k + q_0^{k+1} \Delta t^{k+1} \quad \text{.....(2.38)}$$

$$\begin{aligned} v_l^{k+1} &= \frac{1}{2} \sum_{j=1}^{k+1} \sum_{i=1}^{N} (\theta_{i+1} - \theta_{i-1}) u_i^j \Delta t^j \\ &= v_l^k + \frac{\Delta t^{k+1} L^k}{2} \sum_{i=1}^{N} (\theta_{i+1} - \theta_{i-1}) u_i^{k+1} \end{aligned} \quad \text{.....(2.39)}$$

In equation (2.39) central difference is applied, special attention should be paid to the summation at the first and last node, as they occupy only half a cell. So it can be expressed as:

$$v_l^{k+1} = v_l^k + \frac{\Delta t^{k+1} L^k}{2} \left[\sum_{i=2}^{N-1} (\theta_{i+1} - \theta_{i-1}) u_i^{k+1} + (\theta_2 - \theta_1) u_1^{k+1} + (\theta_N - \theta_{N-1}) u_N^{k+1} \right] \quad \text{.....(2.40)}$$

The fracture length L^{k+1} can be derived from equation (2.35) and (2.36) as

$$L^{k+1} = \frac{v_{inj}^{k+1} - v_l^{k+1}}{\beta^{k+1} w_1^{k+1}} \quad \text{.....(2.41)}$$

Finally the change rate of the fracture length $\dot{L}$, as needed in (2.25), can be updated using the backwards difference equation as:

$$\dot{L}^{k+1} = (L^{k+1} - L^k) / \Delta t^{k+1} \quad \text{.....(2.42)}$$

2.5 Stability Criterion

A popular method developed by Von Neumann analyzes the conditions of unstable propagation of a perturbation on a finite difference grid with time (Press et al. 1989). The following is the approach derived by Detournay et al. 1990 for the calculation of the time step: rewriting the PKN equations in the form of a diffusion-type equation of w, by substituting equation (2.19) and (2.22) into (2.20) and ignoring the leak-off and poroelastic terms, we get the following diffusion-type equation for w:

$$\dot{w} = c_w \frac{\partial^2 w}{\partial \theta^2} + \frac{(2n+1)c_w}{w} \left(\frac{\partial w}{\partial \theta}\right)^2 + \frac{\theta \dot{L}}{L} \frac{\partial w}{\partial \theta} \quad \text{.....(2.43)}$$

where the 'diffusivity coefficient' c_w is given by

$$c_w = \left[\frac{2G\psi^n w^{2n+1}}{\pi n^n (1-\nu) K H L^{n+1}} \left|\frac{\partial w}{\partial \theta}\right|^{1-n}\right]^{1/n} \quad \text{.....(2.44)}$$

Note that for Newtonian fluids ($n=1$) c_w reduces to

$$c_w = \frac{4Gw^3}{\pi^3 (1-v) \mu H L^2} \quad \text{.....(2.45)}$$

Apparently, the differential equation (2.43) is highly nonlinear, as c_w is a function of w. We assume that the stability condition can be assessed by ignoring the second and third term (to satisfy the nonlinear stability) in the right-hand side of the equation (2.43), so it is expressed as:

$$\dot{w} = c_w \frac{\partial^2 w}{\partial \theta^2} \quad \text{.....(2.46)}$$

According to the Von Neumann stability analysis (also known as Fourier stability analysis), the stability requirement to the one-dimensional heat equation (2.46) is:

$$\frac{c_w \Delta t}{\Delta \theta^2} \le \frac{1}{2} \quad \text{.....(2.47)}$$

and calculating c_w from the previous time step. The critical time step, Δt_c at t^{k+1} is then computed at each iteration according to the general stability criterion for heat equation

$$\Delta t_c^{k+1} = \min\left[\frac{\Delta \theta_i^2}{2(c_w)_i^k}\right]; i = 1, N-1 \quad \text{.....(2.48)}$$

In fact, based on a dimensional analysis, it can be shown for a PKN geometry without leak-off that (Nolte and Economides 1989)

$$\begin{aligned} w &\sim L^{1/(2n+3)} \\ L &\sim t^{(2n+2)/2n+3} \end{aligned} \quad \text{.....(2.49)}$$

Consequently,

$$c_w \sim t^{-1} \quad \text{.....(2.50)}$$

which implies that Δt_c increases linearly with time when there is no fluid leak-off.

2.6 Solution Procedure and Time-stepping

The numerical solution must start with any initial state. It's impossible to start at $L = 0$ at $t = 0$; hence an artificial initial condition based on an approximate solution is necessary. Here we impose the approximate solution (Nolte and Economides 1989) in order to calculate the initial length, width, pressure, etc at a small initial time. With the nodal quantities, w_i^k, p_i^k, $q_{i+1/2}^k$, u_i^k, L^k and $\dot{L}^k$ at time t^k, the solution is advanced to the next time t^{k+1} using the following the procedure:

1. The magnitude of the next time step, Δt^{k+1}. In the case of constant fluid leak-off coefficient, Δt^{k+1} is calculated using the stability criterion (2.48).
2. The fracture width, w_i^{k+1}, is calculated using the local mass balance equation (2.25) when the fracture propagates; and equation (2.29) when the fracture recedes.
3. The 'net stress', p_i^{k+1}, is estimated from equation (2.30).
4. The flow rate, $q_{i+1/2}^{k+1}$, is updated from equation (2.32).
5. The fluid leak-off rate, u_i^{k+1}, is evaluated using (2.33) and (2.34).
6. Finally the fracture length L^{k+1} and its change rate $\dot{L}^{k+1}$ are updated from (2.41) and (2.42), respectively.

2.7 The Program Flow Chart

According to the solution procedure described above, a flow chart of the program is made (Fig. 2.4). First step is to determine whether the poroelastic effect of the formation is to be considered or not. The poroelastic coefficient is set to be zero when assuming the formation is elastic; otherwise it is a non-zero value ranges from 0 to 0.5. The next step is to input the other parameters, and initialize a small starting time, and calculate the initial fracture length, pressure, width, etc. Then start the loop according to the solution procedure, if the simulation time is less than the input shut-in time, the fracture is propagating. In this case, after adjust the initial values at the first time loop, and then calculate the values for next time step in the order of the solution procedure. During shut-in phase, i.e., when the simulation time is larger than the shut-in time, injection is ceased and fracture recedes. This is done by setting the injection rate to be zero. Calculate the parameters in the same order as in the propagation section ($\Delta t^{k+1} \Rightarrow w_i^{k+1} \Rightarrow p_i^{k+1} \Rightarrow q_{i+1/2}^{k+1} \Rightarrow u_i^{k+1} \Rightarrow L^{k+1} \Rightarrow \dot{L}^{k+1}$), until the fracture width or pressure or length is small enough or is zero.

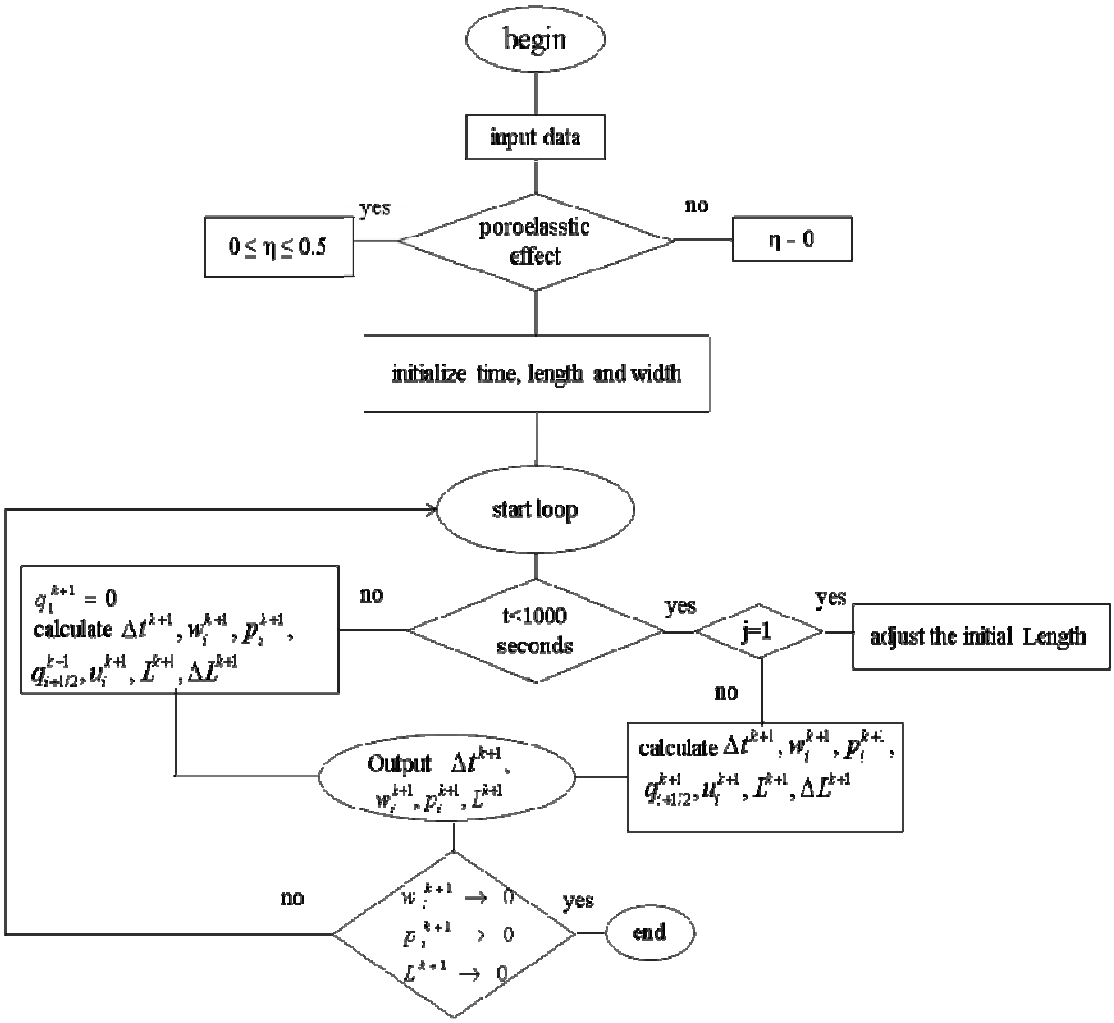

Fig. 2.4 The flow chart of the program.

2.8 Verification of Solution

Assuming one simple case when a fracture is driven in impermeable rocks (no fluid leak-off) by a Newtonian fluid pumped at a constant rate, based on the argument of self-similarity, the dimensionless length, width, pressure, and time corresponding to the fracture length, maximum width and pressure at the inlet and simulation time, are expressed below as derived by Nordgren (Nordgren 1972).

$$L_D(t_D) = 1.56 t_D^{4/5}$$
$$w_D(0, t_D) = 1.09 t_D^{1/5} \quad \text{.....(2.51)}$$
$$p_D(0, t_D) = 0.855 t_D^{1/5}$$

And

$$L_D = \frac{1}{4}\left[\frac{G}{(1-\nu)\mu Q_o}\right]^{\frac{1}{3}} L$$
$$w_D = \frac{1}{4}\left[\frac{G}{(1-\nu)\mu Q_o}\right]^{\frac{1}{3}} w_m \quad \text{.....(2.52)}$$
$$p_D = \frac{\pi}{16}\left[\frac{(1-\nu)^2 H^3}{G^2 \mu Q_o}\right]^{\frac{1}{3}} p$$
$$t_D = \frac{1}{16}\left[\frac{G^2 Q_o}{(1-\nu)^2 \mu^2 H^3}\right]^{\frac{1}{3}} t$$

Table 2.1 Input data for verification

Fluid viscosity, μ	5.6×10^{-7} MPa·s
Injection rate, Q_0	4×10^{-3} m^3/s
Poisson's ratio, ν	0.2
Shear modulus, G	1×10^4 MPa
Fracture height, H	10 m
Injection time, t	1000 sec

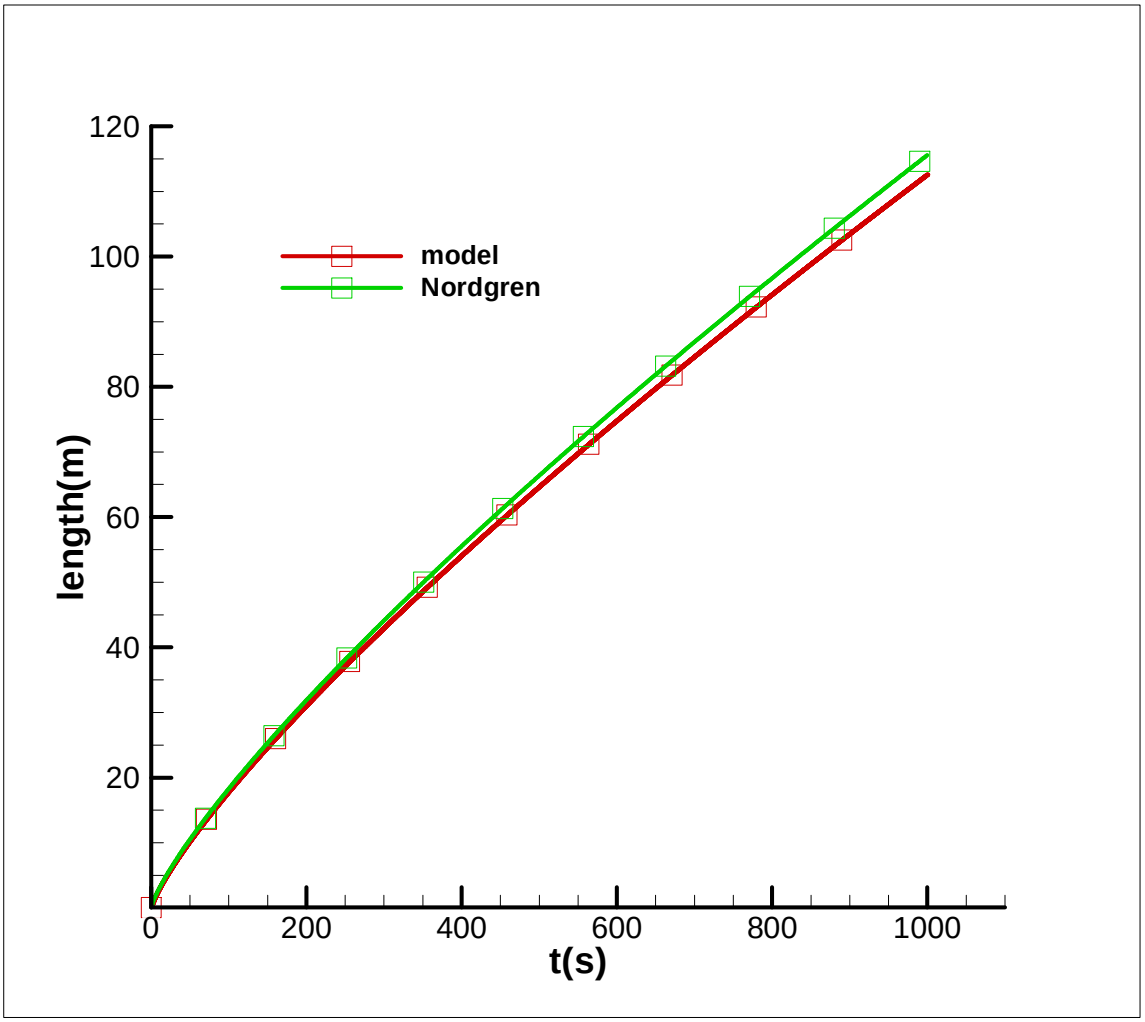

Fig. 2.5 Fracture length history-no leakoff.

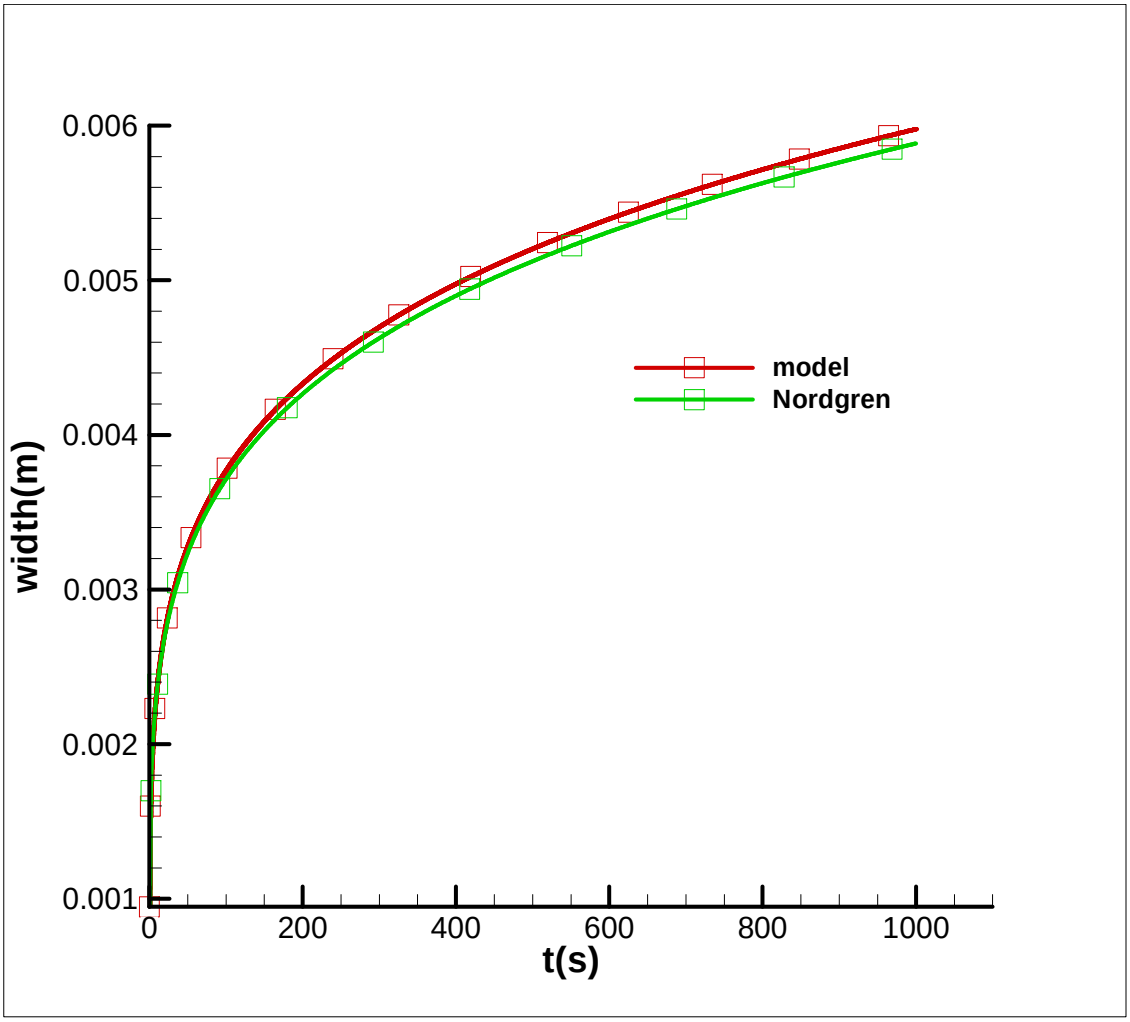

Fig. 2.6 Fracture width history-no leakoff.

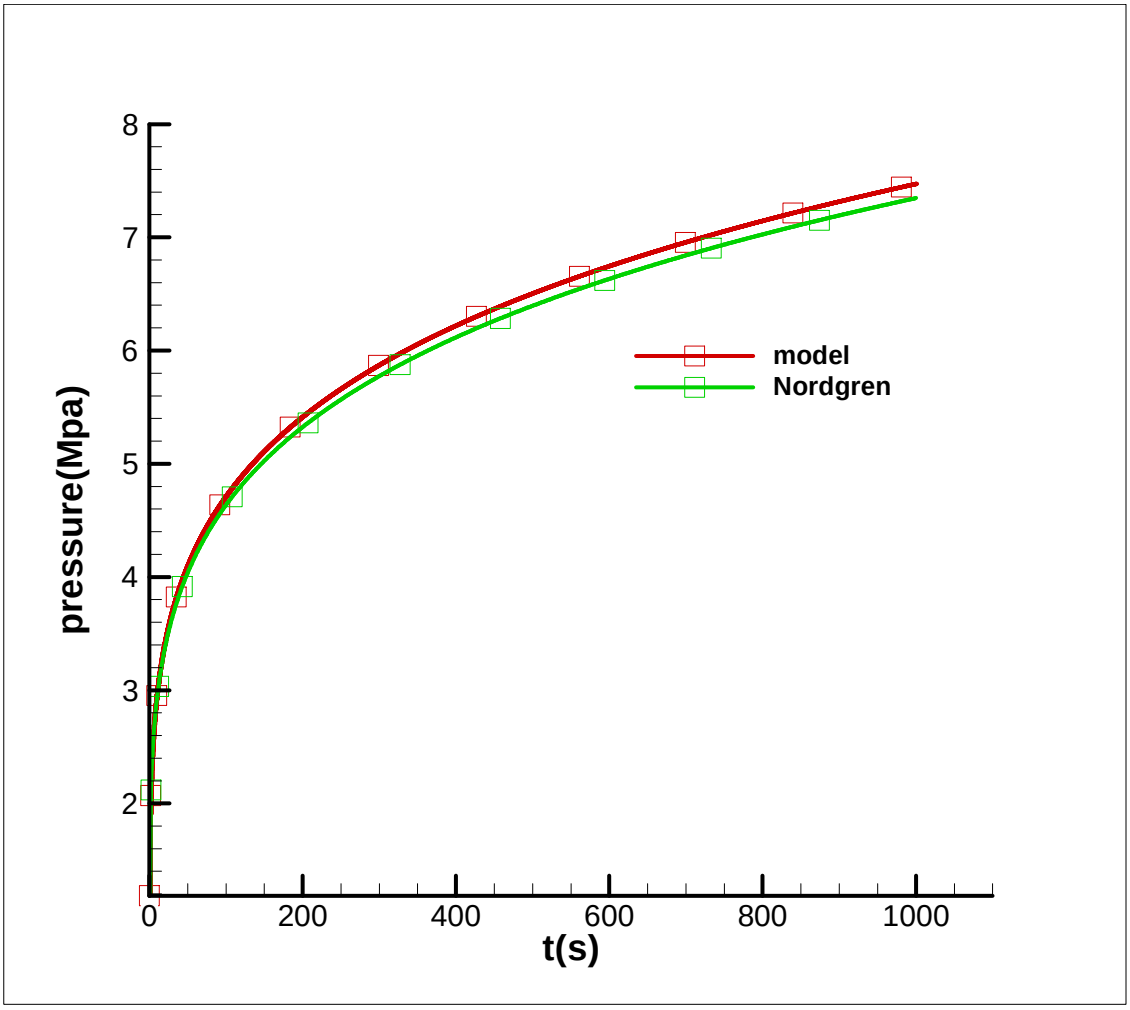

Fig. 2.7 Fracture pressure history-no leakoff.

Note that to be consistent with Nordgren's notation, w_D is defined with respect to the maximum fracture width (see Fig. 1.2), which is related to the average width by $w_m = 4w/\pi$. This problem is simulated by the numerical model with the same assumption as the Nordgren solution (Table 2.1), without leak-off and Newtonian fluid. The fracture length, width and pressure figures (Fig. 2.5), (Fig. 2.6) and (Fig.2.7) show a close agreement between the two solutions.

2.9 Case Study

To compare with the results of previous work by Detournay, *et al.* (Detournay et al. 1990), the PKN fracture model with a *constant fluid leak-off coefficient* is simulated by injecting at the constant flow rate Q_0 for 1000s, and then the well is shut in (Table 2.2). After the shut in of the well, the fracture pinching is analyzed without fluid flow back. Poroelastic effect is included by considering the function (2.6) and adding the aperture due to 'net pressure'.

Table 2.2 Input data for constant leak-off coefficient simulation

Power law constitutive constant, K	5.6×10^{-7} MPa·s$^{0.8}$
Power law fluid index, n	0.8
Injection rate, Q_0	4×10^{-3} m^3/s
Poisson's ratio, ν	0.2
Shear modulus, G	1×10^4 MPa
Fracture height, H	10 m
Leak-off coefficient, C_l	6.3×10^{-5} m/s$^{0.5}$
Interface pressure, λ_p	1.7 MPa
Poroelastic coefficient, η	0.25
Diffusivity coefficient, c	0.4 m^2/s
Injection time, t	1000 sec

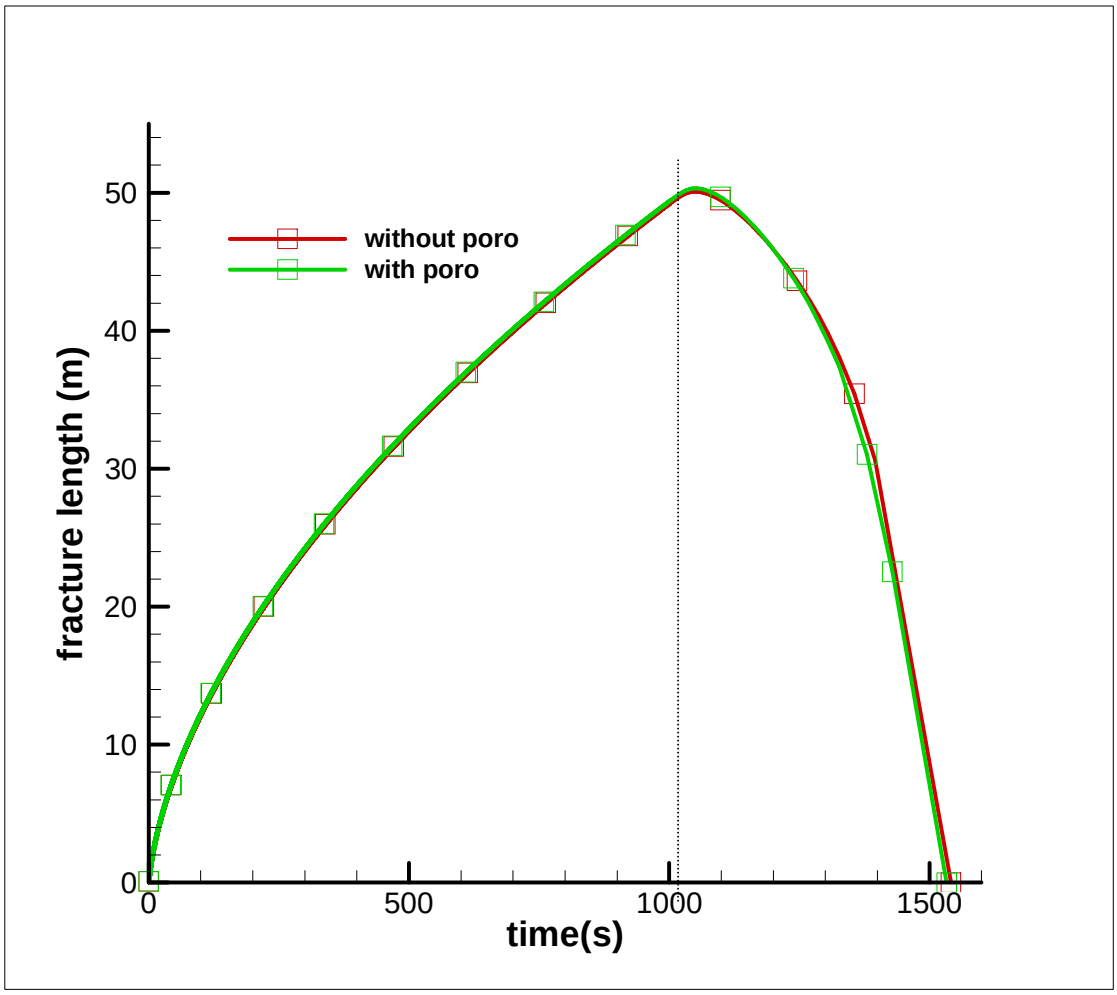

Fig. 2.8 Fracture length change with time, with and without poroelastic.

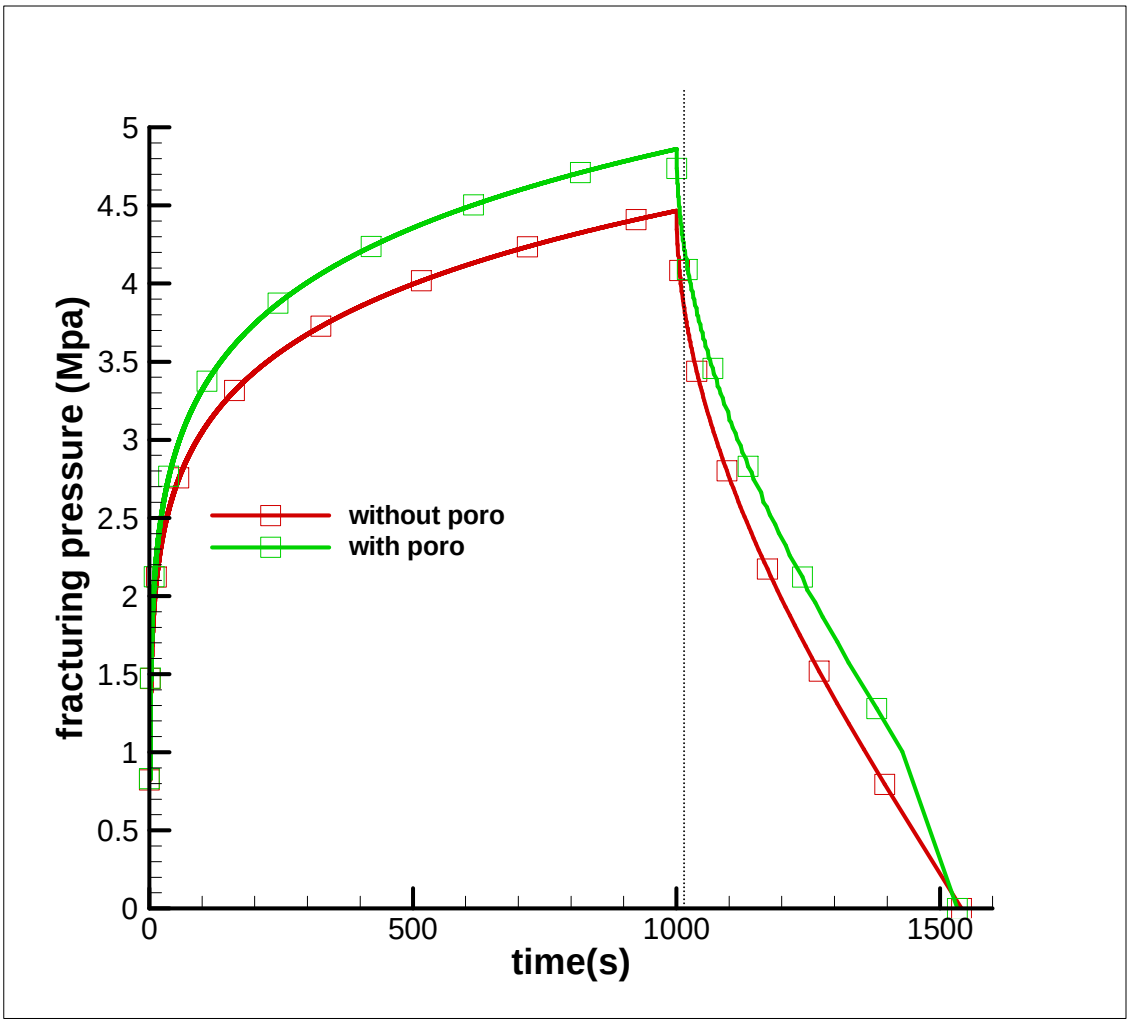

Fig. 2.9 Fracturing pressure change with time, with and without poroelastic.

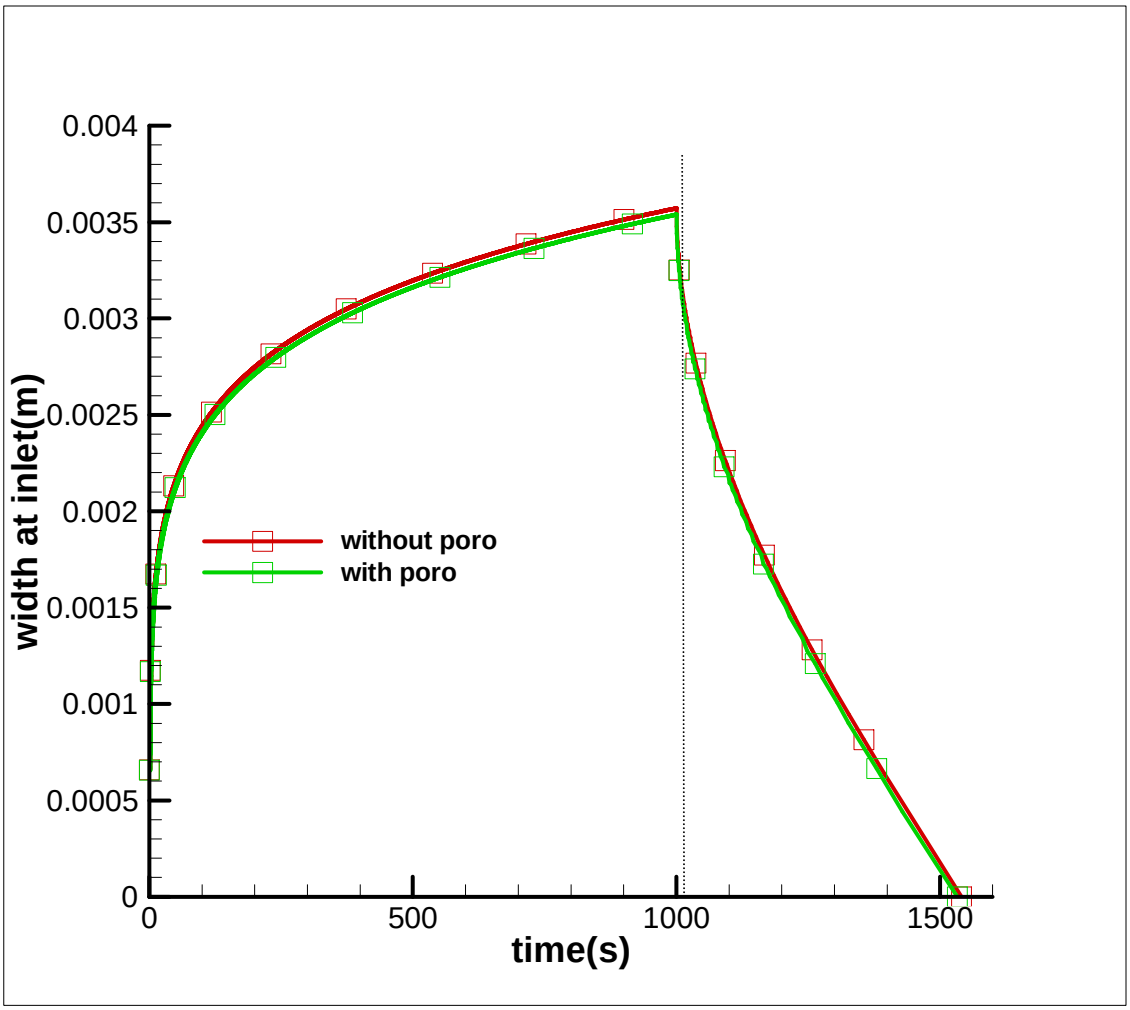

Fig. 2.10 Maximum fracture width change with time, with and without poroelastic.

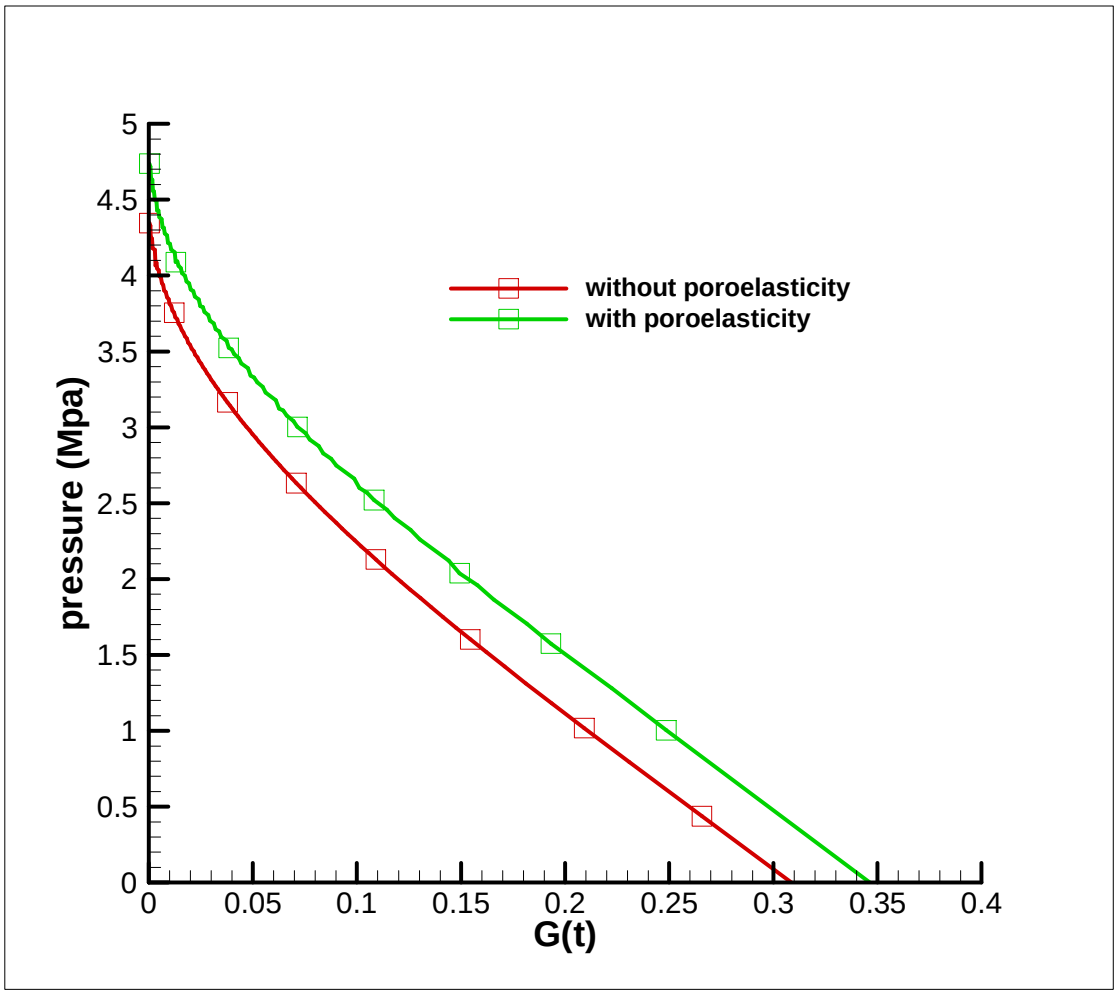

Fig. 2.11 G-function during fracture recesion.

The fracture length as shown in Fig. 2.8 will continue to propagate beyond the point of shut-in, which is due to the continued fluid flow in the fracture driven by the existing pressure gradient. However, Figs.2.9 and 2.10 show that both the fracturing pressure and maximum width increase with time during injecting fluid, and decline since shut-in. The poroelasticity causes a significant increase in fracturing pressure and a

slight reduction in fracture width, without affecting the fracture length. And the G-function curve in Fig. 2.11 is used a lot to calculate the leak-off coefficient.

To verify the results of this study, the plots are compared with the results of Detournay et al. (Detournay et al. 1990). It turned out that the simulation results of the net fracturing pressure, the fracture length, and maximum width are close (described in the Appendix (A.5)), with the differences less than 5%. The good agreement between my work and Detournay further validated the simulation results of both studies.

2.10 Summary

From the study, the effects of poroelasticity on fracture propagation can be summarized as the following:

1 Poroelasticity causes a significant increase in fracturing pressure

2 The fracture length is unaffected;

3 The fracture width is slightly reduced.

Consequently, this study suggests that poroelastic effects can cause a significant increase of the fracturing pressure, but have little influence on the geometry of the fracture. This is a direct consequence of assuming a constant leak-off coefficient: the fracture volume (shown as fracture length and width) is controlled by the difference between the injected fluid volume and the leak-off volume, both of which are pressure independent, leading to the fracture volume is unaffected by the poroelasticity. It can be expected that for pressure dependent leak-off, the prediction of both fracture geometry and pressure will be different. Since the pressure response is under strong influence of

poroelasticity, ignoring poroelastic effects can lead to an erroneous interpretation of parameters such as minimum in situ stress, leak-off coefficient, when determining of the state of the formation during an actual treatment.

3. A PKN HYDRAULIC FRACTURE SIMULATION WITH PRESSURE-DEPENDENT LEAKOFF

3.1 Introduction

The Carter's leak-off theory as described in equation (2.5) indicates that the fluid leak-off rate at any point along the fracture at time t is related to a constant leak-off coefficient C_l. However, it does not consider the influence of time variable fluid pressure inside the fracture. It is easy to imagine that, the fracture pressure goes up during injection, which pushes much more fluid into the surrounding formation. While the fluid pressure inside the fracture goes down after well shut-in, a lower fluid leak-off rate along the fracture should be observed, until the fracture closes at the time fluid pressure equals to the reservoir pressure.

The horizontal cross-section of PKN fracture model with constant height H (Fig. 1.2) is shown in Fig. 3.1, a $2L$ length fracture propagates in the horizontal direction x, and the flow of the fracturing fluid into the porous formation is assumed to be linear and perpendicular to the face of the fracture in y direction, under the influence of fluid pressure p_f in the fracture.

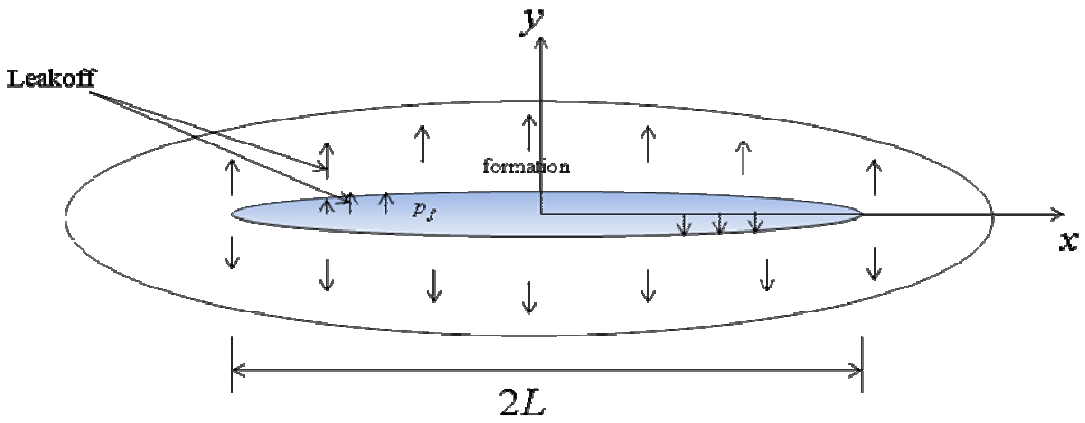

Fig. 3.1 A fluid-pressurized stationary fracture.

3.2 Governing Equation

3.2.1 Pressure Dependent Leak-off Equation

It can be shown that leak-off effect can be separated into two parts: one part is the in situ effective stress neglecting the rock strength and thus the toughness in tension; and the other part is the 'net stress', which changes with time (Abousleiman 1991). The pressure dependent leak-off equation is (described in Appendix (A.6)):

$$u = \frac{2\kappa(\sigma_o - p_o)}{\sqrt{\pi c(t-\tau(x))}} + \frac{2\kappa}{\sqrt{\pi c}} \int_{\tau(x)}^{t} \frac{\partial p(x,t')}{\partial t'} \frac{1}{\sqrt{t-t'}} dt' \quad \text{.....(3.1)}$$

where u is the fluid leak-off rate, κ is the mobility coefficient defined as the ratio of the permeability k to the viscosity μ, c is the diffusivity coefficient defined as $c = \frac{\kappa}{\phi C_p}$, and ϕ is the porosity of the rock, C_p is the compressibility of the pore and pore fluid system, t is the time since pumping start, $\tau(x)$ is the arrival time of the fracture tip at location x

(described in Appendix (A.4)), σ_o is the minimum in situ stress, p_o is the virgin pore pressure, $_p$ is the 'net stress' defined as $p = p_f - \sigma_o$, and p_f is the flow pressure in the fracture.

3.2.2 Pressure-width Relation

The pressure-dependent leak-off will change the fluid leak-off rate to surrounding formation, since w_p is the reduced fracture width caused by fluid loss into the permeable formation and induced a dilation of the surrounding rock. Consequently, the pressure-dependent leak-off changes the w_p formula from (2.8) to the following expression (Detournay and Cheng 1991):

$$w^p = -2\eta M_c(\sigma_o - p_o) f(t^*) - 2\eta M_c \int_{\tau(x)}^{t} \frac{\partial p(x,t')}{\partial t'} f(\frac{4c(t-t')}{H^2}) dt' \text{ ……..(3.2)}$$

in which η is the poroelasticity coefficient, M_c is fracture compliance, H the fracture height. w_p also consists of two parts' effects: the first term on the right of the equation is the effect of the in situ effective stress neglecting the rock strength and thus the toughness in tension; the second term is the effect of the 'net stress'.

Combining equation (2.6), (2.7) and (3.2)

$$p = \frac{w}{M_c} + 2\eta\lambda_p f(t^*) + 2\eta \int_{\tau(x)}^{t} \frac{\partial p(x,t')}{\partial t'} f(\frac{4c(t-t')}{H^2}) dt' \text{ ……...(3.3)}$$

Translating equations (3.1) and (3.3) into a moving coordinate system, according to (2.17) and (2.18)

$$u(\theta,t)=\frac{2\kappa(\sigma_o-p_o)}{\sqrt{\pi c(t-\tau(\theta,t))}}+\frac{2\kappa}{\sqrt{\pi c}}\int_{\tau(\theta,t)}^{t}\frac{h(\theta,t')}{\sqrt{t-t'}}dt' \quad \text{.....(3.4)}$$

$$p=\frac{w}{M_c}+2\eta\lambda_p f(t^*)+2\eta\int_{\tau(x)}^{t}\frac{\partial p(x,t')}{\partial t'}f(t-t')dt' \quad \text{.....(3.5)}$$

Discrete equations (3.4) and (3.5) using an explicit finite-difference scheme:

$$u_i^{k+1}=\frac{2\kappa}{\sqrt{\pi c}}\left[\frac{\sigma_o-p_o}{\sqrt{t^{k+1}-\tau_i^{k+1}}}+\int_{\tau_i^{k+1}}^{t^{k+1}}\frac{h(\theta_i,t')}{\sqrt{t^{k+1}-t'}}dt'\right];i=1,N-1 \quad \text{.....(3.6)}$$

$$u_N^{k+1}=\frac{2\kappa}{\sqrt{\pi c}}\left(\frac{2(\sigma_o-p_o)}{\sqrt{t^{k+1}-\tau_{N-\frac{1}{2}}^{k+1}}}\right) \quad \text{.....(3.7)}$$

$$p_i^{k+1}=\frac{w_i^{k+1}}{M_c}+2\eta(\sigma_o-p_o)f\left(\frac{4c(t^{k+1}-\tau_i^{k+1})}{H^2}\right)+2\eta\int_{\tau_i^{k+1}}^{t^{k+1}}h(\theta_i,t')f\left(\frac{4c(t^{k+1}-t')}{H^2}\right)dt'$$

……..……(3.8)

and

$$h(\theta,t')=\frac{\partial p(x,t')}{\partial t'}=\frac{\partial p(\theta,t')}{\partial t'}-\theta\frac{\dot{L}(t')}{L(t')}\frac{\partial p(\theta,t')}{\partial\theta} \quad \text{.....(3.9)}$$

Comparing to the previous section, these two models have the same fluid momentum, local fluid mass balance, global mass balance theory, and initial and boundary conditions. The difference is that they apply different leak-off theories, which leads to different width-pressure equation. Same solution procedure to previous simulations will be used in this one.

3.3 Stability Criterion

For pressure dependent leak-off, the time-stepping algorithm is the same during fracture propagation. It is also estimated by equation (2.48). While during fracture recession, the size of the time step is limited to a preset maximum change of width between time steps.

3.4 Case Study

3.4.1 The Input Data

The PKN fracture model with pressure-dependent fluid leak-off rate is simulated by injecting fracturing fluid at a constant rate for 1000 seconds, and then shut-in the well to let the fracture recedes (Table 3.1).

Table 3.1 Input data for the pressure-dependent leak-off simulator

Power law constitutive constant, K	5.6×10^{-7} MPa·s
Power law fluid index, n	1
Injection rate, Q_0	4×10^{-3} m^3/s
Poisson's ratio, υ	0.2
Shear modulus, G	1×10^4 MPa
Fracture height, H	10 m
Mobility coefficient for reservoir fluid, $KAPPA$	8.36×10^{-6} m^2/ MPa·s
Interface pressure, λ_p	1.7 MPa
Poroelastic coefficient, η	0.15
Diffusivity coefficient, c	0.4 m^2/s
Injection time, t	1000 sec

The following plots show how the fracture length, width and pressure change during fracture propagation.

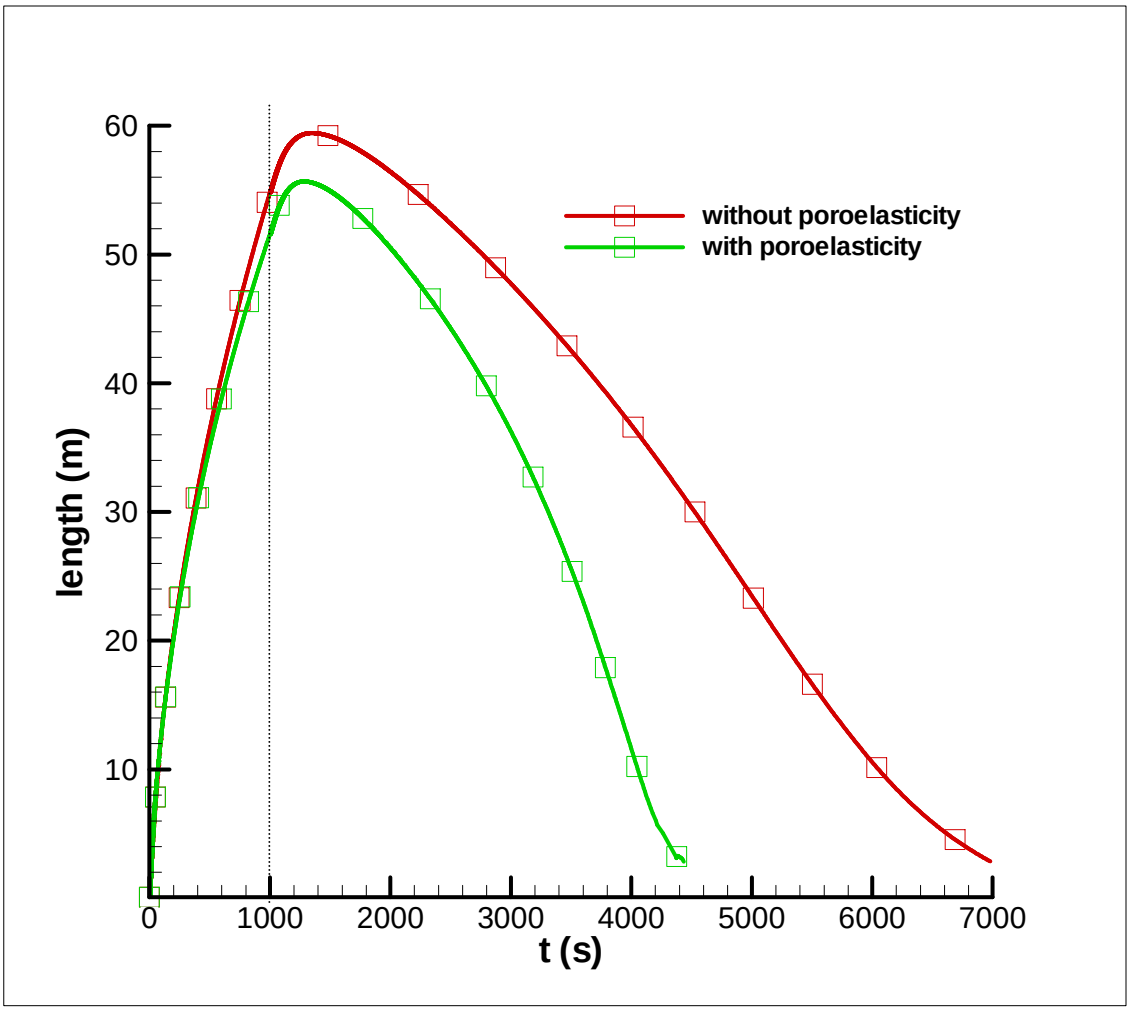

Fig. 3.2 Fracture length change history with pressure-dependent leak-off.

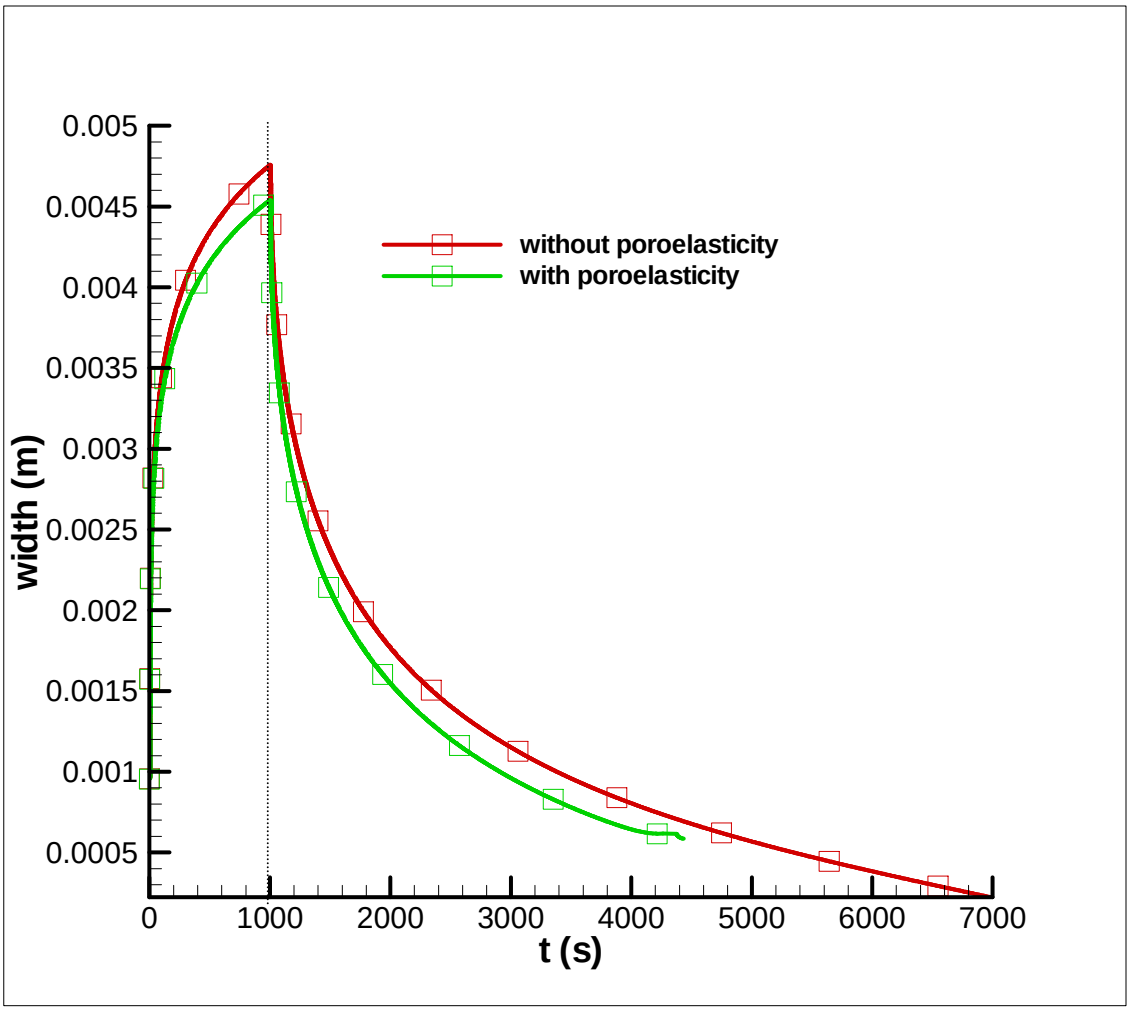

Fig. 3.3 Maximum fracture width change with time, with pressure-dependent leak-off.

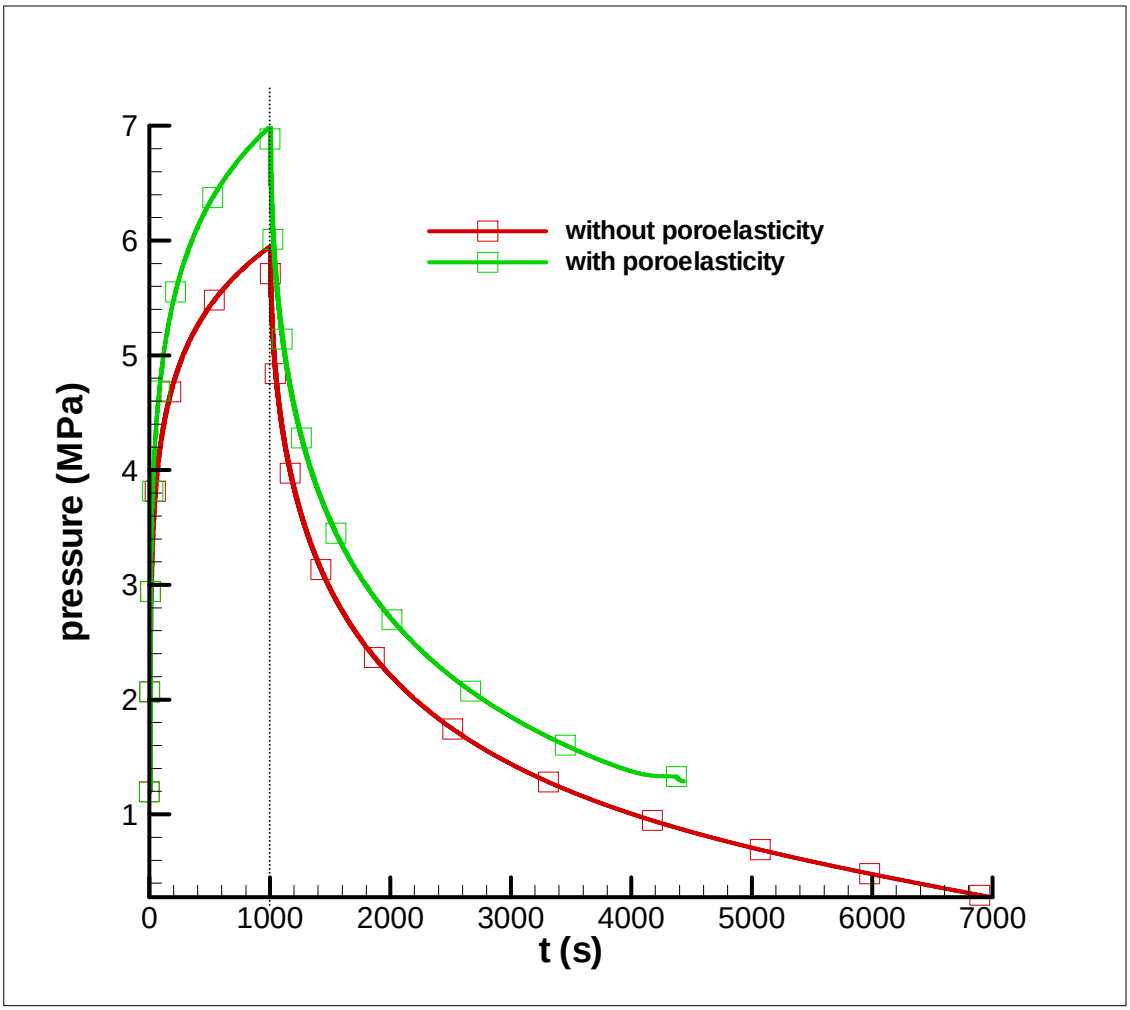

Fig. 3.4 Net fracturing pressure change history with time, with pressure-dependent leak-off.

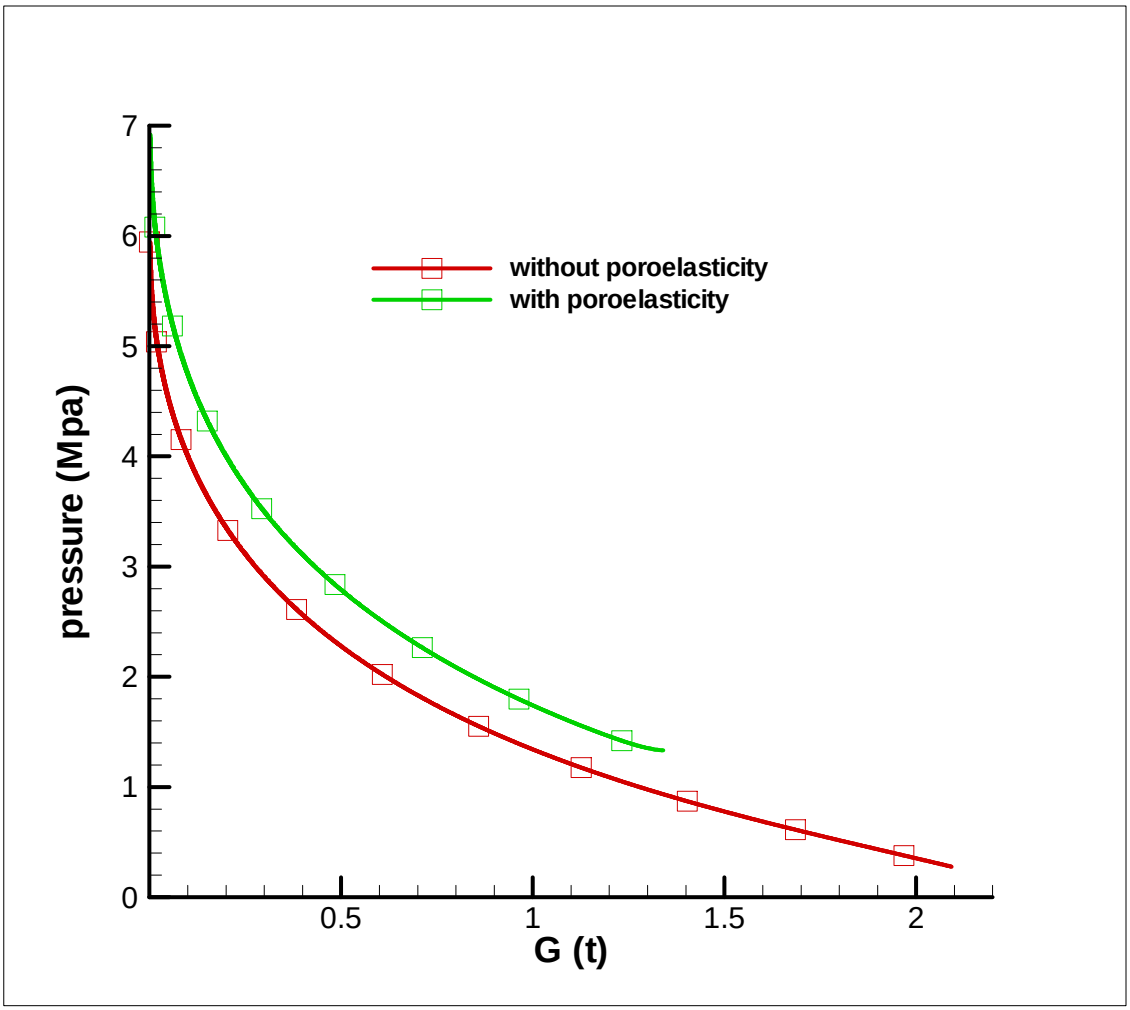

Fig. 3.5 The G-function curve.

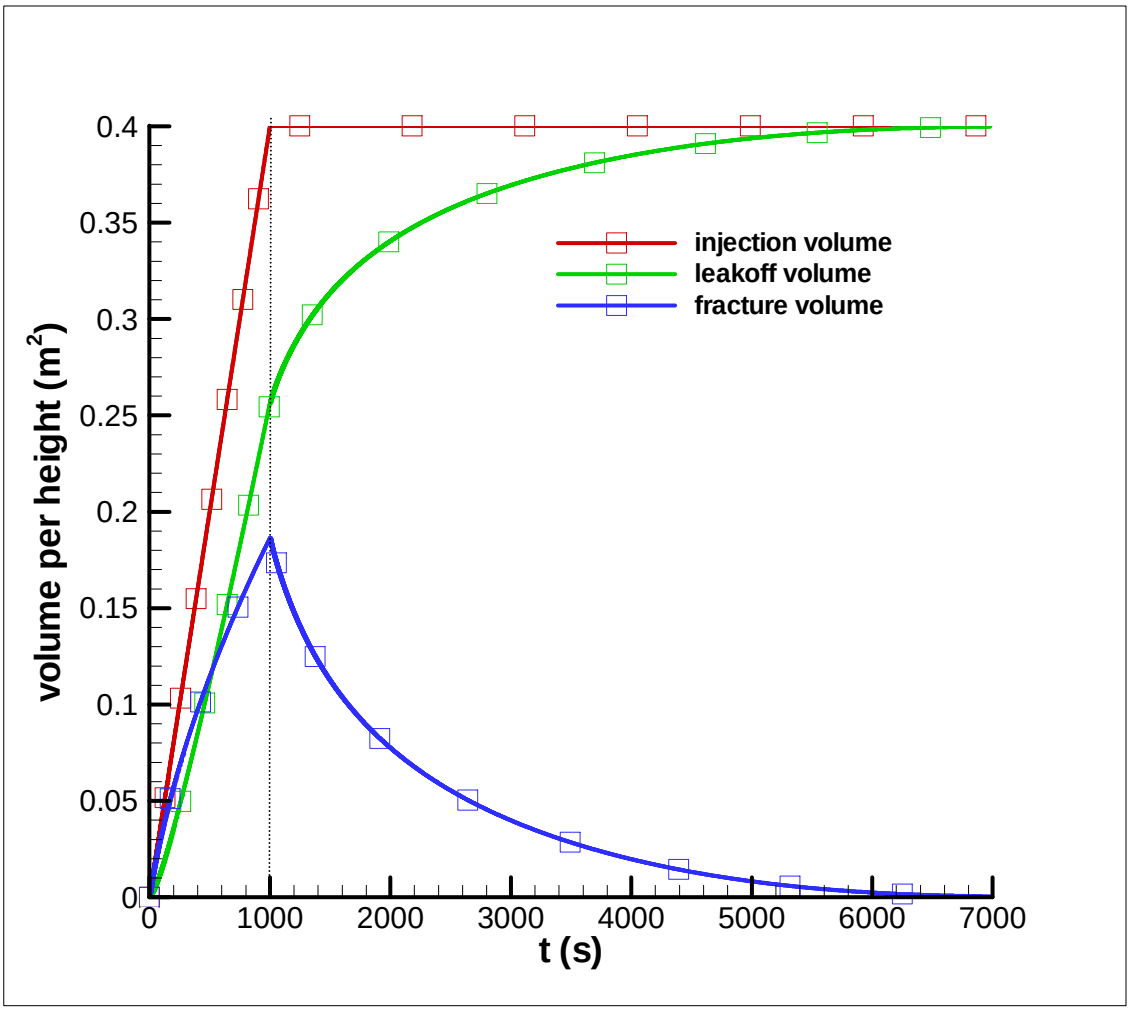

Fig. 3.6 The fracture, injection and leakoff fluid volume history without poroelasticity.

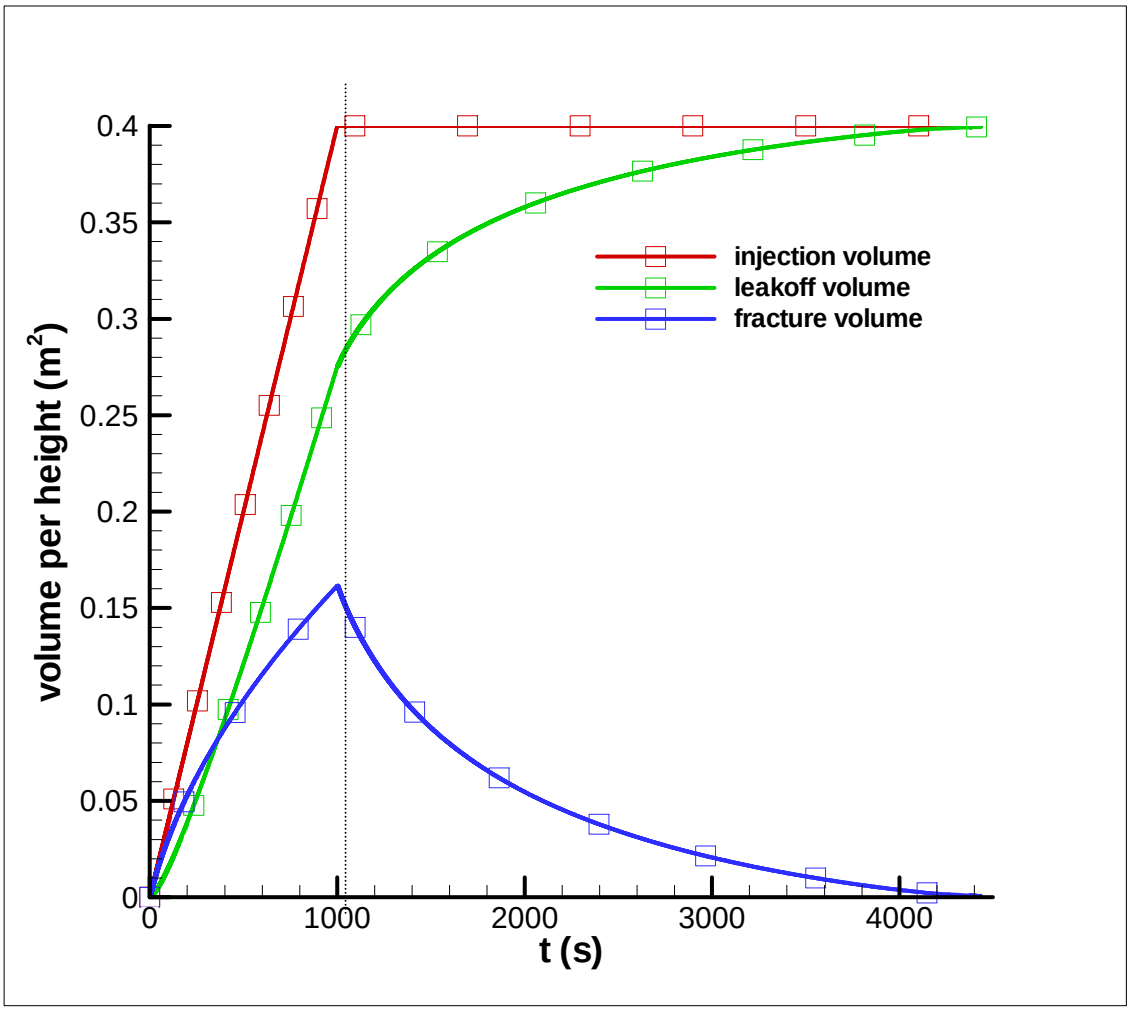

Fig. 3.7 The fracture, injection and leakoff fluid volume history with poroelasticity.

Comparing with Figs.2.8, 2.9 and 2.10, similar conclusion could be drawn from Figs.3.2, 3.3 and 3.4 shown above: fracture length, maximum width and fracturing pressure increase during the period of injection; fracture width and pressure decline sharply after shut-in; fracture length continues to increase after shut-in because it is continuously driven by the fluid pressure even after the fluid supply has stopped; and finally, they all decline gradually to zero when the fluid leak-off dominates the process.

In Figs. 3.2-3.4 the fracturing pressure increases with poroelastic effect in both the propagation and recession stages. While in Figs. 3.2 and 3.3, we observe that it will produce a smaller fracture length and width when poroelastic effect is included. Since the pumping time and the fluid injection rate in both simulations are the same, it is concluded that the poroelastic effect will force more fluid to the formation. And these conclusions are similar to the work done by Abousleiman 1991 (described in Appendix A.7). The effects of poroelasticity are expressed in the following aspects: poroelasticity causes a significant increase in the fracturing pressure and also causes a smaller fracture volume with smaller maximum fracture length and width. The G-function plot in Fig. 3.5 is used a lot in the industry. The fluid leaks into formation faster as the pressure is higher in the fracture with poroelasticity, comparing Fig. 3.6 with 3.7 that the fracture closure time is shorter in Fig. 3.7.

4. SENSITIVITY ANALYSIS OF FLUID AND FORMATION PROPERTY

4.1 Introduction

In oil and gas industry, in order to get maximum fracture conductivity and to produce hydrocarbon out of the underground as much and fast as possible, it's necessary to optimize the process of hydraulic fracturing of a specific kind of reservoir according to both the fluid and formation character.

In this section, the sensitivity of mechanics properties of fluid and rock to the fracture geometry and fracturing pressure is analyzed according to the simulator described in the previous sections. The effects of fluid viscosity, shear modulus of rock, and the fluid leak-off coefficient on fracture geometry and pressure are studied. To clearly show these effects, the simulator described in section 2 with elastic formation is applied.

4.2 Fluid Viscosity

The effects of fluid viscosity on the fracture geometry and fracturing pressure is modeled by taking into account the same kind of formation, and inputting the power law constitutive constant to be 5.6×10^{-9} MPa·s$^{0.8}$, 3.08×10^{-8} MPa·s$^{0.8}$, 5.6×10^{-8} MPa·s$^{0.8}$, 3.08×10^{-7} MPa·s$^{0.8}$, 5.6×10^{-7} MPa·s$^{0.8}$, 3.08×10^{-6} MPa·s$^{0.8}$, 5.6×10^{-6} MPa·s$^{0.8}$, 3.08×10^{-5} MPa·s$^{0.8}$,and 5.6×10^{-5} MPa·s$^{0.8}$ (Table 4.1) and running these cases respectively:

Table 4.1 Input data to examine the effect of fluid viscosity

Power law constitutive constant, K	$5.6\times10^{-9}, 3.08\times10^{-8}, 5.6\times10^{-8}, 3.08\times10^{-7}, 5.6\times10^{-7}, 3.08\times10^{-6}, 5.6\times10^{-6}, 3.08\times10^{-5}$ MPa·s$^{0.8}$
Power law fluid index, n	0.8
Injection rate, Q_0	4×10^{-3} m^3/s
Poisson's ratio, υ	0.2
Shear modulus, G	1×10^4 MPa
Fracture height, H	10 m
Leak-off coefficient, C_l	6.3×10^{-5} m/s$^{0.5}$
Interface pressure, λ_p	1.7 MPa
Poroelastic coefficient, η	0.25
Diffusivity coefficient, c	0.4 m^2/s
Injection time, t	1000 sec

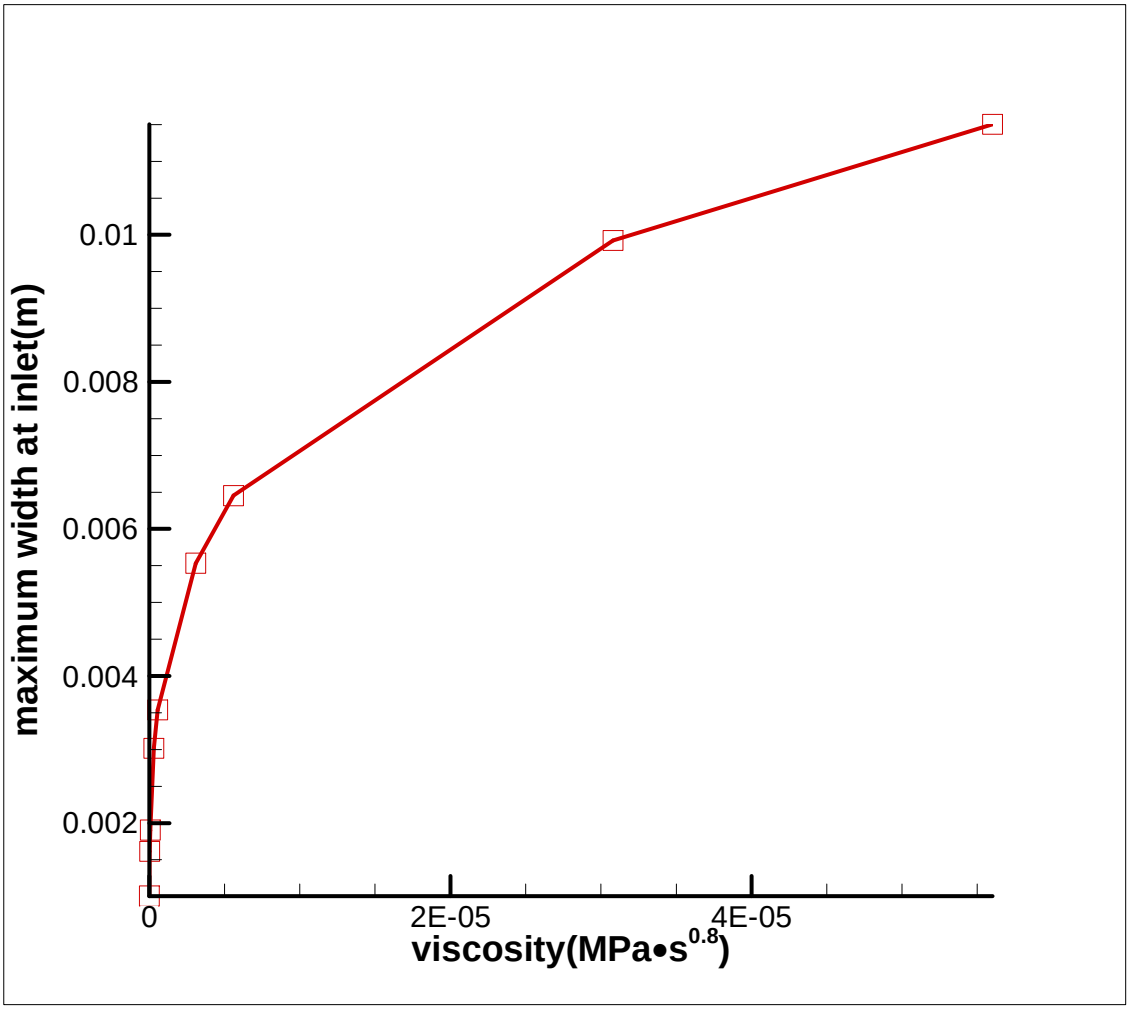

Fig. 4.1 Fracture maximum width changes with different fluid viscosity.

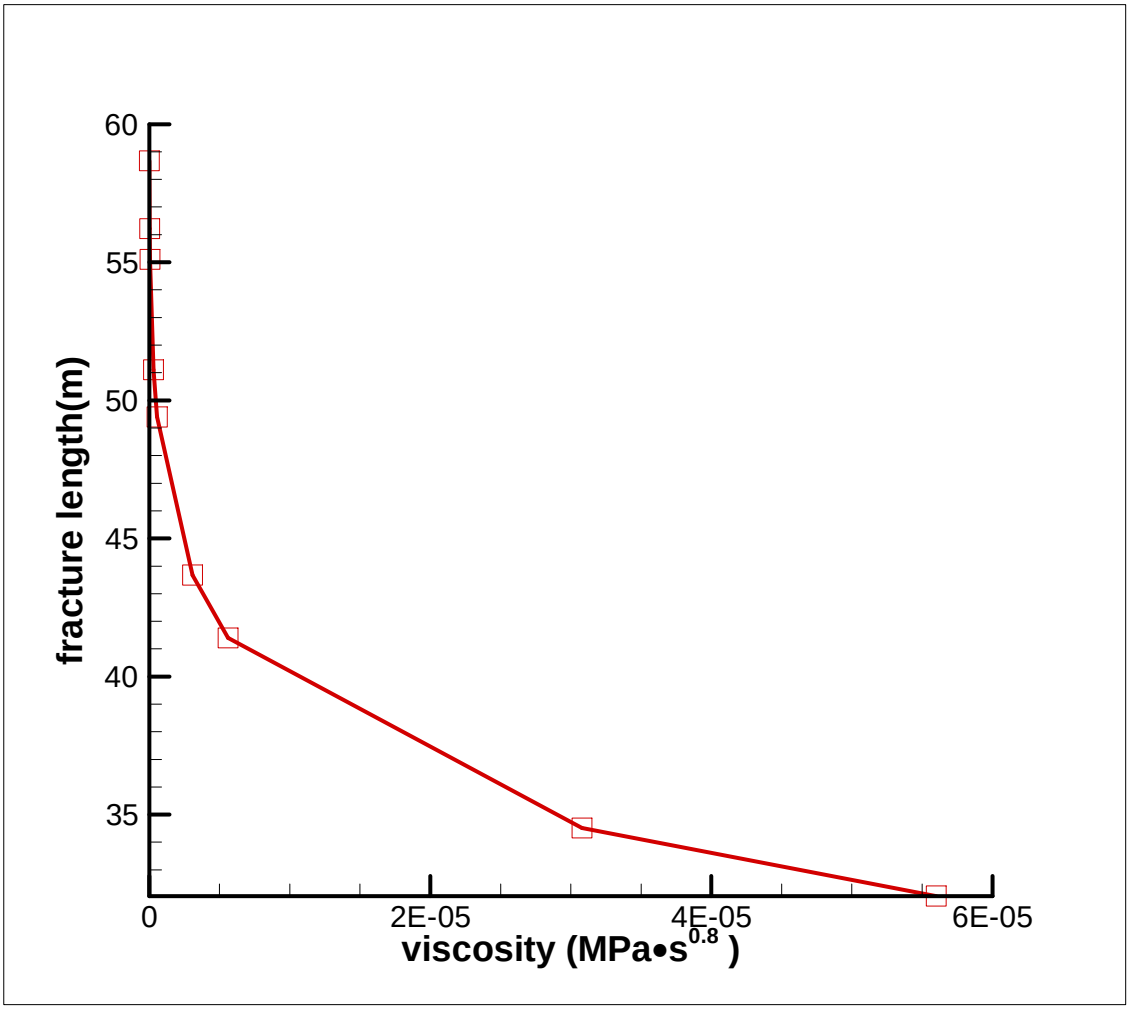

Fig. 4.2 Fracture length changes with different fluid viscosity.

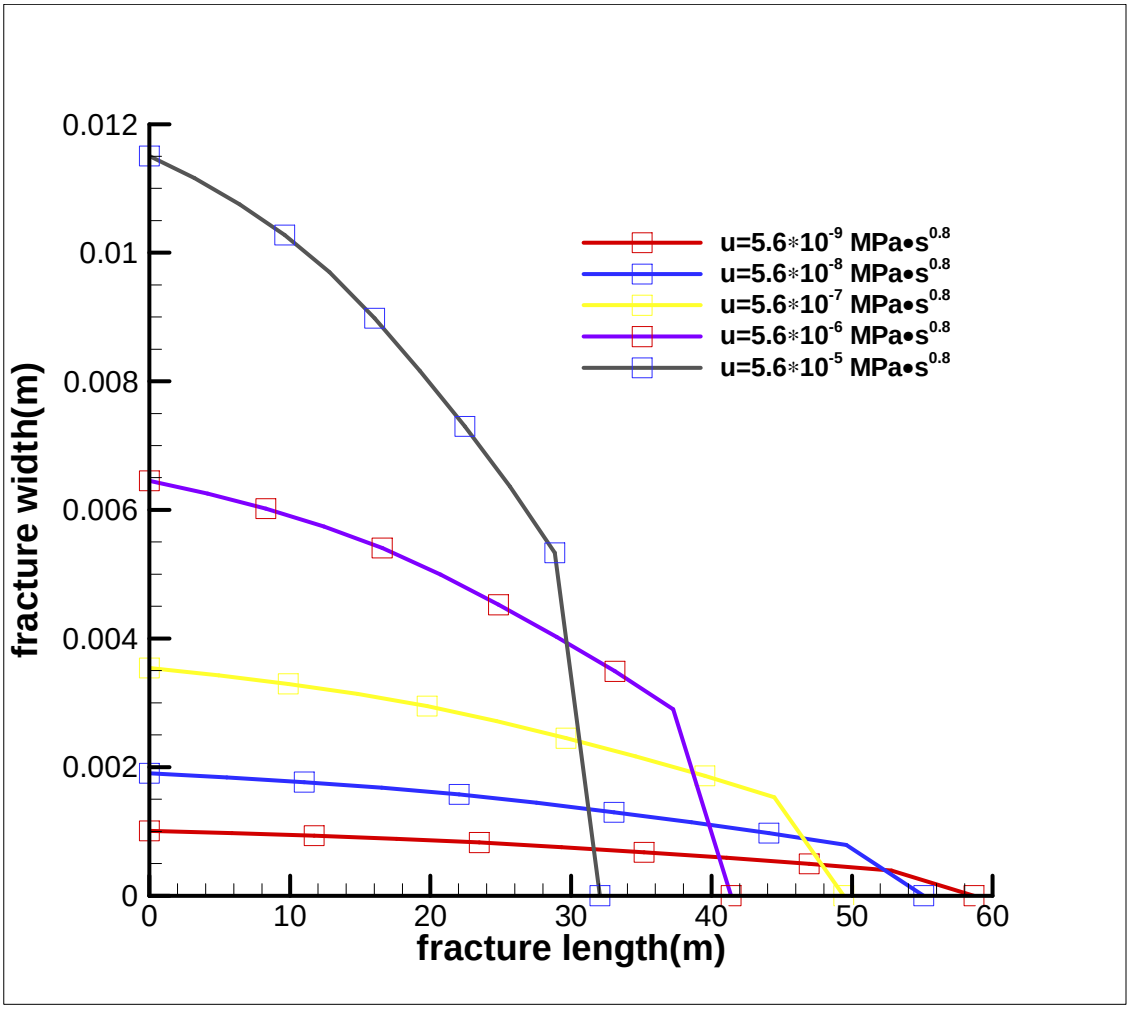

Fig. 4.3 Fracture geometry changes with different fluid viscosity.

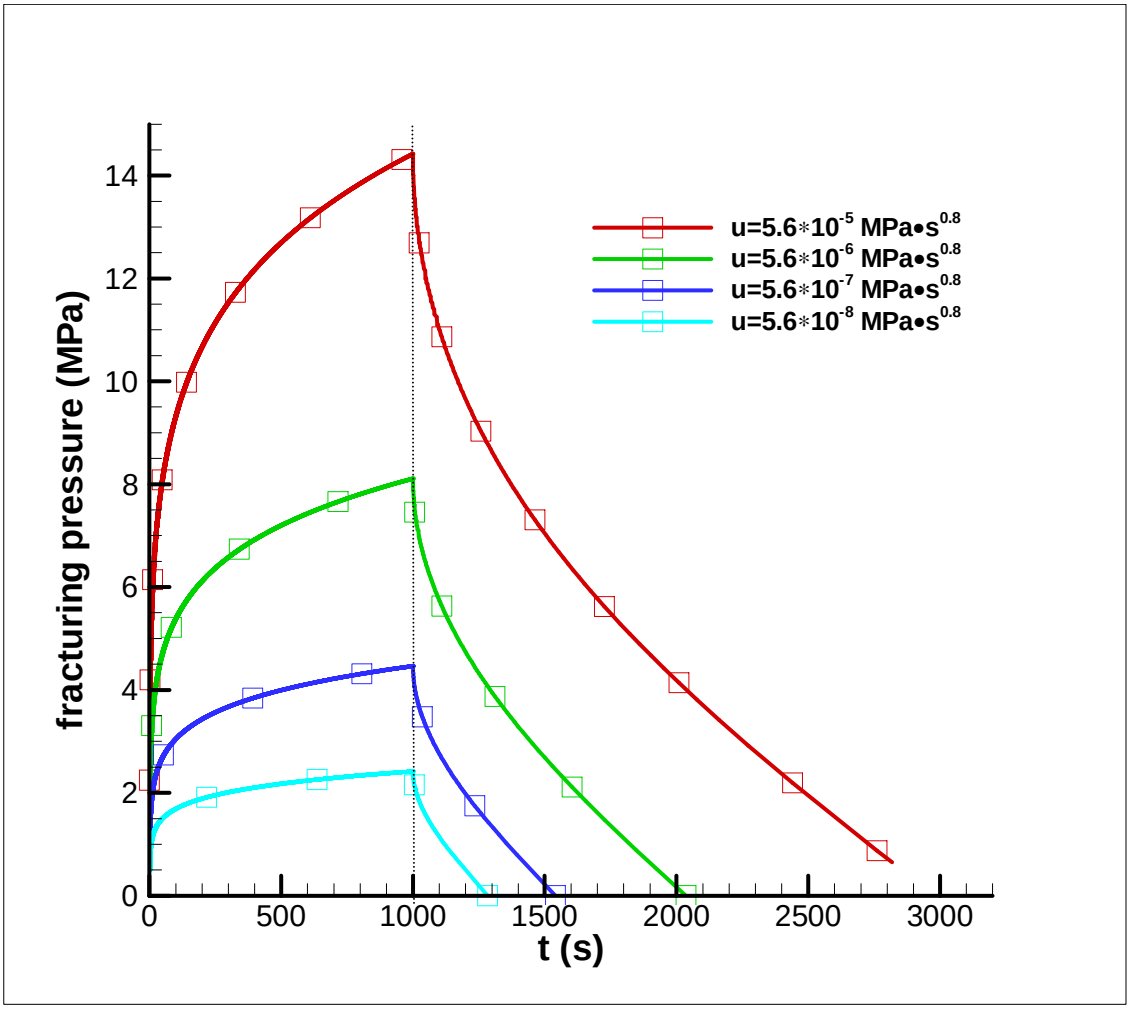

Fig. 4.4 Fracturing pressure changes with different fluid viscosity.

Fig. 4.1 and Fig. 4.2 show that the fracture width increases with increasing of the fluid viscosity and the fracture length decreases with the increasing of fluid viscosity. Fig. 4.3 indicates that a wider and shorter fracture will be produced with higher fluid viscosity and a narrower and longer fracture will be produced with lower fluid viscosity. Fig. 4.4 tells that a higher pumping pressure is required to deal with higher viscosity fracturing fluid under the same formation and operation conditions. These results are in a good agreement with the industry practice.

4.3 Formation Shear Modulus

Considering different types of reservoirs, we examined the effect of formation shear modulus on the fracture geometry and fracturing pressure, while keeping the pumping fracturing fluid and operation conditions unchanged. Inputting the shear modulus to be 1×10^{3} MPa, 1×10^{4} MPa and 1×10^{5} MPa (Table 4.2) and running these cases respectively, we get the following result:

Table 4.2 Input data to examine the effect of rock shear modulus

Power law constitutive constant, K	5.6×10^{-7} MPa·s$^{0.8}$
Power law fluid index, n	0.8
Injection rate, Q_0	4×10^{-3} m^3/s
Poisson's ratio, υ	0.2
Shear modulus, G	$1\times10^3, 1\times10^4, 1\times10^5$ MPa
Fracture height, H	10 m
Leak-off coefficient, C_l	6.3×10^{-5} m/s$^{0.5}$
Interface pressure, λ_p	1.7 MPa
Poroelastic coefficient, η	0.25
Diffusivity coefficient, c	0.4 m^2/s
Injection time, t	1000 sec

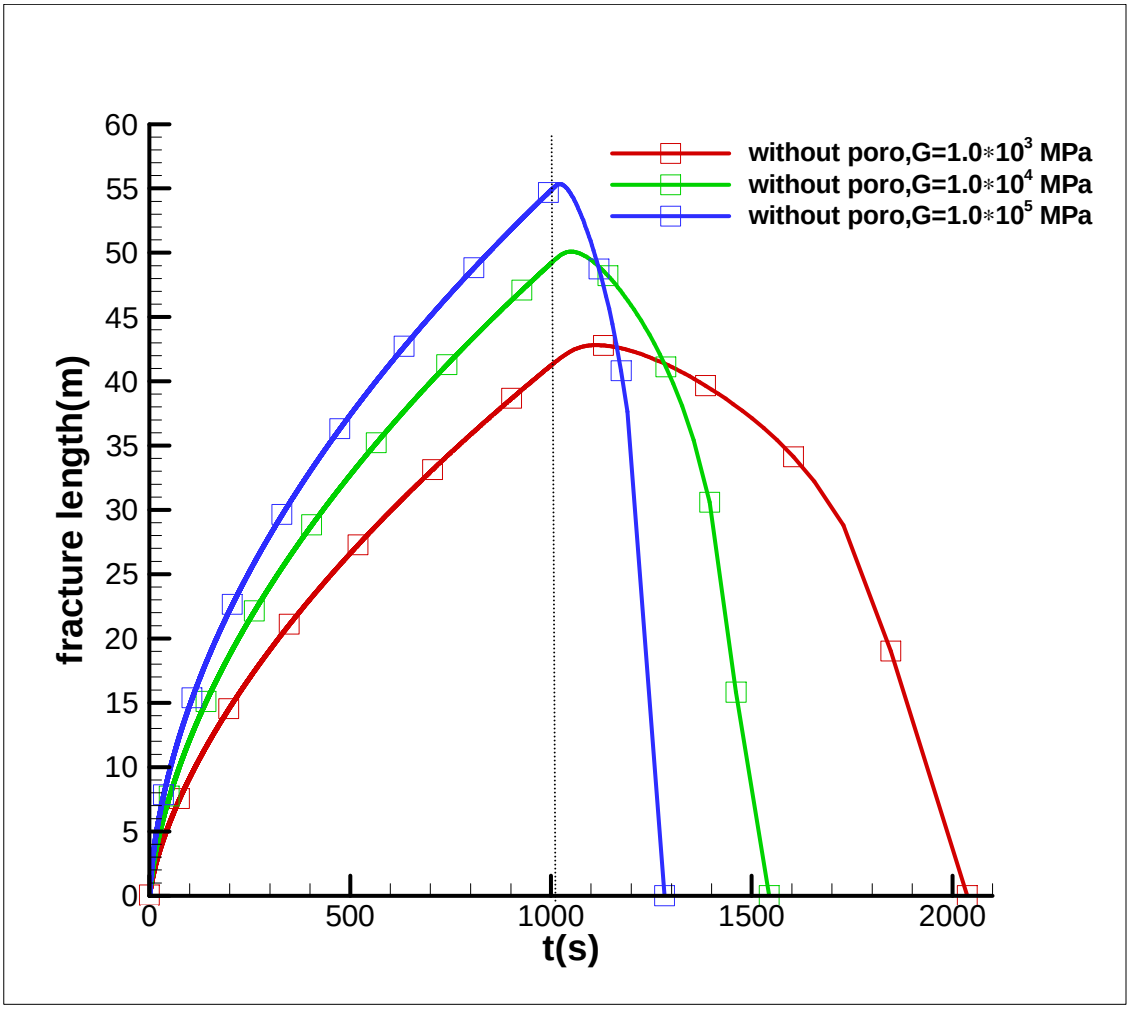

Fig. 4.5 The effect of shear modulus on fracture length, without poroelasticity.

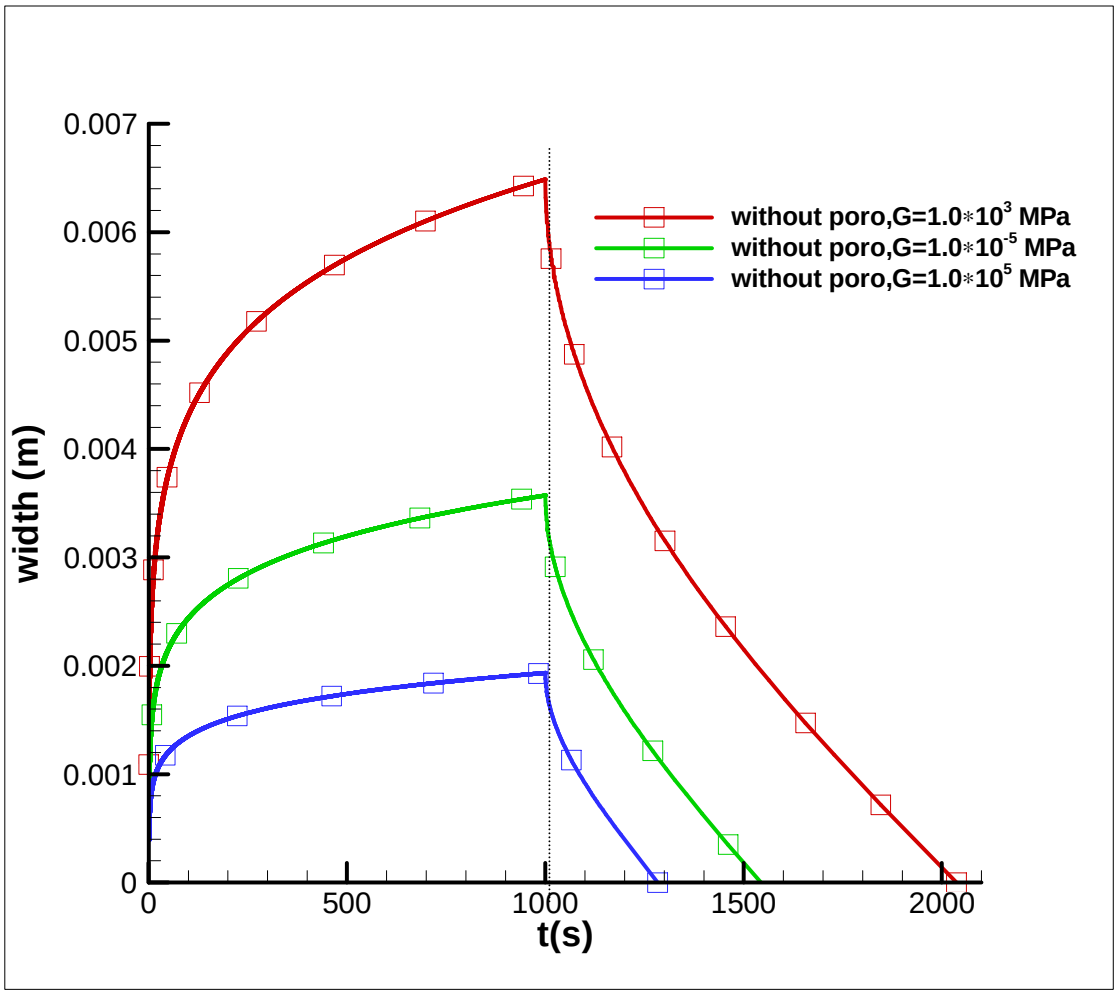

Fig. 4.6 The effect of shear modulus on maximum fracture width, without poroelasticity.

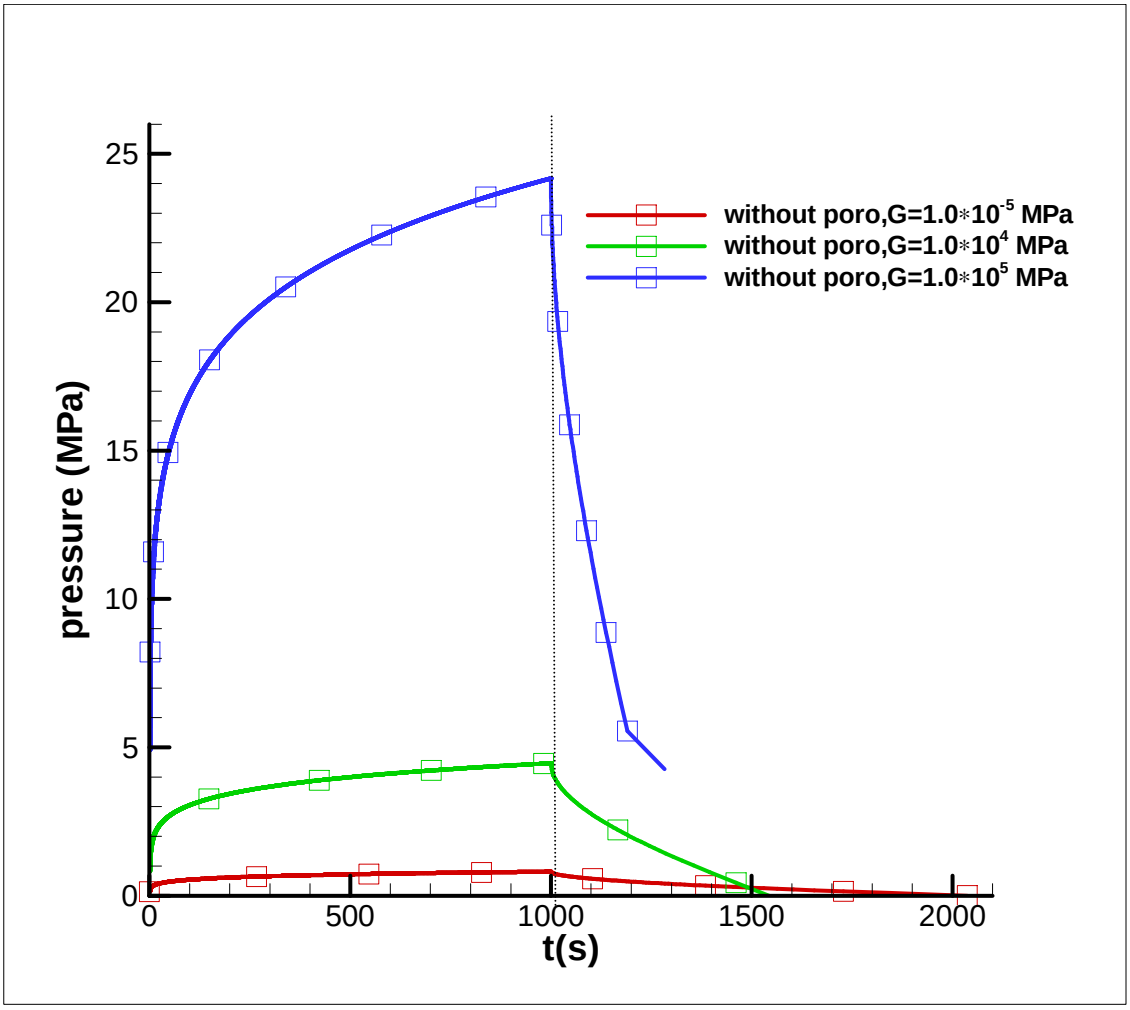

Fig. 4.7 The effect of shear modulus on fracturing pressure , without poroelasticity.

Figs. 4.5 and 4.6 express that a shorter and wider fracture will be generated when the formation is soft with low shear modulus, while a longer and narrower fracture will be produced when the formation is hard with high shear modulus, using the same kind of fracturing fluid and operation conditions. And also as displayed in Fig. 4.7, higher fracturing pressure is required to fracture harder reservoirs.

4.4 Fluid Leak-off Coefficient

Fluid leak-off coefficient is a parameter dependent on both fluid and formation properties. Here the effect of fluid leak-off coefficient on the fracture geometry and fracturing pressure is examined by keeping the fluid and rock properties unchanged. Inputting the leak-off coefficient to be 2.3×10^{-5}, 6.3×10^{-5} and 1.3×10^{-4} m/s$^{0.5}$ (Table 4.3) and running these cases respectively, the following results are obtained:

Table 4.3 Input data to examine the leak-off coefficient

Power law constitutive constant, K	5.6×10^{-7} MPa·s$^{0.8}$
Power law fluid index, n	0.8
Injection rate, Q_0	4×10^{-3} m^3/s
Poisson's ratio, υ	0.2
Shear modulus, G	1×10^4 MPa
Fracture height, H	10 m
Leak-off coefficient, C_l	$2.3\times10^{-5}, 6.3\times10^{-5}, 1.3\times10^{-4}$ m/s$^{0.5}$
Interface pressure, λ_p	1.7 MPa
Poroelastic coefficient, η	0.25
Diffusivity coefficient, c	0.4 m^2/s
Injection time, t	1000 sec

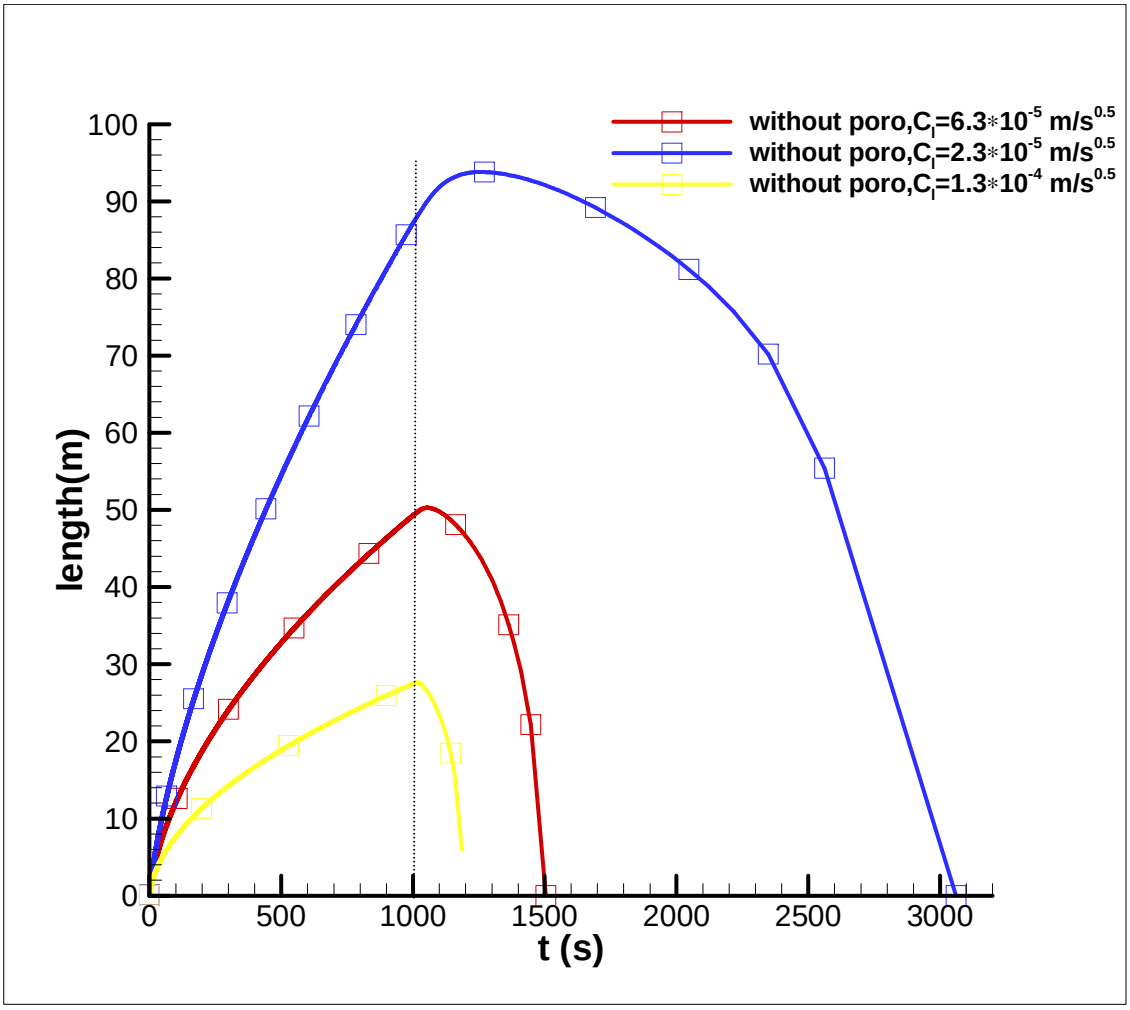

Fig. 4.8 The effect of leak-off coefficient on fracture length, without poroelasticity.

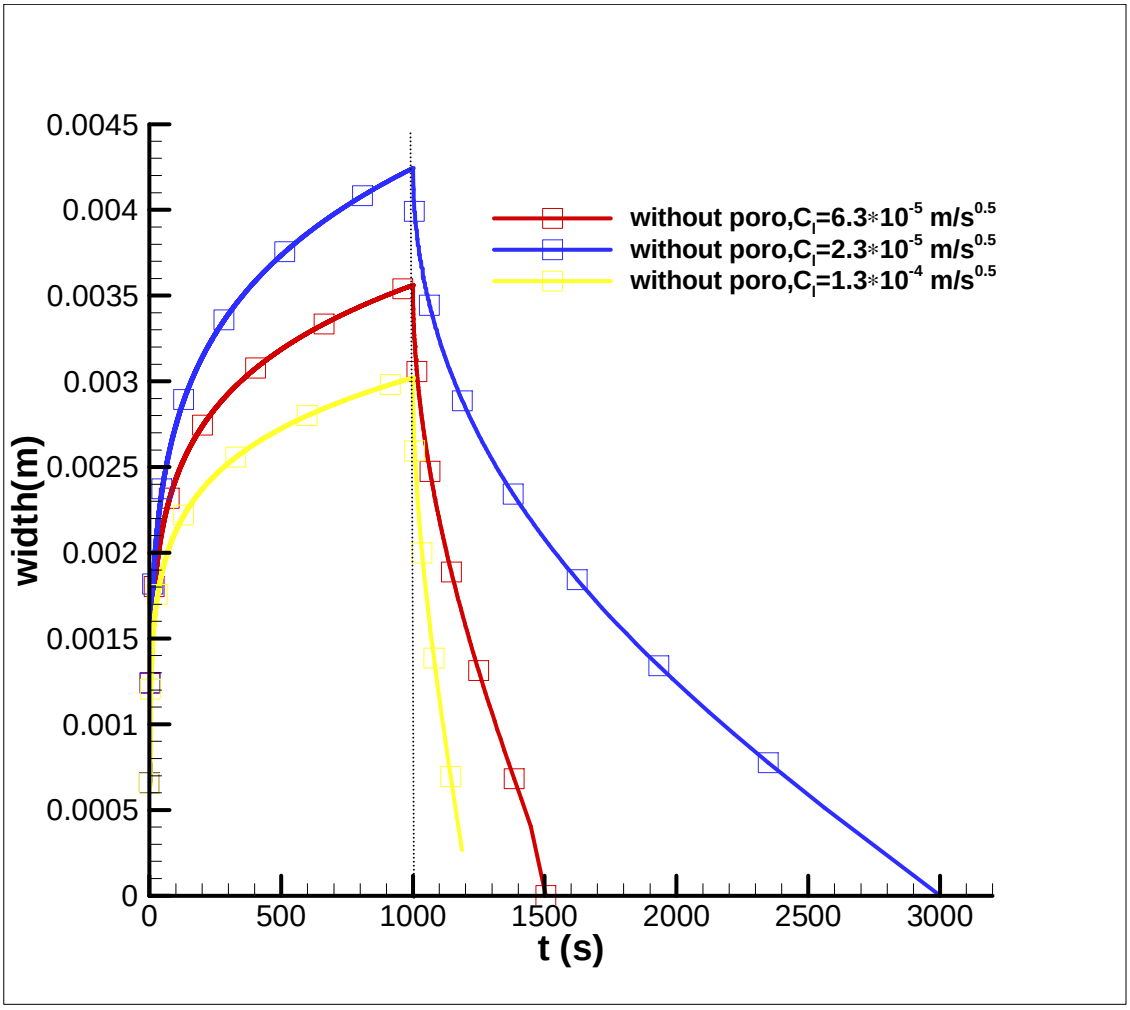

Fig. 4.9 The effect of leak-off coefficient on maximum width, without poroelasticity.

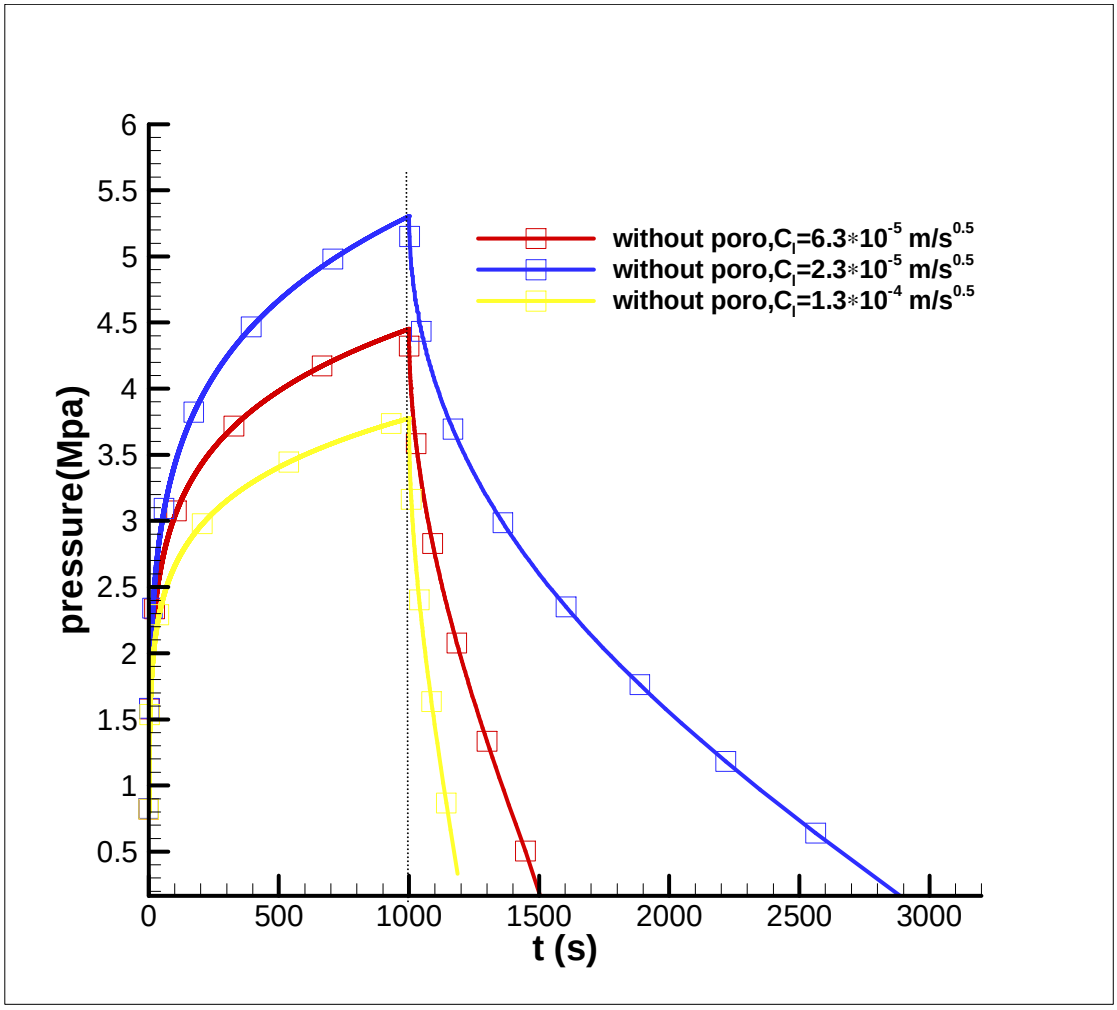

Fig. 4.10 The effect of leak-off coefficient on fracturing pressure, without poroelasticity.

As is shown in Figs. 4.8, 4.9, and 4.10, the fracture length, width, fracturing pressure, and the fracture closure time increased as the leak-off coefficient decreased. The leak-off coefficient has different effect from the fracturing fluid viscosity and formation shear modulus in that, small leak-off coefficient produces long and wide fractures with high fracturing pressure, while large leak-off coefficient produces short and narrow fractures with low fracturing pressure.

5. FORMATION PERMEABILITY DETERMINATION BY MICRO OR MINI HYDRAULIC FRACTURING

5.1 Introduction

Pressure transient derived from well tests in oil/gas reservoirs is a valuable piece of information to estimate the reservoir characteristics. This study presents a theory and analysis for a post fracture pressure transient test, which is known as the impulse pressure test (Gu et al. 1993). A program is developed based on their work to interpret the pressure decay response after shut-in. The analysis is an injection/falloff test used to determine formation permeability, by injecting a small amount of fluid into the formation to create a short fracture and then shutting in with the fluid locked in the formation. This kind of fracture is able to pass through the damaged near wellbore zone and expose a large formation area to the flow, so the permeability determined using this method should be more close to the actual permeability of the reservoir than other conventional pressure transient tests. On the other hand, fracturing might be difficult to avoid during injection into low permeability formations. In addition, this theory can be used to interpret the pressure data.

The present impulse fracture theory is based on the distribution of the source solution of the diffusion equation. The fracture is driven as a hydraulic fracture and then shut in. The source is distributed along the actual trajectory of the fracture with its intensity prescribed by the fracturing fluid leak off rate.

For simplicity, the fracture created in the test is considered to be a PKN model fracture, and it employs the previous hydraulic fracture simulator which records the fracture trajectory and the leak off history for both fracture propagation and recession stages. The sources are distributed accordingly until the fracture closes at the wellbore and no more fluid leak-off into the formation takes place. Then the pressure falloff is continuously simulated until the reservoir pressure is approached. This numerically simulated pressure transient data provides important information to determine the formation permeability, using the type-curve-analysis of the asymptotic behavior during intermediate and large times (see Fig. 5.1 for the hydraulic fracture flow regimes).

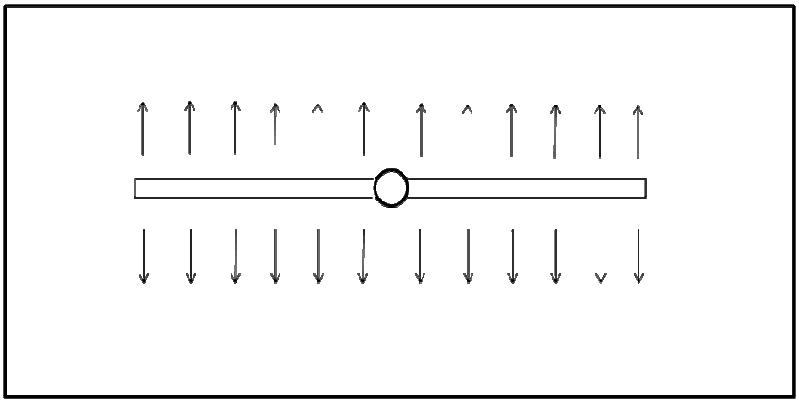

Small time linear flow

⇩

Fig. 5.1 Hydraulic fracture flow regimes.

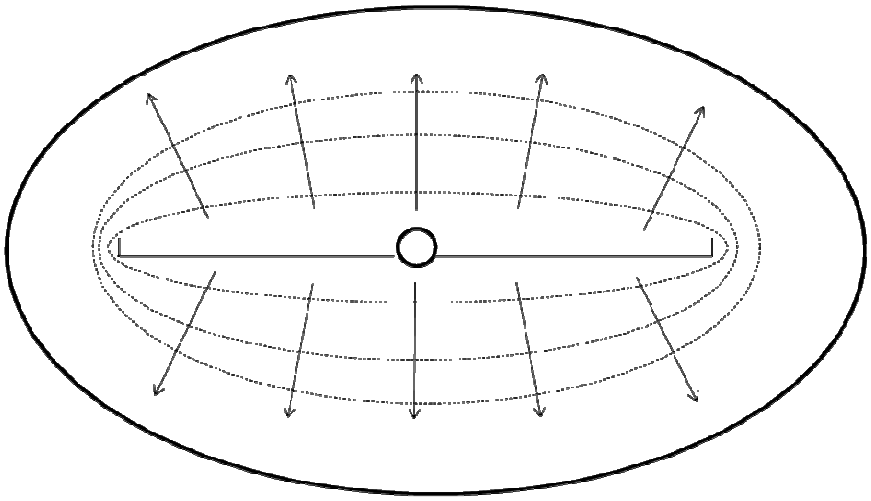

Intermediate time elliptical flow

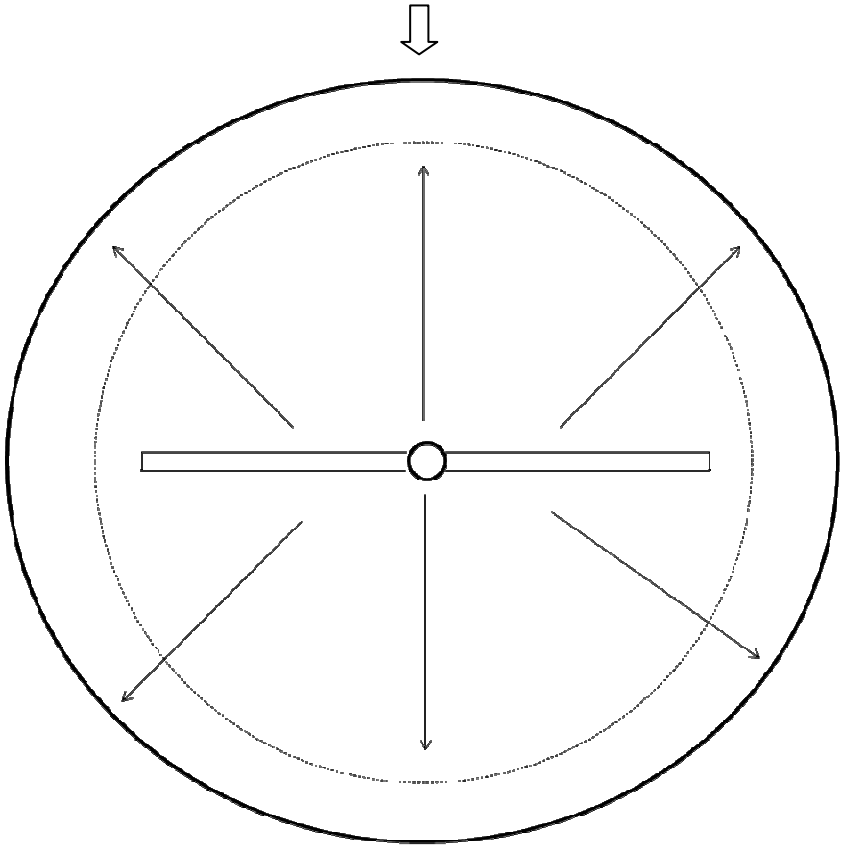

Large time radial flow

Fig. 5.1 Continued.

5.2 Impulse Fracture Pressure Transient Model

Considering a homogeneous pay zone bounded by two impermeable ones, both the wellbore section and the created PKN model fracture are assumed to extend to the full height of this formation. This geometry allows for the use of the two-dimensional (in horizontal directions) diffusion equation in the formation

$$\nabla^2 p = \frac{1}{c}\frac{\partial p}{\partial t} \qquad \text{.....(5.1)}$$

where p is the 'net pressure', $p = p_f - p_o$, and p_f is the flow pressure, p_o is the hydrostatic virgin pore pressure ; ∇^2 is Laplace's operator in two dimensions, and c is the reservoir diffusivity coefficient.

For this problem, it is postulated that the effect of hydraulic fracturing upon the reservoir pressure is equivalent to the distribution of fluid sources at the fracture surfaces with their strength characterized by the fluid leak off rate. A schematic fracture propagation history is shown in Fig. 5.2. The vertical axis represents the fracture length, and the horizontal one is the elapse time since the initiation of pumping. The fracture is zero in length at time $t = 0$. The length increases over time before pumping ceases at time t_p by shutting off the valve to lock the fluid in the down hole. The fracture will continue to propagate for a short while until it reaches a maximum length L_m. Then it starts to recede, and eventually closes at the wellbore at time t_c.

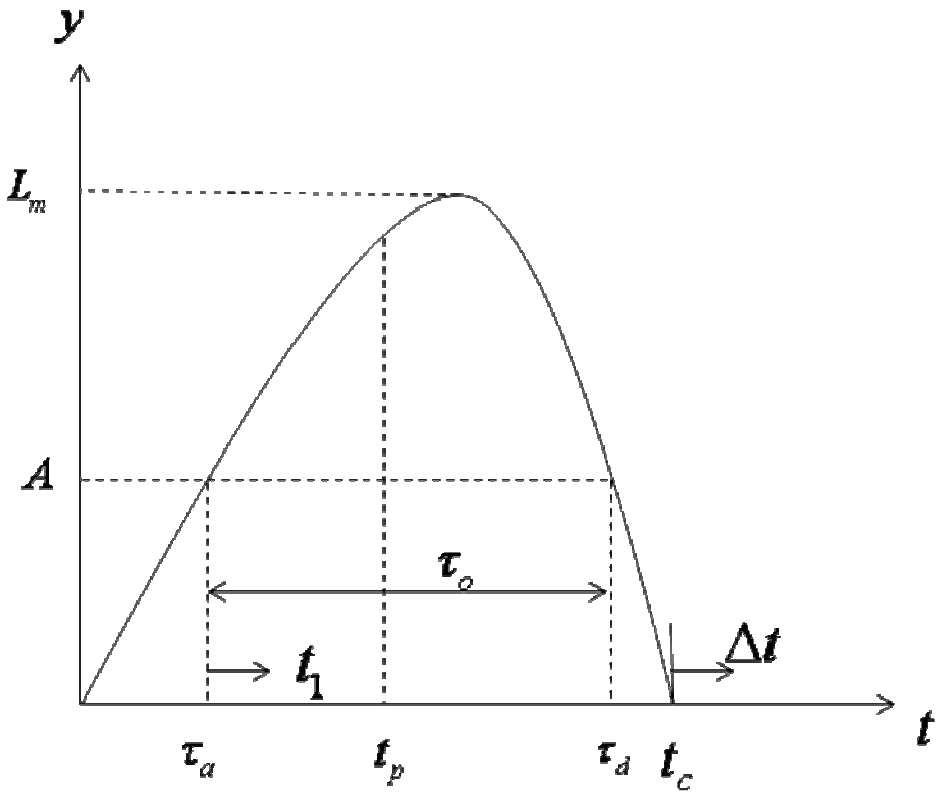

Fig. 5.2 The schematic fracture length history.

As shown in Fig. 5.2, it assumes that as the fracture arrives at point A at time $t=\tau_a$, an injection source is turned on at that location and that time. During fracture recession, the fracture is closed at point A at time $t=\tau_d$, and the injection source is turned off. At the fracture closure time $t=t_c$, the fracture is closed at the wellbore and the entire volume of injected fluid is lost into the formation. For formation permeability determination, we are interested in the pressure behavior during the post-closure time. The pressure diffusion at that time can take place both in the porous medium and the 'closed' fracture. For simplicity, however, we assume that the closed fracture has zero

conductivity. This assumption is necessary for two reasons: it is difficult to estimate the conductivity of a closed fracture, and more simple theories can be derived (Abousleiman et al. 1994), which lead to graphical procedures for parameters determination that are most useful for field engineers. Based on the 'straight line methods', the conventional type-curve analysis yields some traditional behaviors, such as the -1slope; and also new behaviors, such as -2 and +1 slopes, when plot the pressure versus normalized time.

Without the complication of fracture conductivity, the post closure pressure behavior can be simulated by the distribution of fluid sources with known intensity (which must be calculated beforehand by the previous numerical simulator). Considering an instantaneous point source with a unit fluid volume injection, the influence of pressure on the reservoir is given by the following equation (Carslaw and Jaeger 1956):

$$p(r,t)=\frac{1}{4\pi\kappa t}e^{-r^2/4ct} \qquad \text{.....(5.2)}$$

where r is the radial distance, t is the elapsed time since injection, and $\kappa = k/\mu$ is the mobility coefficient, with k is the formation permeability and μ is the fluid viscosity. Equation (5.2) satisfies the diffusion equation (5.1). The point source can be distributed over the fracture trajectory during the time interval of the fracture exposure (from the arrival of the fracture tip at τ_a to its departure time at τ_d), at the strength of the leak off velocity u. The influence of the sources on the reservoir pressure at any point (x, y) in the domain, at a time $t \geq t_c$, is obtained by applying Duhamel's principle of superposition as expressed in the following equation:

$$p(x,y,t)=\frac{1}{4\pi\kappa}\int_{-L_m}^{L_m}\int_{\tau_a(x')}^{\tau_d(x')}u(x',t')\frac{e^{-r^2/4c(t-t')}}{t-t'}dt'dx' \quad \text{.....(5.3)}$$

where $r=\sqrt{(x-x')^2+(y-y')^2}$. Notice that both τ_a and τ_d are functions of the location x' along the fracture, and the fluid leak-off velocity u is a function of both the location x' and the time t' between τ_a and τ_d, and that the integration is performed from $-L_m$ to $+L_m$ to take care of the two wings of the fracture.

The leak off intensity u can be obtained from Carter's leak off theory which is a traditional industry model same to the one adopted in the previous PKN fracture simulator and shown as following equation:

$$u(x',t')=\frac{2C_l}{\sqrt{t'-\tau_a(x')}} \quad \text{.....(5.4)}$$

in which C_l is Carter's leak-off coefficient.

Since the pressure during the post-fracture-closure time will examined,

$$\Delta t=t-t_c \quad \text{.....(5.5)}$$

it is more convenient to rewrite (5.3) by shifting the time frame to t_c. In addition, in this study we are only interested in the solution at the origin (0, 0), where the borehole is located, because this is the only location where fracturing pressure is observable in reality. Equation (5.3) becomes

$$p(\Delta t)=\frac{1}{2\pi\kappa}\int_{0}^{L_m}\int_{0}^{\tau_o(x')}u(t')\frac{e^{-x'^2/4c(t_1(x')-t')}}{t_1(x')-t'}dt'dx' \quad \text{.....(5.6)}$$

in which

$$\tau_o(x') = \tau_d(x') - \tau_a(x') \quad \text{.....(5.7)}$$

is the total fracture exposure time at the location x', and

$$t_1(x') = \Delta t + t_c - \tau_a(x') \quad \text{.....(5.8)}$$

is the time measured since the arrival of the fracture τ_a (see Fig. 5.2). The leak-off is given as

$$u(t') = \frac{2C_l}{\sqrt{t'}} \quad \text{.....(5.9)}$$

we noticed that in (5.6) the integration is performed only over one wing by taking advantage of the character of symmetry. Equations (5.6) and (5.9) now form the basis of our analytical solution.

In Equation (5.6), the fracture arrival and departure time can be determined by the previous numerical simulator according to the inverse function $\tau(L) = L^{-1}(\tau)$. For the PKN model simulation, the $L(t)$ record is given in a digitized form. $\tau_a(x)$ and $\tau_d(x)$ can be easily extracted by interpolation.

Once the length history is available, we can read the maximum length L_m from the record. The length is then subdivided into a number of segments with a size of ΔL. If the segment ΔL is small enough, we can treat the line source approximately as a point source located at the center of the segment x_i, with the strength of the source given by $u(t')\Delta L$. This approximation turns the integration with respect to x' in (5.6) into a summation expressed as following:

$$p(\Delta t)=\frac{\Delta L}{2\pi\kappa}\sum_{i=1}^{n}\int_{0}^{\tau_o(x_i)}u(t')\frac{e^{-x_i^2/4c(t_1(x_i)-t')}}{t_1(x_i)-t'}dt' \quad \text{.....(5.10)}$$

where n is the number of source segments. Equation (5.10) is then numerically integrated by Gaussian quadrature, which can therefore predicts decline of the pressure happened after fracture closure in the wellbore.

5.3 Radial Flow Theory

Radial flow pattern in well testing has been observed and investigated by many researchers (Agarwal et al. 1974; Horner 1951; Soliman 1986). Useful type-curve procedures have been devised. Radial flow takes place naturally in a borehole injection or production. It is demonstrated that the radial pattern also appeared in fractured wells (Economides and Nolte 1989; Gringarten and Ramey 1974) after a long time development.

5.3.1 Large Time Asymptotic Behavior

This research shows that the radial flow behavior is retrievable in the induced hydraulic fracturing operation. A large time range is necessary to observe this behavior. It is noticed that as $t\to\infty(\Delta t\to\infty)$, t_1 in (5.8) behaves as $t_1(x')\approx\Delta t$, and also $t_1-t'\approx\Delta t$, because as t increases, only Δt will increase with all the other quantities remain bounded. As a consequence, the exponential term in (5.6) approaches to 1 and the equation can be simplified as:

$$p(\Delta t) \approx \frac{1}{2\pi\kappa\Delta t}\int_0^{L_m}\int_0^{\tau_o(x')} u(t')dt'dx' \quad \text{.....(5.11)}$$

Notice that Δt is removed from the integrand since it is independent of the parameters $x'$and t'. Considering that the entire volume of fluid injected is lost into the formation at the fracture closure (zero fracture volume at that time), it is found that

$$\int_{-L_m}^{L_m}\int_0^{\tau_o(x')} u(t')dt'dx' = \frac{Q_o t_p}{H} \quad \text{.....(5.12)}$$

where Q_o is the constant injection rate at the wellbore. Combining equations (5.11) and (5.12), the asymptotic pressure transient law is obtained:

$$p(\Delta t) \approx \frac{Q_o t_p}{4\pi\kappa H}\Delta t^{-1} \quad \text{as } t \to \infty \quad \text{.....(5.13)}$$

The foregoing equation suggests that the -1 slope should appear at large time on the plot of $_p$ versus Δt on a log-log scale. It is of interest in this research to compare the result in (5.13) with the point source solution of (5.2). It is noted that at $r = 0$ and $t > 0$, equation (5.2), which corresponds to a unit volume injection, reduces to

$$p(0,t) = \frac{1}{4\pi\kappa t} \quad \text{.....(5.14)}$$

It is realized that equation (5.13) is essentially the point source solution, which is characterized by a radial flow. It can be surmised that: the late-time pressure behavior after fracture closure is like that of an instantaneous source solution, whether the formation is fractured or not during the injection.

To confirm the foregoing conjecture and to grasp upon the implication of ‘large time’, the foregoing asymptotic theory is tested on three hydraulic fracturing cases with

their parameters summarized in Table 5.1. Case 1 follows the example in the study by Detournay et al. (Detournay et al. 1990). Case 2 is created by perturbing the parameters so the final treated fracture length is about twice of the length in the first case. Case 3 is based on the actual parameter used and/or estimated in a field experiment. Using the previous PKN simulator, the fracture propagation histories are calculated and displayed in Fig. 5.3. Some crucial results are listed in Table 5.2.

Table 5.1 Parameters for three hydraulic fracture treatment cases

parameters	Case 1	Case 2	Case 3
μ (MPa·s)	5.6×10^{-7}	5.6×10^{-7}	1.0×10^{-9}
n	1.0	1.0	1.0
κ(m^2/ MPa·s)	1.0×10^{-5}	5.0×10^{-6}	1.0×10^{-7}
c (m^2/s)	0.4	0.4	0.0017
C_l (m/$s^{0.5}$)	6.3×10^{-5}	4.0×10^{-5}	2.49×10^{-5}
ν	0.2	0.2	0.2
G(MPa)	1.0×10^{4}	1.0×10^{4}	8.6×10^{3}
Q_o (m^3/s)	0.008	0.011	0.00266
H (m)	10.0	10.0	15.24
t_p(s)	1000	1000	120
λ_p (MPa)	1.7	1.7	1.7

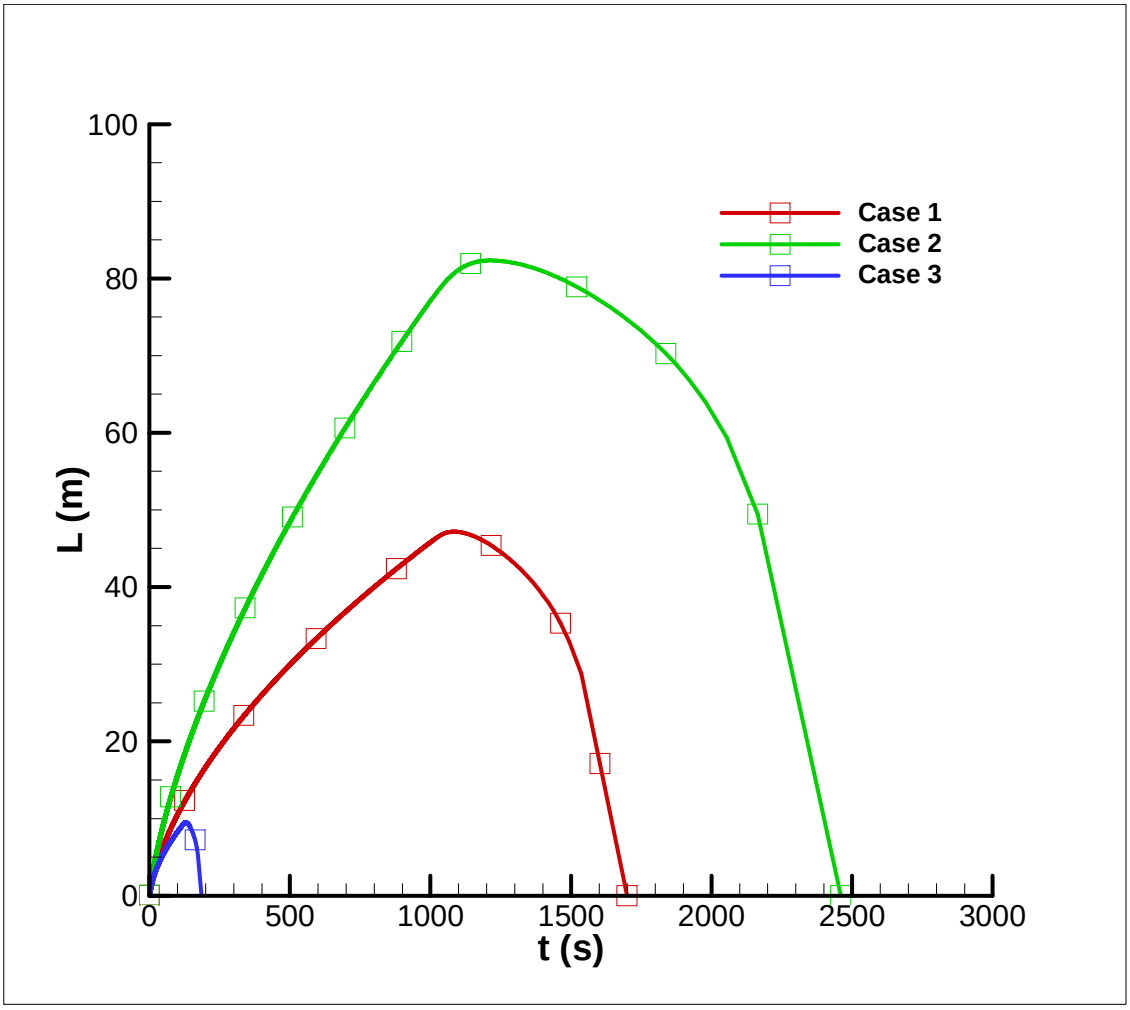

Fig. 5.3 Simulated fracture propagation histories.

Table 5.2 Summary of PKN fracture simulation

Results	Case 1	Case 2	Case 3
t_p (s)	1000	1000	120
t_c (s)	1698.95	2459.45	185.52
L_m (m)	47.18	82.33	9.52

The pressure transients in the wellbore after fracture closure for the three cases are presented respectively in the blue lines in Figs. 5.4 to 5.6 as $_p$ versus a normalized time in log-log scales. Figs. 5.4 and 5.6 are presented by normalizing Δt by fracture closure time t_c. However, since t_c is obtained from the numerical simulation, this information may not be available in field operations. In these cases, it is easier to normalize Δt by the pumping time t_p. Fig. 5.6 is normalized in this way just to demonstrate the flexibility of the theory.

In the same diagrams, we also plot the pressure derivatives taken equation (5.13) with respect of Δt

$$-\frac{dp(\Delta t)}{d\ln\Delta t} = -\Delta t\frac{dp(\Delta t)}{d\Delta t} \quad \text{.....(5.15)}$$

in green lines. The same large time characteristics are observed, since

$$-\Delta t\frac{dp(\Delta t)}{d\Delta t} = \frac{Q_o t_p}{4\pi\kappa H}\Delta t^{-1} \quad \text{.....(5.16)}$$

and the converging point of the two curves seems to mark the beginning of the -1 slope behavior.

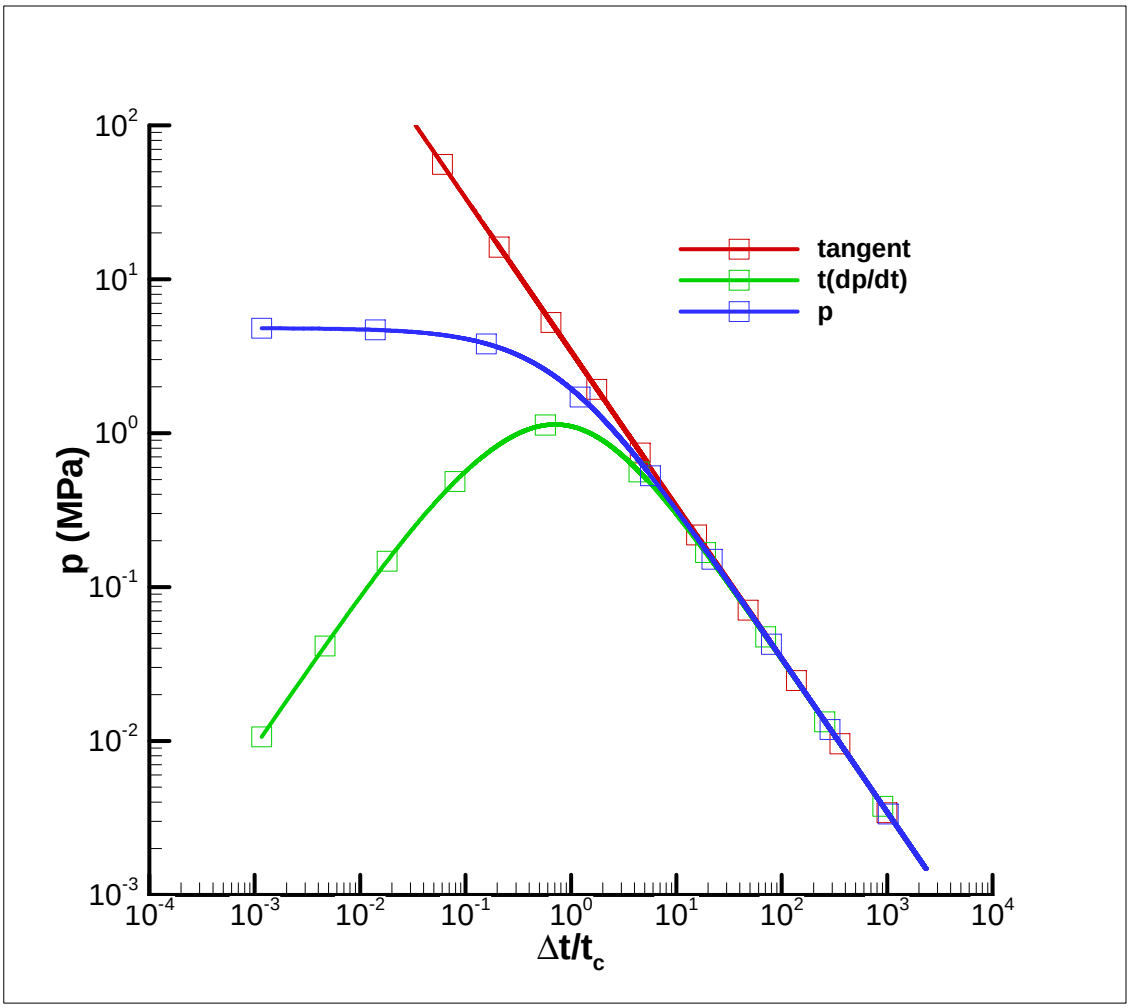

Fig. 5.4 Pressure transient for case 1, large time radial flow theory.

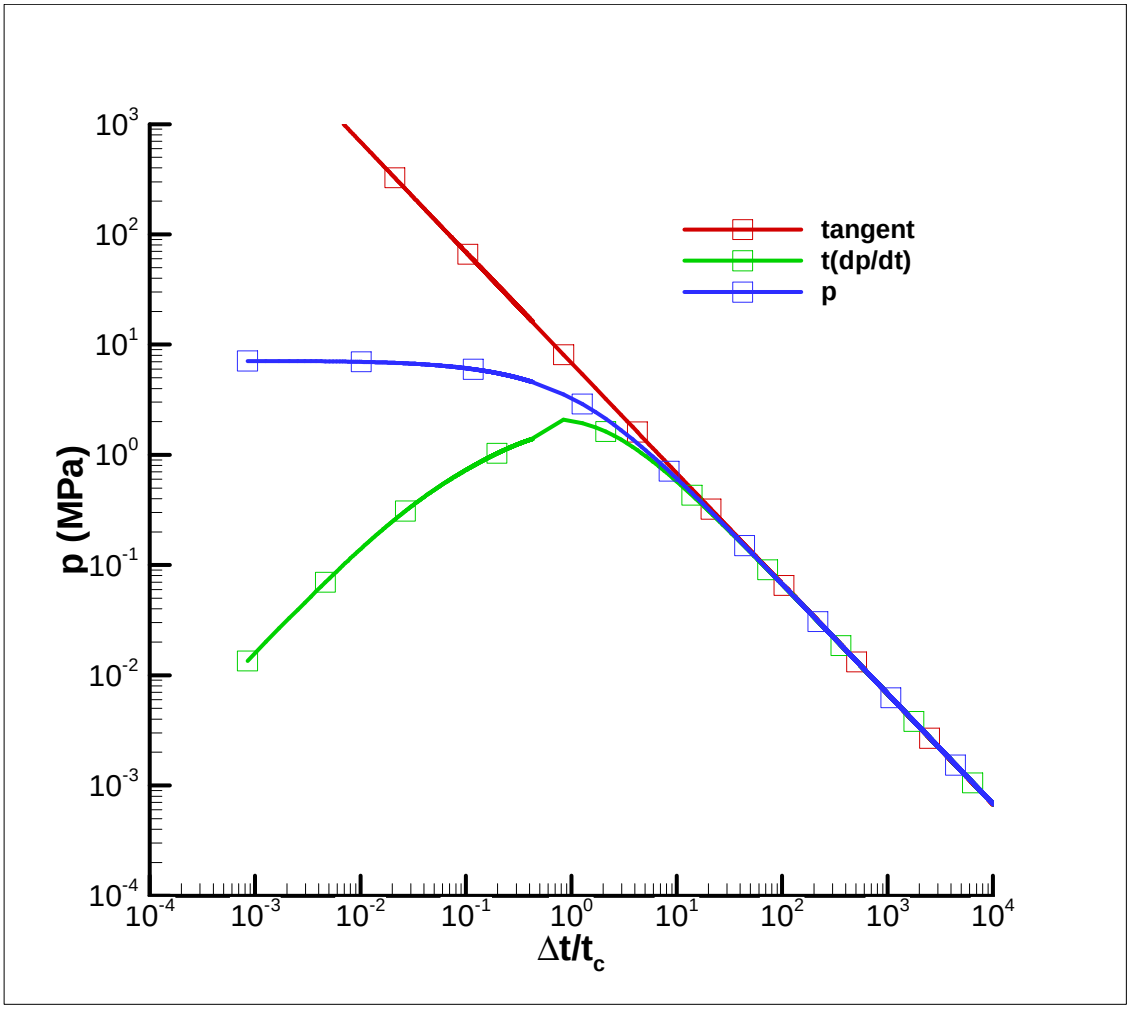

Fig. 5.5 Pressure transient for case 2, large time radial flow theory.

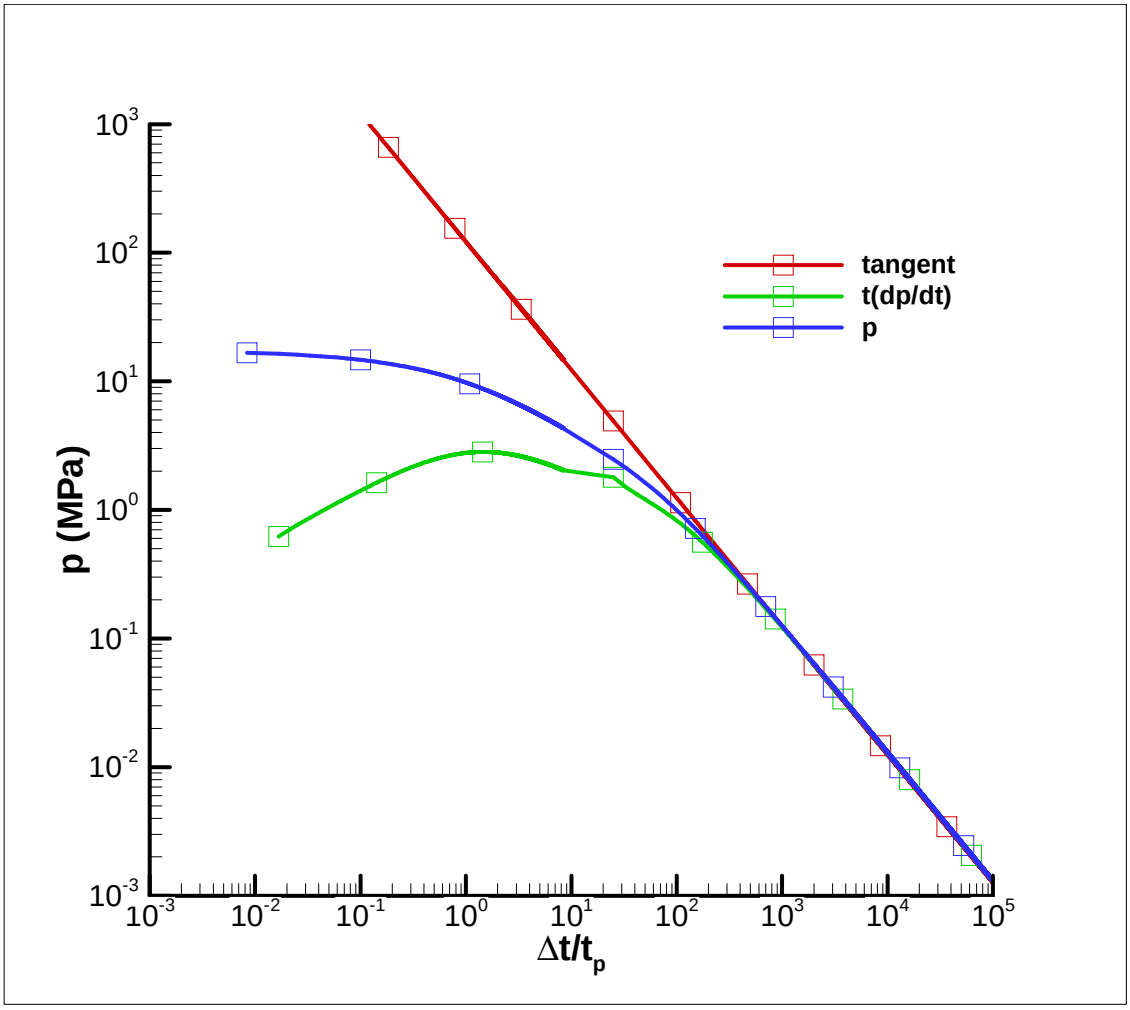

Fig. 5.6 Pressure transient for case 3, large time radial flow theory.

In Figs. 5.4 to 5.6, the -1 slope is observed around $\Delta t / t_c = 10$ for cases 1 and 2, whereas a much larger around $\Delta t / t_p = 120$ time is needed for case 3. Furthermore, if we extend the straight line backward to intersect the $\Delta t / t_c = 1$ or the $\Delta t / t_p = 1$ axis, and read the pressure intercept p_i ($p_i = 3.6$, 7.5 and 125 MPa are, respectively, read in these cases), the mobility coefficient can be estimated for cases 1 and 2 as follows:

$$\kappa = \frac{Q_o t_p}{4\pi H p_i t_c} \quad \text{.....(5.17)}$$

and for case 3

$$\kappa = \frac{Q_o}{4\pi H p_i} \quad \text{.....(5.18)}$$

Based on the values in Tables 5.1 and 5.2, we calculated the mobility κ as $1.04\times10^{-5}, 4.75\times10^{-6}$, and 1.1×10^{-7} m^2/ MPa·s, respectively for the three cases. Then we get the estimated permeability through function $k = \kappa / \mu$. These mobility values are compared with the input 'true' values$1.0\times10^{-5}, 5.0\times10^{-6}$, and$1.0\times10^{-7}$ m^2/ MPa·s. A good agreement between them is observed.

5.3.2 Horner Plot

Horner published his work on permeability estimates from pressure data buildup analysis in 1951 (Horner 1951). Similar type of work was available to ground-water hydrologists earlier, known as the recovery test (Theis 1935; Todd 1980). In the recovery test, a well is injected or produced at a constant rate for a time t_p, and then the pump is shut off. The Horner plot, is the plot of the pressure decline (or buildup) versus the logarithm of 'Horner time', which is a time function used to specifically analyze buildup test data. Horner time is defined as the special case of superposition (radial) time, for a single and constant rate flow period followed by a shut-in (i.e. a buildup), $t_H = (t_p + \Delta t)/\Delta t$.

In this model, it is expected that the finite injection interval effect will still be felt at a somewhat intermediate time, which leads to a Horner-type theory. As an approximation, it is assumed that the total fluid volume used in the treatment, $Q_o t_p$, is evenly injected during the period t_c over the thickness H in the form of a radial flow pattern (point source). For continuous injection intensity $Q_o t_p / H t_c$, the pressure influence function is (Carslaw and Jaeger 1956)

$$p(r,t) = \frac{Q_o t_p}{4\pi\kappa H t_c} E_1\left(\frac{r^2}{4ct}\right) \quad \text{.....(5.19)}$$

where $E_1(x)$ is the exponential integral (Abramowitz and Stegun 1972).

For injection lasting for the duration t_c and then shut off, the post-fracture pressure at $t > t_c$ is

$$p(r,\Delta t) = \frac{Q_o t_p}{4\pi\kappa H t_c}\left\{E_1\left[\frac{r^2}{4c(t_c+\Delta t)}\right] - E_1\left[\frac{r^2}{4c\Delta t}\right]\right\} \quad \text{.....(5.20)}$$

For small arguments (large time), the exponential integral has a logarithmic behavior as expressed as:

$$E_1(\xi) = -\ln\xi - \gamma + \xi + \cdots \quad \text{.....(5.21)}$$

where $\gamma = 0.57722$ is Euler's constant. By taking the first two terms in (5.21) and substituting into equation (5.20), the large time post-fracture pressure at the wellbore ($r = 0$) is expressed as:

$$p(\Delta t) \approx \frac{Q_o t_p}{4\pi\kappa H t_c} \ln\frac{t_c + \Delta t}{\Delta t} \quad \text{.....(5.22)}$$

The foregoing asymptotic expression suggests that if the pressure is plotted against the Horner time $t_H = (t_c + \Delta t)/\Delta t$ ($t_H = (t_p + \Delta t)/\Delta t$ for case 3) on a semi-log plot, a straight line should appear. However, when the pressure data for three cases are plotted in Figs. 5.7 to 5.9, the straight lines almost could not be observed.

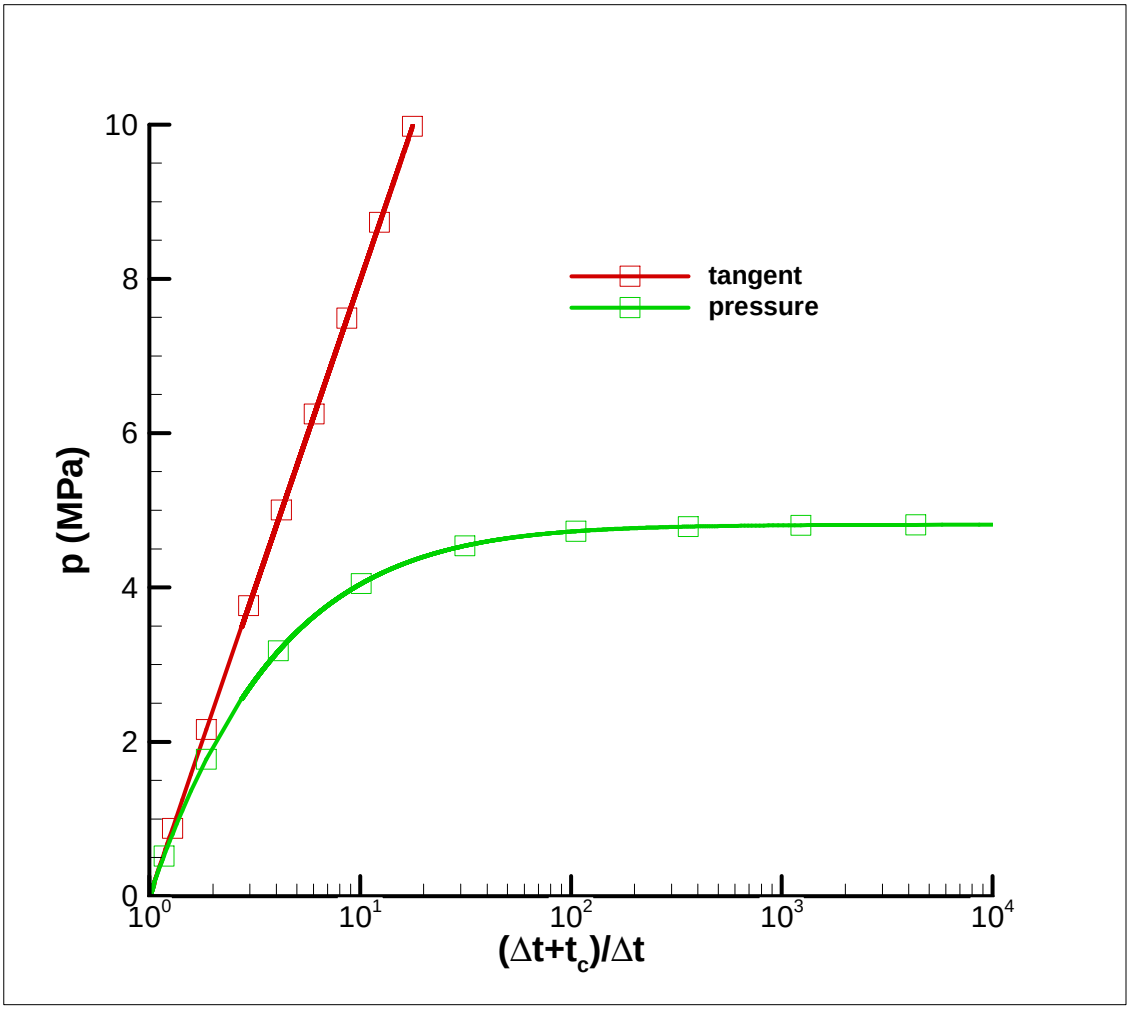

Fig. 5.7 The Horner plot for case 1.

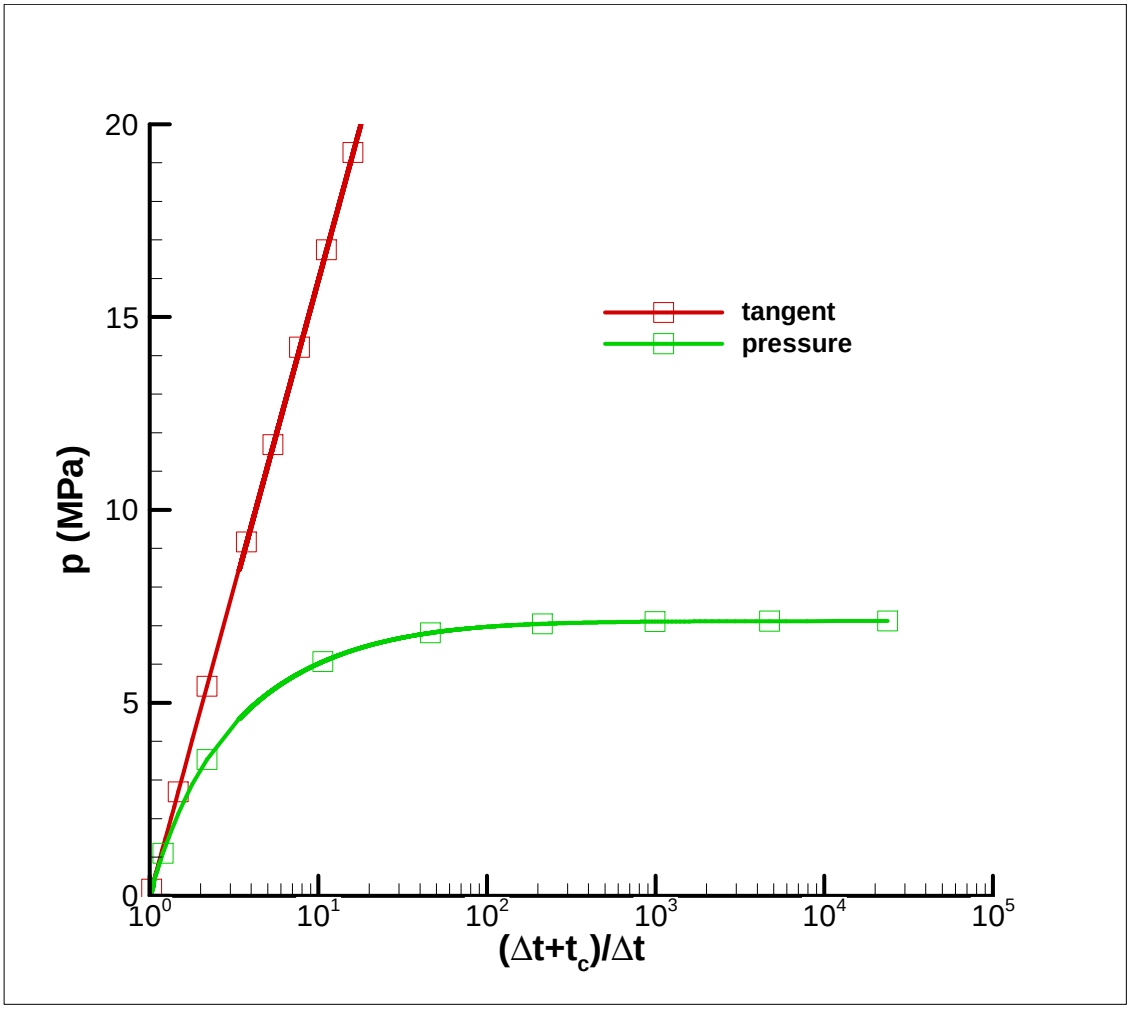

Fig. 5.8 The Horner plot for case 2.

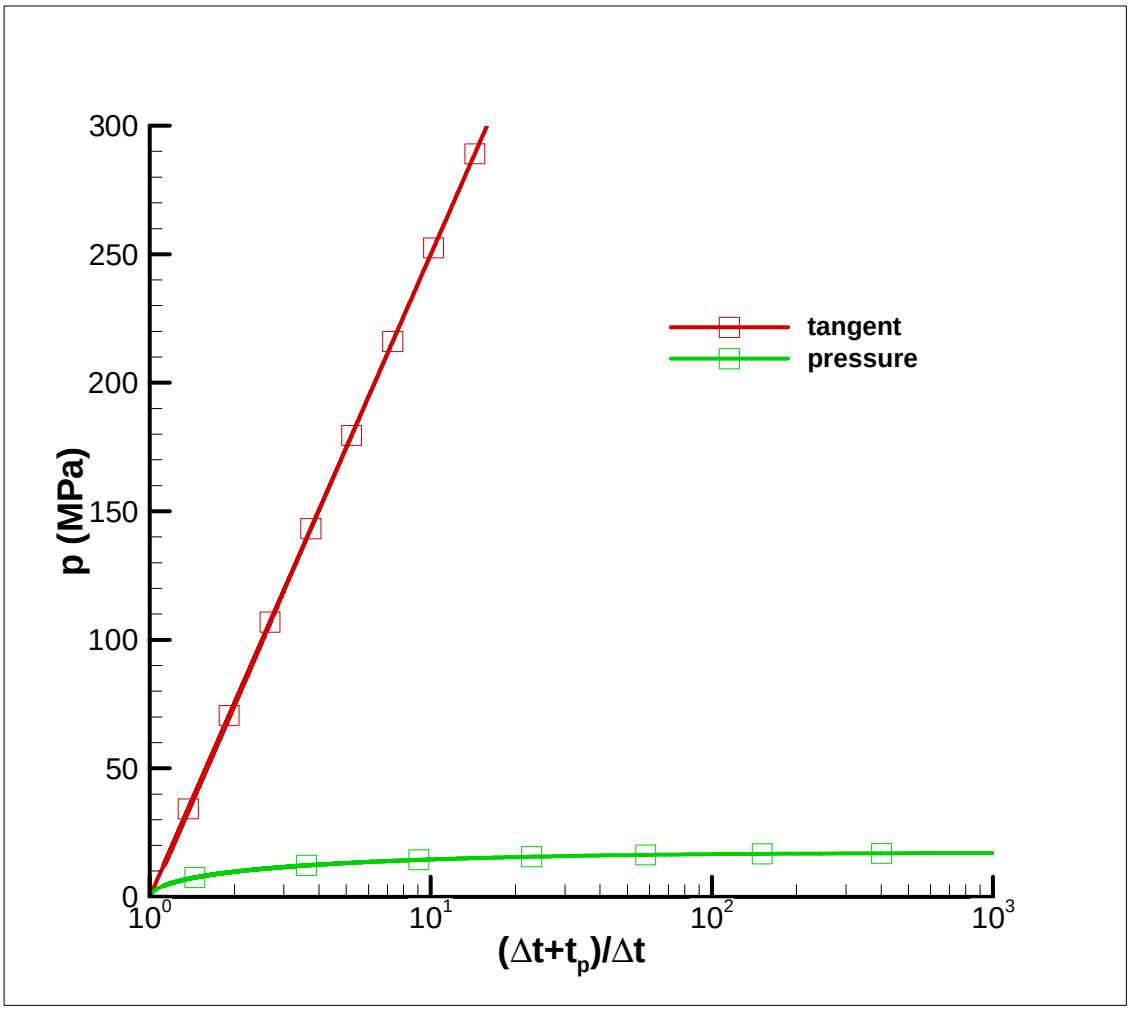

Fig. 5.9 The Horner plot for case 3.

This phenomenon can be explained as the following: since the original injection pattern is linear fracture, it may take a few folds of t_c (the equivalent injection period) for the radial flow to manifest. If it is assumed that the radial flow pattern is established at $\Delta t > 5t_c$ ($\Delta t > 5t_p$ for case 3), with the corresponding Horner time $t_H < 1.2$, the entire 'large time range', which is supposed to exhibit a straight line behavior, is bounded

between $1.0 < t_H < 1.2$. The straight line behavior is invisible under this scale in Figs. 5.7 to 5.9. Therefore, the Horner plot is inefficient to analyze the large time post-fracture pressure transient data.

However, if the inefficiency can be somewhat tolerated, a tangent line of the curve can be draw at $t_H = 1.0$. Reading the pressure intercept at $t_H = 10$ p_i ($p_i = 8.0$, 16.15 and 250.0 MPa respectively for the three cases), the mobility κ can be expressed as

$$\kappa = \frac{(\ln 10) Q_0 t_p}{4\pi H p_i t_c} \quad \text{.....(5.23)}$$

Using this equation, we can back calculate κ as 1.08×10^{-5} m^2/ MPa·s for case 1 (1.0×10^{-5} m^2/ MPa·s), 5.08×10^{-6} m^2/ MPa·s for case 2 (5.0×10^{-6} m^2/ MPa·s), and 0.83×10^{-7} m^2/ MPa·s for case 2 (1.0×10^{-7} m^2/ MPa·s). These comparisons are satisfied.

5.4 Linear Fracture Theory

As observed in the preceding section, the radial flow regime takes quite a relative long time to develop for injections taking place in the form of hydraulic fracturing. As a consequence, it is more reasonable to approximate the flow as a linear fracture pattern. Excellent work about the linear fracture flow regime has been done to identify the flow regimes and to estimate reservoir parameters using type curve matching techniques (Cinco-Ley et al. 1989; Neal and Mian 1989). In these models, the fracture conductivity is an added complexity as people try to estimate the formation permeability. The art of matching a family of type curves might be quite tricky when a semi-empirical estimation

of the fracture conductivity is needed. This inconvenience is resulted from a finite conductivity fracture in which proppant agents are entrapped to create pathway for fluid after fracture closure.

In the impulse fracture test, a fracture is created using fluid without proppant agent. When the fracture closes, the cakes built on the fracture surfaces are compressed to fill the gap between the fracture walls. Therefore the fracture is considered with zero conductivity. Under this assumption, several asymptotic theories are developed in the following sections.

5.4.1 Instantaneous Line Source Theory

To study the source geometry effect in earlier times, it is assumed that the injection occurs as an instantaneous line source with a uniform intensity and an 'equivalent length' L_e. This equivalent length generally does not coincide with the actual fracture maximum length L_m, but it can serve as the first-order estimation of L_m.

The influence function of a line source located at $-L \le x \le L$ and $y = 0$ with unit intensity is given by (Carslaw and Jaeger 1956).

$$p(x,y,t) = \frac{1}{4\pi\kappa t}\int_{-L}^{L} e^{-[(x-x')^2+y^2]/4ct}dx' \quad \text{.....(5.24)}$$

If the observation point is at the origin $x = y = 0$, the pressure expression is simplified as:

$$p(0,0,t) = \frac{1}{2\kappa}\sqrt{\frac{c}{\pi t}}erf\left(\frac{L}{\sqrt{4ct}}\right) \quad \text{.....(5.25)}$$

where *erf* is the error function. Taking the total injection volume into consideration, the pressure at wellbore for the current problem is

$$p(\Delta t)=\frac{Q_0 t_p}{4\kappa H L_e}\sqrt{\frac{c}{\pi\Delta t}}erf\left(\frac{L_e}{\sqrt{4c\Delta t}}\right) \quad \text{.....(5.26)}$$

For small argument (large time), the error function can be expanded as

$$erf(\xi)=\frac{2}{\sqrt{\pi}}\left(\xi-\frac{\xi^3}{3}+\cdots\right) \quad \text{.....(5.27)}$$

By keeping the first two terms in formula (5.27), we obtain from (5.26) the following equation:

$$p(\Delta t)\approx\frac{Q_o t_p}{4\pi\kappa H}\left(1-\frac{L_e^2}{12c\Delta t}\right)\Delta t^{-1} \quad \text{.....(5.28)}$$

The difference between the instantaneous point source solution (5.13) and the current line source solution (5.28) is

$$\Delta p(\Delta t)\approx\frac{Q_o t_p L_e^2}{48\pi\kappa H c}\Delta t^{-2} \quad \text{.....(5.29)}$$

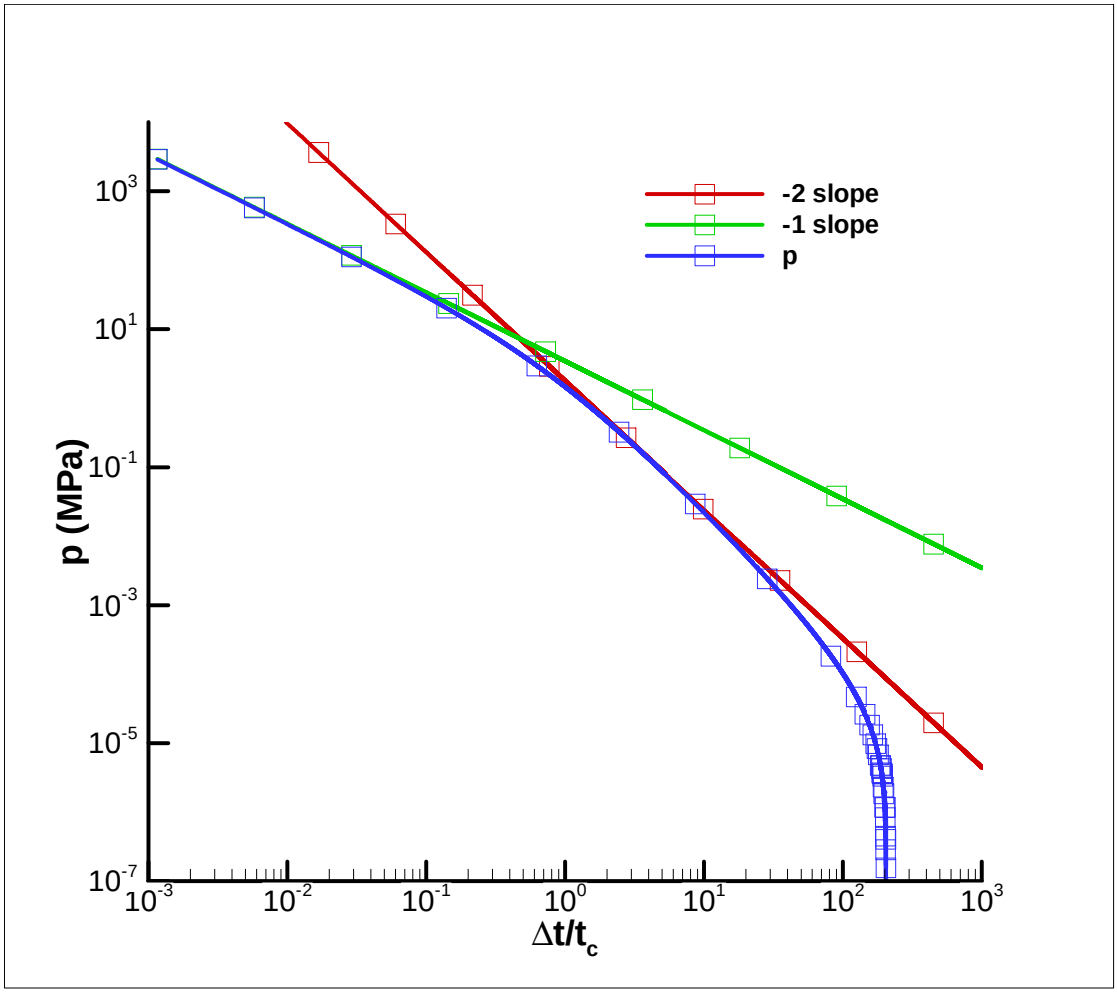

Fig. 5.10 The instantaneous line source for case 1.

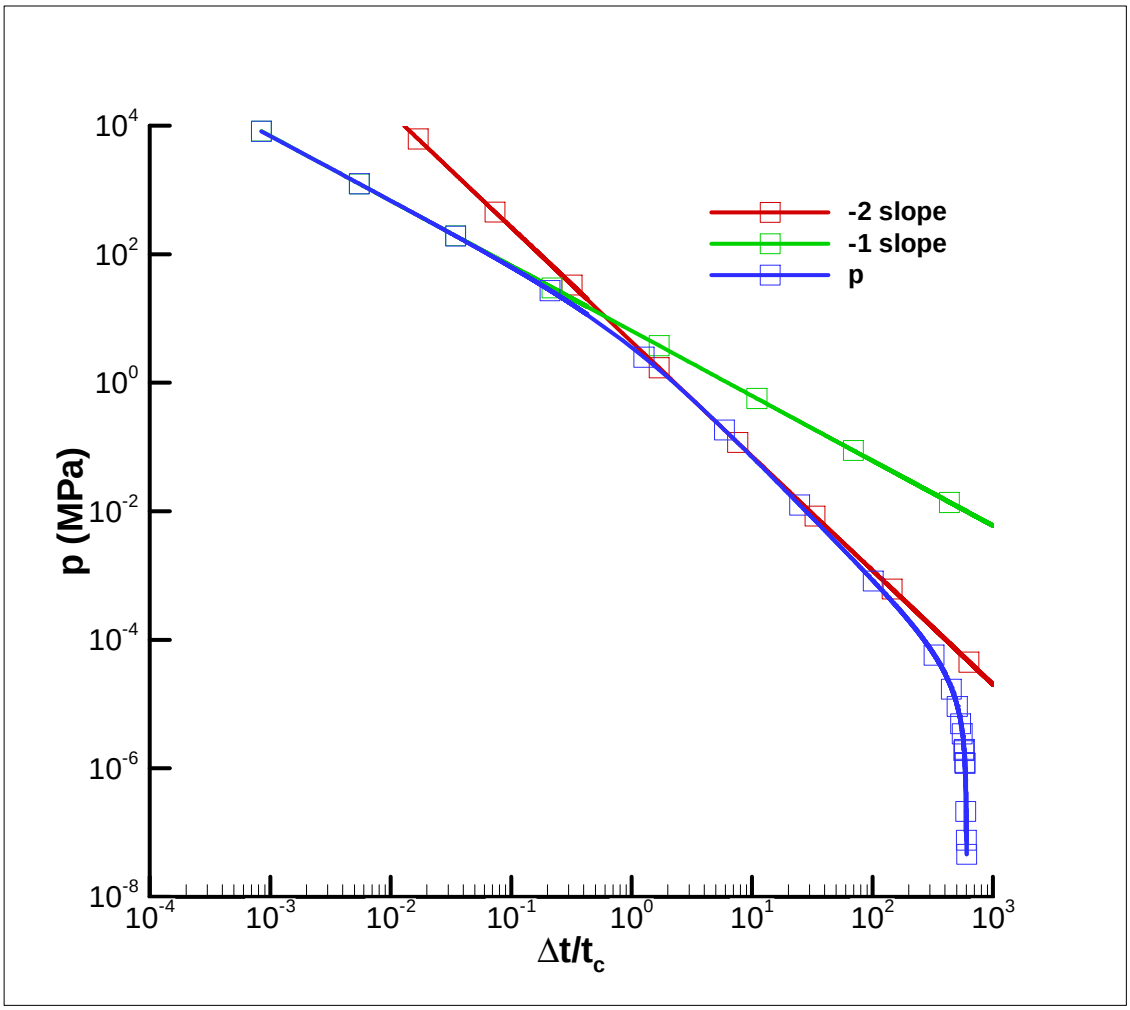

Fig. 5.11 The instantaneous line source for case 2.

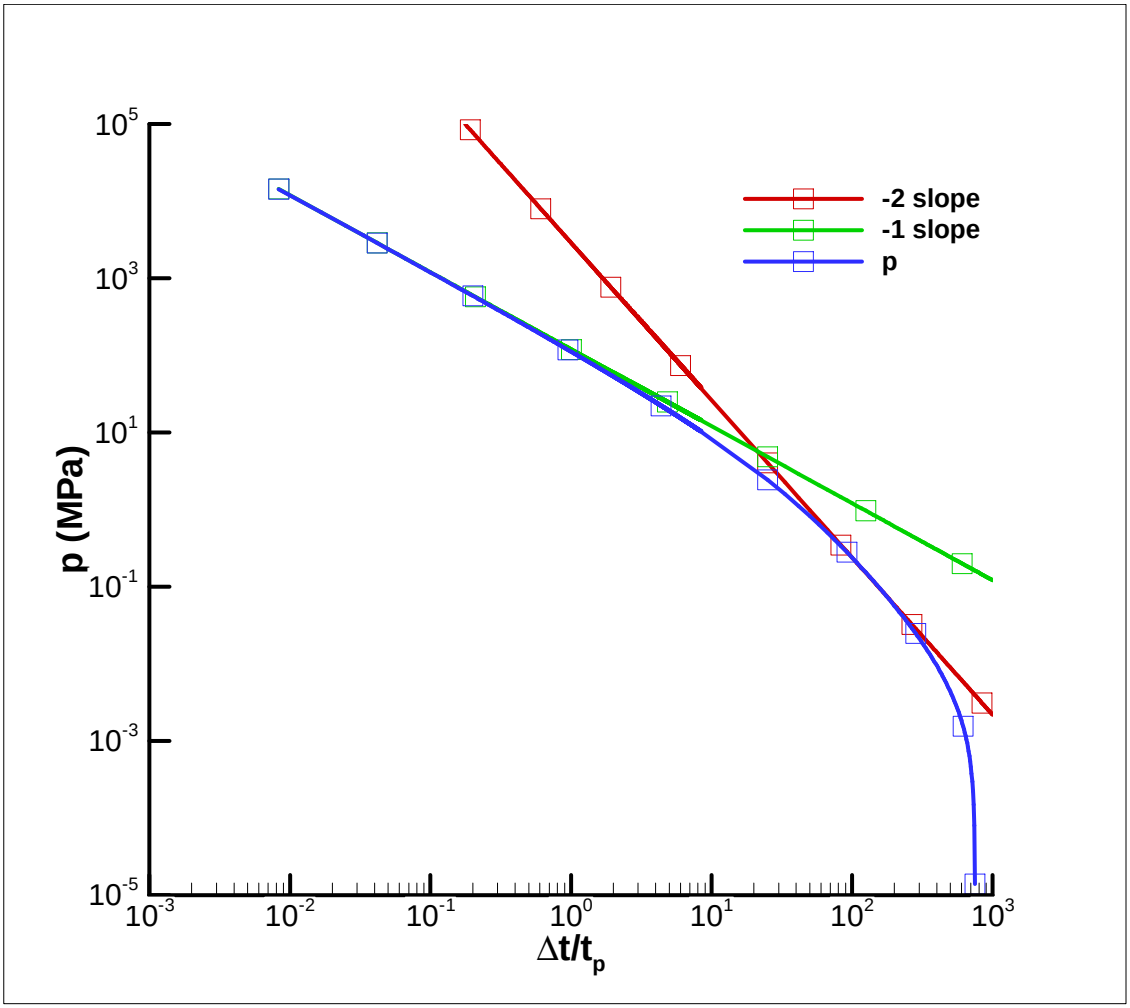

Fig. 5.12 The instantaneous line source for case 3.

The equation above suggests that if we find the differences between the -1 slope straight line and the actual pressure record in Figs. 5.4, 5.5 and 5.6, and show them in log-log plots, a -2 slope straight line should be observed when the linear fracture geometry is still dominant at an intermediate time. These plots are presented in Figs. 5.10, 5.11, and 5.12. There are -1 slope straight lines right after fracture closure. Since

the pressure for equivalent radial flow is thousands of times larger than the actual pressure records in Figs. 5.4, 5.5 and 5.6 at small time, this -1 slope lines in Figs. 5.10, 5.11 and 5.12 represent the equivalent radial flow in early times. The -2 slope lines stand for the linear fracture flow before it changes to radial flow. Extending the -2 slope straight line to find the pressure intercept p_i with the $\Delta t / t_c = 1$ axis ($p_i = 1.3,\ 5.0$ MPa) for cases 1 and 2, and the estimation of the following quantity is:

$$\frac{\kappa c}{L_e^2} = \frac{Q_o t_p}{48\pi H p_i t_c^2} \qquad \text{.....(5.30)}$$

For case 3, which uses t_p to normalize, the formula is slightly changed as

$$\frac{\kappa c}{L_e^2} = \frac{Q_o}{48\pi H p_i t_p} \qquad \text{.....(5.31)}$$

and the -2 slope straight line pressure intercept p_i is 5000 MPa at $\Delta t / t_p = 1$. The foregoing equations can be used in several ways. Firstly, with known diffusivity coefficient c and fracture length L_m, κ can be estimated; and secondly, with a known κ and c, an equivalent fracture length L_e can be evaluated.

In the present cases, substitute the known c and κ values, respectively, to calculate the equivalent lengths $L_e = 53.2$m, 91.1m, and 9.4 m. The maximum lengths as simulated from the previous PKN model are 47.18m, 82.33m, and 9.52m (Table 5.2). The predictions are quite reasonable considering that they are the first-order approximation.

5.4.2 Finite Interval Line Source Theory

The analysis in this section is similar to the recovery test conducted for Horner's plot, assuming that this theory is applicable to some intermediate time intervals. The pressure influence function for a continuous line source at the wellbore is (Gringarten and Ramey 1974).

$$p(0,0,t)=\frac{Q_o t_p}{4\pi\kappa H t_c}[E_1(\frac{L_e^2}{4ct})+\frac{\sqrt{4\pi ct}}{L_e}erf(\frac{L_e}{\sqrt{4ct}})] \quad \text{.....(5.32)}$$

For a finite interval injection with time duration t_c, the corresponding pressure expression is

$$p(\Delta t)=\frac{Q_o t_p}{4\pi\kappa H t_c}\left\{E_1\left[\frac{L_e^2}{4c(t_c+\Delta t)}\right]-E_1\left[\frac{L_e^2}{4c\Delta t}\right]+\frac{\sqrt{4\pi c(t_c+\Delta t)}}{L_e}erf\left[\frac{L_e}{\sqrt{4c(t_c+\Delta t)}}\right]-\frac{\sqrt{4\pi c\Delta t}}{L_e}erf\left[\frac{L_e}{\sqrt{4c\Delta t}}\right]\right\} \quad \text{.....(5.33)}$$

Expanding the foregoing expression for large Δt by keeping the first three terms in (5.21) and first two terms in (5.27), we find the approximation

$$p(\Delta t)=\frac{Q_o t_p}{4\pi\kappa H t_c}\left[\ln\frac{t_c+\Delta t}{\Delta t}+\frac{L_e^2}{12c(t_c+\Delta t)}-\frac{L_e^2}{12c\Delta t}\right] \quad \text{.....(5.34)}$$

Once again looking for the difference between the finite interval line source solutions (5.34) and the point source solution (5.22), we obtain

$$\Delta p(\Delta t)=\frac{Q_o L_e^2 t_p}{48\pi\kappa H c t_c^2}(\frac{t_c}{\Delta t}-\frac{t_c}{t_c+\Delta t}) \quad \text{.....(5.35)}$$

Plotting the pressure difference between the tangent fit and the actual pressure record in the Horner plot (Figs. 5.7, 5.8, 5.9), versus the dimensionless time

$t_h = t_c/\Delta t - t_c/t_c + \Delta t$ for case 1 and 2 on log-log scale ($t_h = t_p/\Delta t - t_p/t_p + \Delta t$ for case 3), we should expect a +1 slope line at some intermediate time (see Figs. 5.13 to 5.15). Checking the intercept p_i($p_i = 0.98$, 4.0, 3000 MPa respectively for the three cases) at $t_h = 1$, we are able to utilize the formula 5.29 for case 1 and 2, and 5.30 for case 3 to estimate the equivalent lengths.

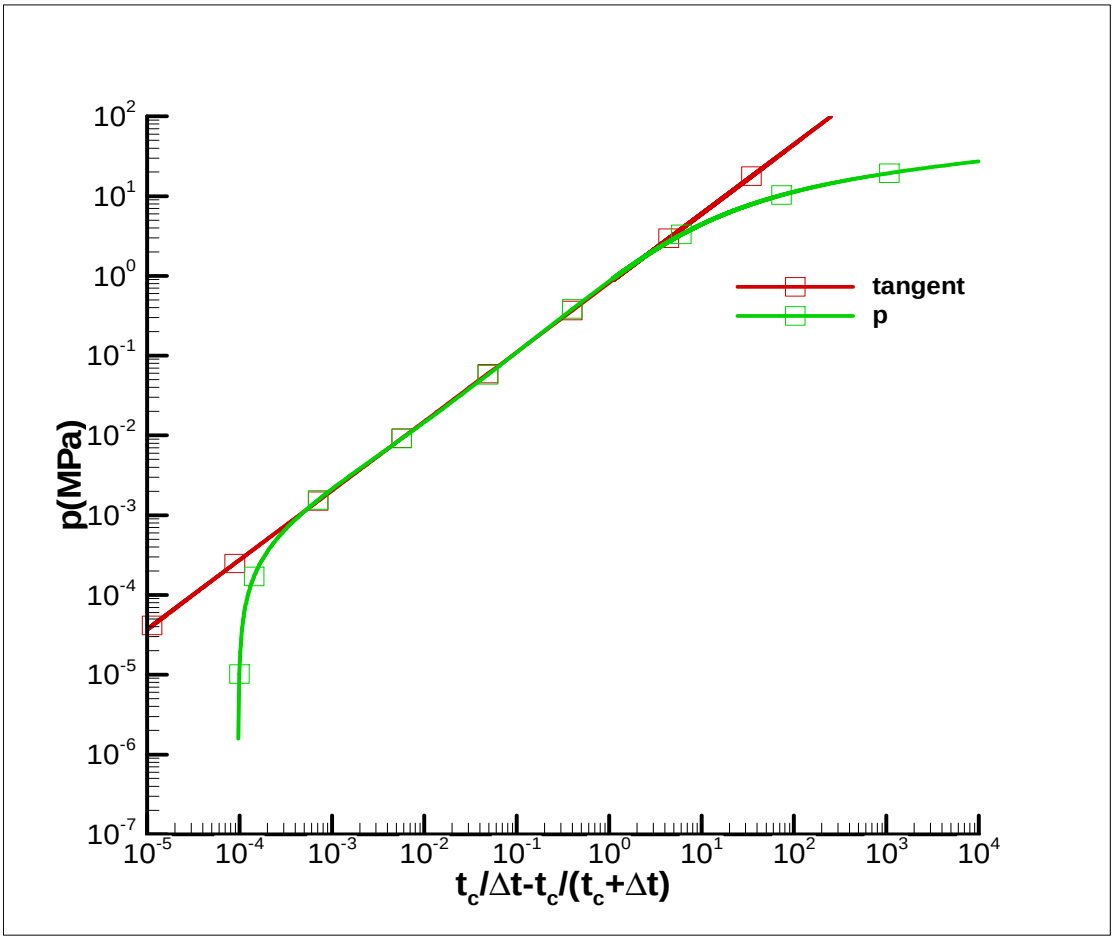

Fig. 5.13 The line source Horner plot for case 1.

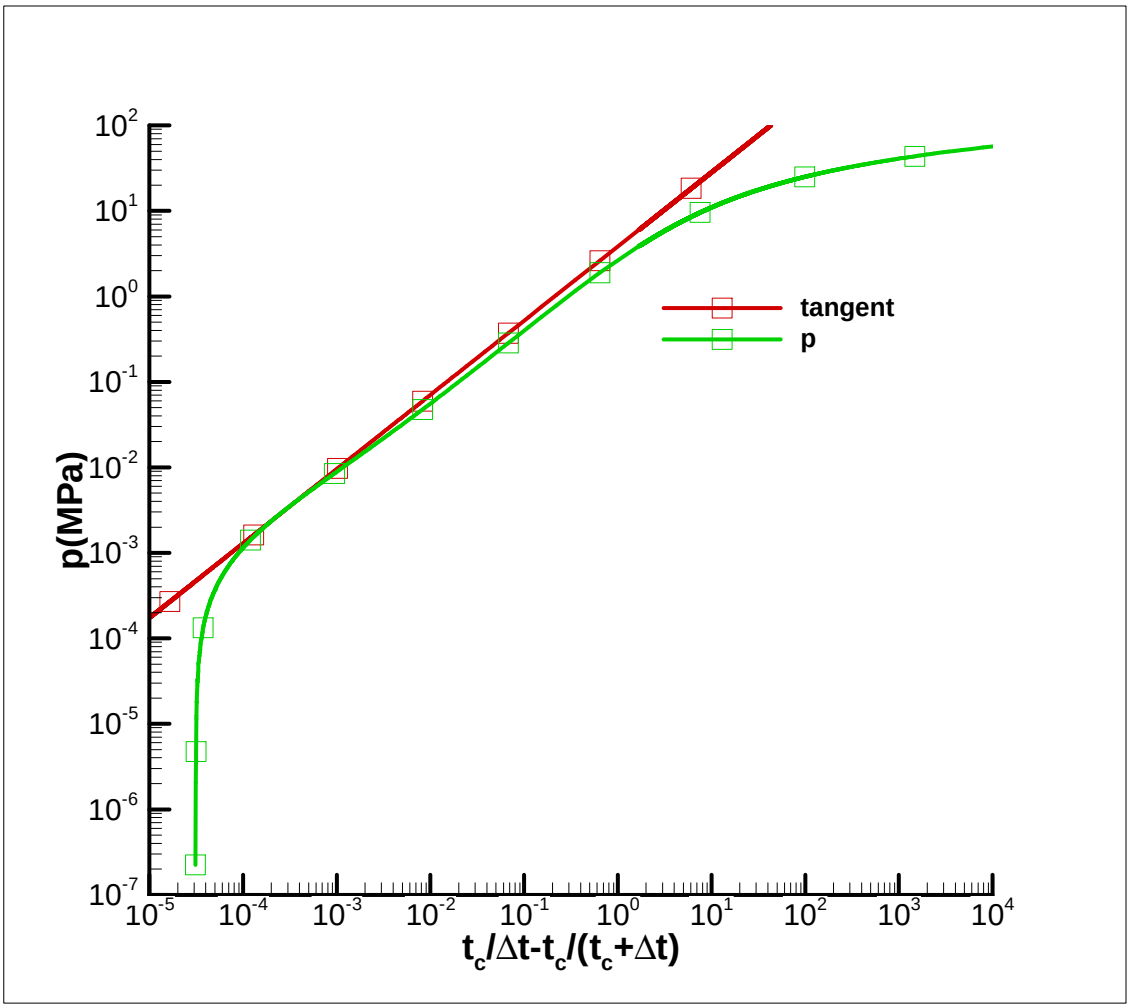

Fig. 5.14 The line source Horner plot for case 2.

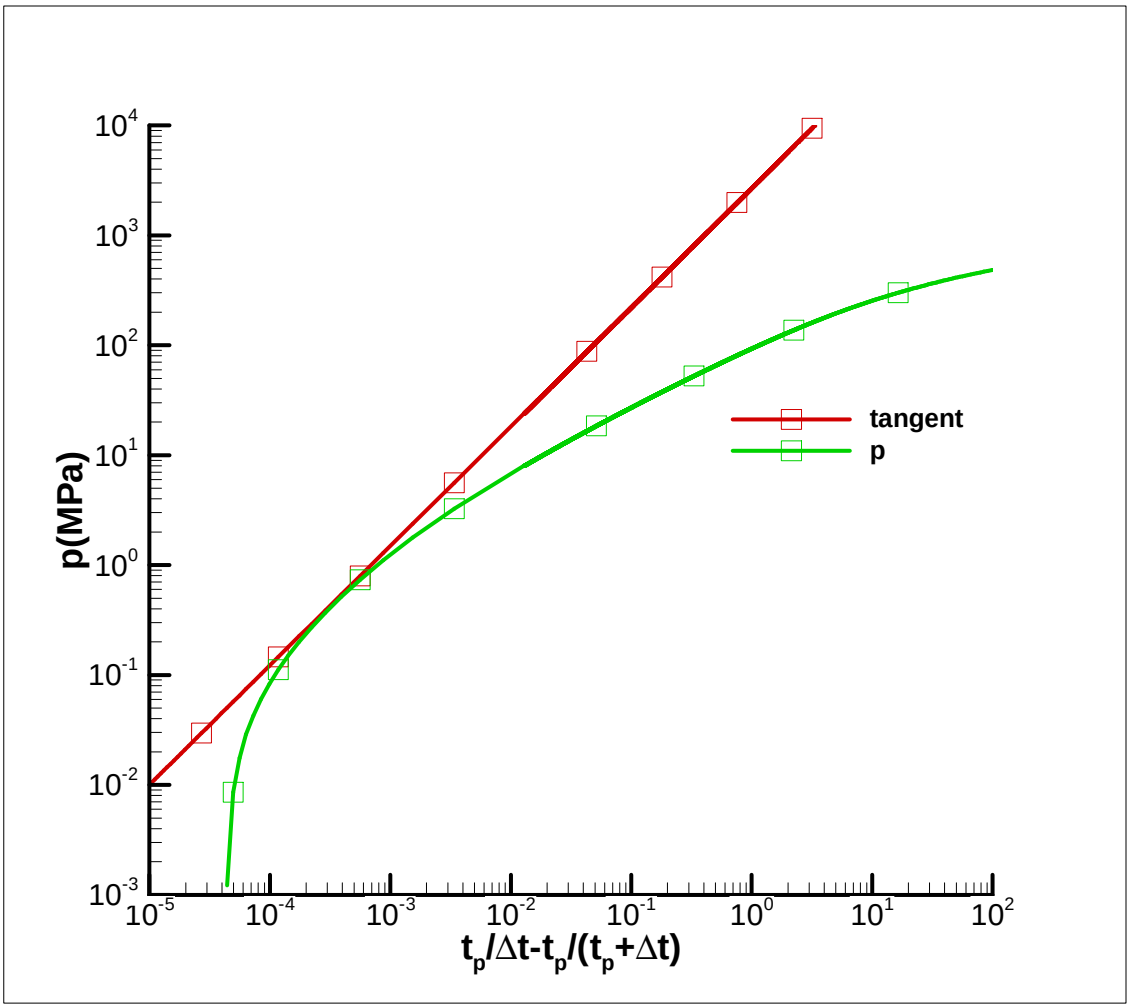

Fig. 5.15 The line source Horner plot for case 3.

The equivalent lengths computed according to the foregoing formula are, respectively, 46.2 m, 81.5 m, and 7.4 m for cases 1 to 3, which also compare very well with the simulated maximum lengths in Table 5.2.

5.5 Conclusion

In this section, we present the theory and analysis of post-fracture pressure transient test. The important things to conclude are:

1) A program based on a theory of distribution of sources along the fracture with varying intensity for PKN fracture geometry is developed. It numerically simulates the pressure decline behavior in the wellbore after fracture closure.
2) Several asymptotic theories were use from which the type curve technique can be used to estimate the formation permeability (in section 5.3) and fracture equivalent length (in section 5.4).
3) It confirmed the type curve theories based on numerically simulated data.

6. CONCLUSIONS

In the present study, several important stages of hydraulic fracturing are discussed using the poroelastic PKN fracture model as described in the literature. Firstly hydraulic fracturing propagation, recession, and pressure changing history are simulated with two different approaches to fluid leak-off theory. And then the sensitivity of fracture geometry and pressure to fluid and formation properties is analyzed. Thirdly, based on previous simulator, the post-fracture pressure-transient analysis is carried out to determine the formation permeability.

6.1 Summary

In Section 2, an existing PKN fracture model (Detournay et al. 1990) is modified. The major points in this part of research are:

1) The Carter's leak-off theory with a constant fluid leak-off coefficient is adopted.
2) Both elastic and poroelastic formation effects are included, and poroelaticity causes significant increase in fracturing pressure.

In Section 3, the PKN fracture model was simulated by applying a pressure-dependent leak-off rate. The following have been addressed:

1) The influence of poroelaticity on fracture geometry and pressure is greater than it is in previous model. The poroelaticity causes a smaller fracture volume with smaller maximum fracture length and width.

2) The pressure-dependent leak-off model leads to fast fluid loss into the formation during injection; it lowers the fluid leak-off rate after shut-in, thus it takes a longer time before the fracture closes.

In Section 4, the effects of fluid viscosity, shear modulus of rock, and the fluid leak-off coefficient on fracture geometry and pressure are discussed and the following arguments can be made:

1) A wider and shorter fracture will be produced with higher fluid viscosity and a narrower and longer fracture will be produced with lower fluid viscosity with all other conditions unchanged.
2) A shorter and wider fracture will be generated when the formation is soft with low shear modulus, while a longer and narrower fracture will be produced when the formation is hard with high shear modulus with all other conditions unchanged.
3) The fracture length, width, fracturing pressure, and the fracture closure time increase with decreasing of the leak-off coefficient.

In Section 5, the post-fracture pressure-transient analysis is conducted to determine the formation permeability, using the type-curve-analysis of the asymptotic behavior during intermediate and large times. The results show a good agreement with published results, which enhanced the validity of both studies (Abousleiman et al. 1994).

6.2 Future Work

This study addressed certain questions and problems in hydraulic fracturing modeling. However, this technique is far from perfect and more questions need to be answered to improve future models. Based on this study, the following aspects could be significant questions in hydraulic fracture modeling for future study:

1) To apply the model developed in this study to simulate fracture network generation.
2) Taking formation temperature change into consideration in future modeling.
3) Analyzing small time pressure behavior in the post-fracture pressure-transient test to determine the formation permeability. (We just discussed the intermediate and large time solution in Section 5).

REFERENCES

Abé, H., Mura, T., and Keer, L. 1976. Growth-rate of a Penny-shaped Crack in Hydraulic Fracturing of Rocks. *J. Geophys. Res.* **81** (35).

Abousleiman, Y.N. 1991. A Poroelastic PKN Model with Pressure Dependent Leakoff and Formation Permeability Determination, PhD dissertation, University of Delaware.

Abousleiman, Y.N., Cheng, A.H.-D., and Gu, H. 1994. Formation Permeability Determination by Micro or Mini-Hydraulic Fracturing. *J. Energy Res. Tech .Trans. ASME* **116**: 104-114.

Abramowitz, M. and Stegun, I. 1972. *Handbook of Mathematical Functions*. Dover, New York.

Agarwal, R.G., Al-Hussainy, R., and Ramey, H.J.J. 1974. An Investigation of Wellbore Storage and Skin Effect in Unsteady Liquid Flow: I. Analytical Treatment. *SPE J. Trans. AIME* **249**: 279-290.

Biot, M.A. 1941. General Theory of Three-dimensional Consolidation. *Journal of Applied Physics* **12**: 155-164.

Boone, T.J. and Detournay, E. 1990. Response of a Vertical Hydraulic Fracture Intersecting a Poroelastic Formation Bounded by Semi-I nfinite Impermeable Elastic Layers. *Int. J. Rock Mech. Mining Sci. & Geomech. Abstr.* **27**: 189-197.

Carslaw, H. and Jaeger, J.C. 1956. *Conduction of Heat in Solids,* 2nd edition. Oxford, UK: Oxford University Press.

Carter, R.D. 1957. Derivation of the General Equation for Estimating the Extent of the Fractured Area. *In Drill. and Prod. Prac. API,* ed. Howard, G.C. and Fast,C.R., 261-268. New York.

Cinco-Ley, H., Samaniego-V, F., and Rodriguez, F. 1989. Application of the Pseudolinear-Flow Model to the Pressure-Transient Analysis of Fractured Well. *SPE Formation Evaluatin* **4** (3): 438-444.

Cleary, M.P. 1980. Comprehensive Design Dormulae for Hydraulic Fracturing. Paper SPE 9259 presented at 55th Annual Fall Technical Conference and Exhibition, Dallas, TX, 21-24 September.

Courant, R., Isaacson, E., and Rees, M. 1952. On the Solution of Nonlinear Hyperbolic Differential Equations by Finite Differences. *Comm. Pure Appl. Math.* **5**: 243-255.

Detournay, E. and Cheng, A. H. D. 1991. Plane Strain Analysis of a Stationary Hydraulic Fracture in a Poroelastic Medium. *Int. J. Solids Structures* **27**: 1645-1662.

Detournay, E., Cheng, A. H. D., and Mclennan, J.D. 1990. A Poroelastic PKN Hydraulic Fracture Model Based on an Explicit Moving Mesh Algorithm. *J. Energy Res. Tech.Trans. ASME* **112** (4): 7.

Detournay, E. and Cheng, A. H. D. 1993. Fundamentals of Poroelasticity. In *Comprehensive Rock Engineering: Principles, Practice and Project*, ed. Fairhurst, C., Analysis and Design Method: Pergamon Press. II.

Economides, M. and Nolte, K.G. 2000. *Reservoir Stimulation,* 3rd edition, New York: John Wiley & Sons, Ltd.

Economides, M.J. and Nolte, K.G. 1989. *Reservoir Stimulation,* 2nd edition, Houston, TX: Prentice Hall.

Geertsma, J. 1957. The Effect of Fluid Pressure Decline on the Volumetric Changes of Porous Rocks. *Journal of Applied Mechanics* **24**: 594-601.

Geertsma, J. and Klerk, F.d. 1969. A Rapid Method of Predicting Width and Extent of Hydraulically Induced Fractures. *J. Pet. Tech.* **21**: 1571-1581.

Ghassemi, A., Diek, A., and Roegiers, J. C. 1996. A Solution for Stress Distribution Around An Inclined Borehole in Shale. *Int. J. Rock Mech. Mining Sci. & Geomech. Abstr.* **35** (4): 538-540.

Griffith, A.A. 1921. The Phenomena of Rupture and Flow in Solids. *Phil. Trans. Roy. Soc.* **221**: 163-198.

Griffith, A.A. 1924. The Theory of Rupture. *Proc.* 1st International Congress on Applied Mechanics, Delft, Netherlands, 55-63.

Gringarten, A.C. and Ramey, H.J.J. 1974. Unsteady-State Pressure Distribution Created by a Well With a Single Infinite-Conductivity Vertical Fracture. *SPE J. Trans. AIME* **257**: 347-360.

Gu, H., Elbel, J.L. and Nolte, K.G. 1993. Formation Permeability Determination Using Impulse-Fracture Injection. Paper SPE 25425-MS presented at SPE Production Operations Symposium, Oklahoma City, Oklahoma, 21 March.

Horner, D.R. 1951. Pressure Buildup in Wells. *Proc.*, 3rd World Petroleum Congress, Hague, Netherlands, 28 May-6 June.

Howard, G.C. and Fast, C.R. 1957. Optimum Fluid Characteristics for Fracture Extension. *Drill. and Prod. Prac. API* 261-270.

Jun, G. 2009. Modeling and Analysis of Reservoir Response to Stimulation by Water Injection, MS thesis, Texas A&M University, College Station, TX.

Khristianovitch, S.A. and Zheltov, Y.P. 1955. Formation of Vertical Fractures by Means of Highly Viscous Fluids. *Proc.*, 4th World Petroleum Congress, Rome, **2**:579-586.

Legarth, B., Huenges, E., and Zimmermann, G. 2005. Hydraulic Fracturing in a Sedimentary Geothermal Reservoir: Results and Implications. *Int. J.Rock Mech. Mining Sci.* **42**: 1028-1041.

Morales, R.H. 1989. Microcomputer Analysis of Hydraulic Fracture Behavior with a Pseudothree Dimensional Simulator. *SPEPE* **4** (1): 69-74.

Murphy, H. 1983. Hot Dry Rock Reservoir Development and Testing in the USA. *Proc.*, First Japan-U.S. Seminar on Hydraulic Fracturing and Geothermal Energy, Tokyo, 2-5 November, 33-38.

Muskat, M. 1937. *The Flow of Homogeneous Fluids Through Porous Media*. New York: McGraw-Hill Book Company.

Neal, D.B. and Mian, M.A. 1989. Early-Time Tight Gas Production Forecasting Technique Improves Reserves and Reservoir Description. *SPE Form Eval* **4** (1): 25-32.

Nilson, R.H. and Griffiths, S.K. 1983. Numerical Analysis of Hydraulically-Driven fractures. *J. of Compt. Meth. and Appl. Mech. and Eng.* **36**: 359-370.

Nolte, K.G. 1979. Determination of Fracture Parameters From Fracturing Pressure Decline. *Proc*., 54th Annual Fall Technical Conference, Las Vegas, Nevada, 23-26 September.

Nolte, K.G. and Economides, M.J. 1989. Fracturing Diagnosis Using Pressure Analysis. In *Reservoir Stimulation*, ed. M.J.Economides and K.G.Nolte, Chap. 7, Englewood Cliffs, NJ.: Pretice Hall, Inc.

Nordgren, R.P. 1972. Propagation of a Vertical Hydraulic Fracture. *Society of Petroleum Engineering Journal* **253**: 306-314.

Nygren, A. and Ghassemi, A. 2006. Poroelastic and Thermoelastic Effects of Injection into a Geothermal Reservoir. Paper presented at The 41st U.S. Symposium on Rock Mechanics, Golden, ARMA/USRMS 06-1053.

Perkins, T.K. and Kern, L.R. 1961. Widths of Hydraulic Fractures. *J. Pet. Tech.* **13**: 937-949.

Poollen, H.K.V., Tinsley, J.M., and Saunders, C.D. 1958. Hydraulic Fracturing: Fracture Flow Capacity vs. Well Productivity. *Trans., AIME* **213**: 91-95.

Prats, M. 1961. Effect of Vertical Fractures on Reservoir Behavior-Incompressible Fluid Case. *SPE Journal* 105-118. SPE1575-G.

Press, W.H., Flannery, B.P., Teukolsky, S.A. and Vetterling, W.T. 1989. *Numerical Recipe*, New York: Cambridge University Press.

Qiang, Z. 2001. Comparison fo the PKN, KGD and Nordgren Modified PKN Model Predicting Width and Extent of Hydraulically Induced Fractures. Report for Geological Engineering Research 590, University of North Dakota, Grand Forks, ND, (unpublished).

Rice, J.R. and Cleary, M.P. 1976. Some Basic Stress-diffusion Solutions for Fluid Saturated Elastic Media with Compressible Constituents. *Rev. Geophys.***14**: 227-241.

Roegiers, J. C., Detournay, E., Cheng, A.H. D. and McLennan, J.D. 1989. Poroelastic Considerations in in situ Stress Determination by Hydraulic Fracturing. *Int. J. Rock Mech. Mining Sci. & Geomech. Abstr*. **26**: 507-513.

Schlumberger Oilfield Glossary. Schlumberger, www.glossary.oilfield.slb.com/. Downloaded 1st June 2011.

Settari, A. 1980. Simulation of Hydraulic Fracturing Processes. *SPE Journal* **20**(6): 487-500.

Settari, A. 1985. A New General Model of Fluid Loss in Hydraulic Fracturing. *SPE J.***25** (4) 491-501.

Settari, A. and Cleary, M.P. 1986. Development and Testing of a Pseudo-three-dimensional Model of Hydraulic Fracture Geometry. *SPE Prod. Eng.* **1** (6) 449-466.

Simonson, E.R., Abou-Sayed, A.S., and Clifton, R.J. 1978. Containment of Massive Hydraulic Fractures. *Soc. Pet. Engrs. J.* **18**: 27-32.

Soliman, M.Y. 1986. Analysis of Buildup Tests With Short Producing Time. *SPE Form. Eval.* **1** (4) 363-371.

Theis, C. V. 1935. The Relations Between the Lowering of the Piezometric Surface and the Duration of Discharge of a Well Using Ground-Water Storage. *Transactions of the American Geophsical Union* **16**: 519-524.

Todd, D.K. 1980. *Groundwater Hydrology*, 2nd Edition, New York, Wiley.

Valko, P. and Economides, M. 1995. *Hydraulic Fracture Mechanics*. Chichester, Wiley.

Veatch, R.W. 1983a. Overview of Current Hydraulic Fracturing Design and Treatment Technology-Part 1. *J. Pet. Tech.* **35** (4) 677-687.

Veatch, R.W. 1983b. Overview of Current Hydraulic Fracturing Design and Treatment Technology-Part 2. *J. Pet. Tech.* **35** (5) 853-863.

Warpinski, N.R. and Smith, M.B. 1989. Rock Mechanics and Fracture Geometry. *Recent Advances in Hydraulic Fracturing* **12**: 57-80.

APPENDIX

A. 1 Poroelasticity Property

There are two parameters that arise commonly when dealing with poroelastic materials: First, the poroelastic constant, α, is independent of the fluid properties and is defined as (Rice and Cleary 1976):

$$\alpha = \frac{3(\nu_u - \nu)}{B(1-2\nu)(1+\nu_u)} = 1 - \frac{K}{K_s} \quad \text{……(A.1)}$$

where B is Skempton pore pressure coefficient, ν_u is undrained Poisson ratio, ν is drained Poisson ratio, K is drained bulk modulus of elasticity, and Ks bulk modulus of solid phase. The range of poroelastic constant is 0 to 1, but most rocks fall in the range of 0.5 to 1 (Rice and Cleary, 1976).

The second parameter is poroelastic stress coefficient, usually expressed with symbol η, and defined as (Detournay and Cheng 1993):

$$\eta = \alpha \frac{(1-2\nu)}{2(1-\nu)} \quad \text{……...(A.2)}$$

The range of η is 0 to 0.5, and it is independent of the fluid properties.

A. 2 Derivation of Local Fluid Mass Balance Equation

The following is a fracture element with elliptical cross section, whose area is A_1 and A_2 in both ends. Fracture propagates in x direction, with length dx, height H and maximum fracture width w_m.

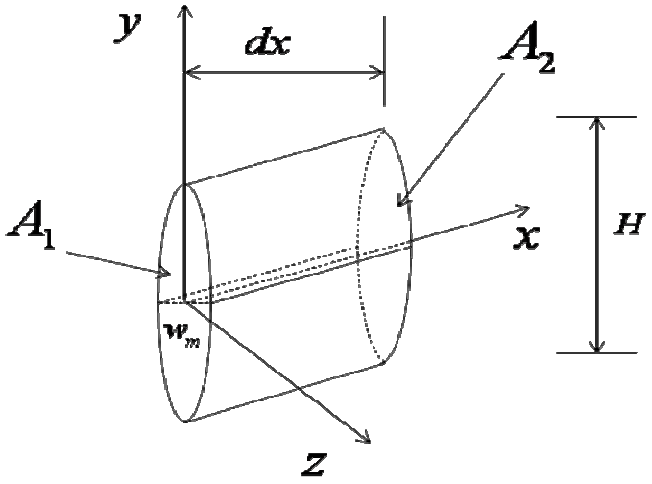

Fig. A.1 A fracture element.

For $dx \to 0$, $A_1 = A_2 = A = \frac{\pi H}{4} w_m(x,t)$. $q(x,t) \cdot H$ is the volume rate of flow through a cross-section (x=constant) of the fracture. And $u \cdot H \cdot dx$ is the fluid volume leak-off rate. $q(x,t)$ is the average flow rate per unit height of fracture, and u is the fluid leak-off velocity accounting for both walls.

For the conservation of volume:

$$q \cdot H \cdot \Delta t + \bar{v} A + u \cdot (H \cdot dx) \cdot \Delta t = q \cdot H \cdot \Delta t + \frac{\partial x}{\partial t} \cdot (\frac{\pi}{4} H \cdot w_m) + u \cdot (H \cdot dx) \cdot \Delta t = 0$$

……...……(A.3)

$$\therefore \frac{\partial q}{\partial x} + \frac{\pi}{4} \frac{\partial w_m}{\partial t} + u = 0 \text{ ……(A.4)}$$

Since the average fracture width is $w = \frac{\pi}{4} w_m$, equation (A.4) is simplified as:

$$\therefore \frac{\partial q}{\partial x} + \frac{\partial w}{\partial t} + u = 0 \quad \text{……(A.5)}$$

A. 3 The Moving Coordinate System

For this type of mesh, the moving coordinate θ is expressed as $\theta = x / L(t)$, which has a range of [0, 1]. This algorithm allows one to use a constant number of nodes to discretize the variable fracture length throughout the solution procedure. The nodes are distributed according to a geometric progression, increasing their density both near the fracture tip and fracture inlet, because of the high pressure and width gradient during fracture propagation and recession. The coordinate θ_i of node i for the first half of the fracture $L/2$ is therefore

$$\theta_i = 0.5 \frac{r^{N-1} - r^{N-i}}{r^{N-1} - 1} \quad \text{…….. (A.6)}$$

while the node distribution for the other half is $1-\theta_i$, where r is the ratio of the progression.

And for this program, 10 to 15 nodal points will be good enough, since too many nodal points don't increase the accuracy that much, and also that will request much longer computing time. To contrast, this paper ran two cases with 11 and 50 nodal points respectively, based on the same input data as listed in Table 2.1. The case with 11 nodal points ran within 30 seconds, while the other one was more than 30 minutes. The results are shown as the following:

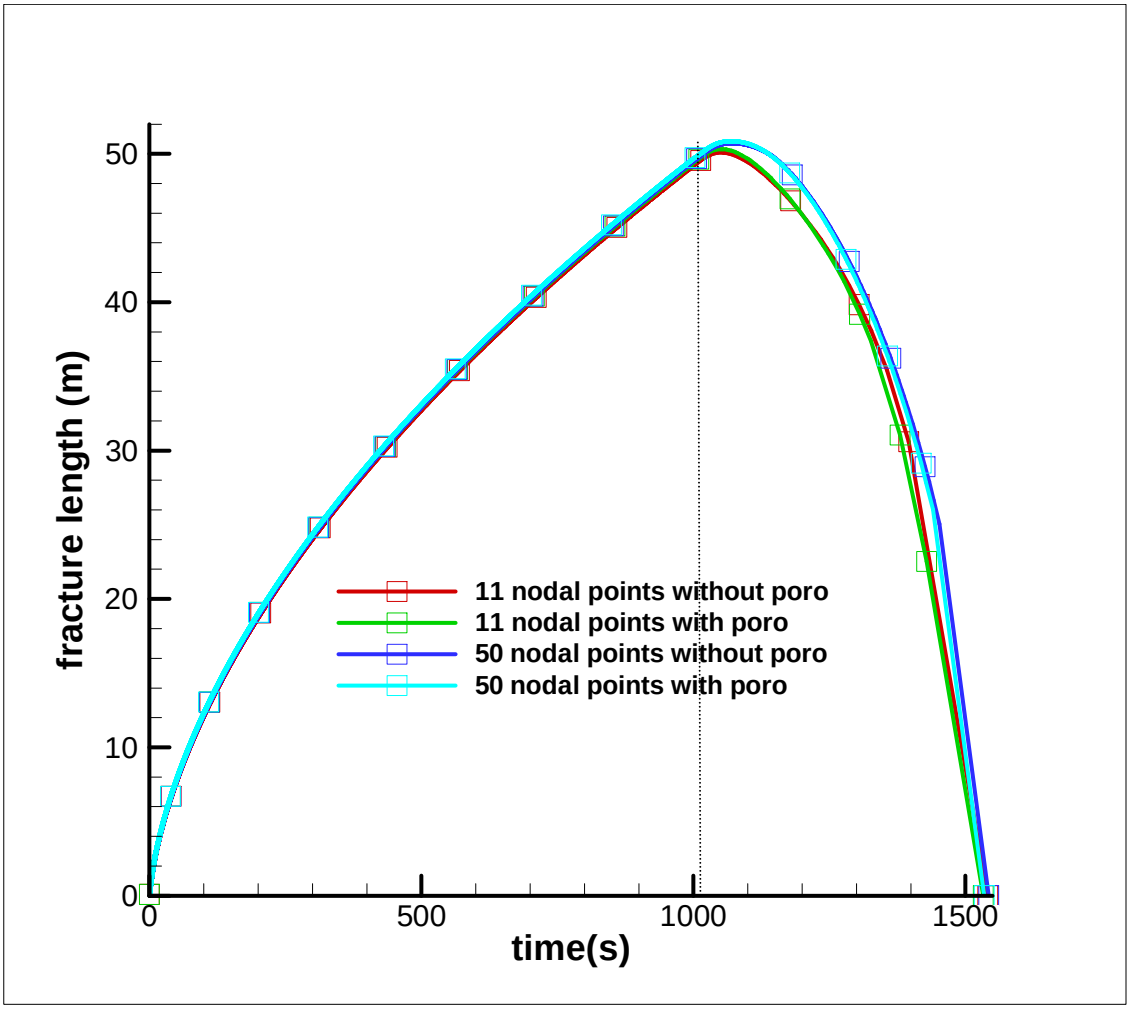

Fig. A.2 Fracture length history with 11 and 50 nodal points.

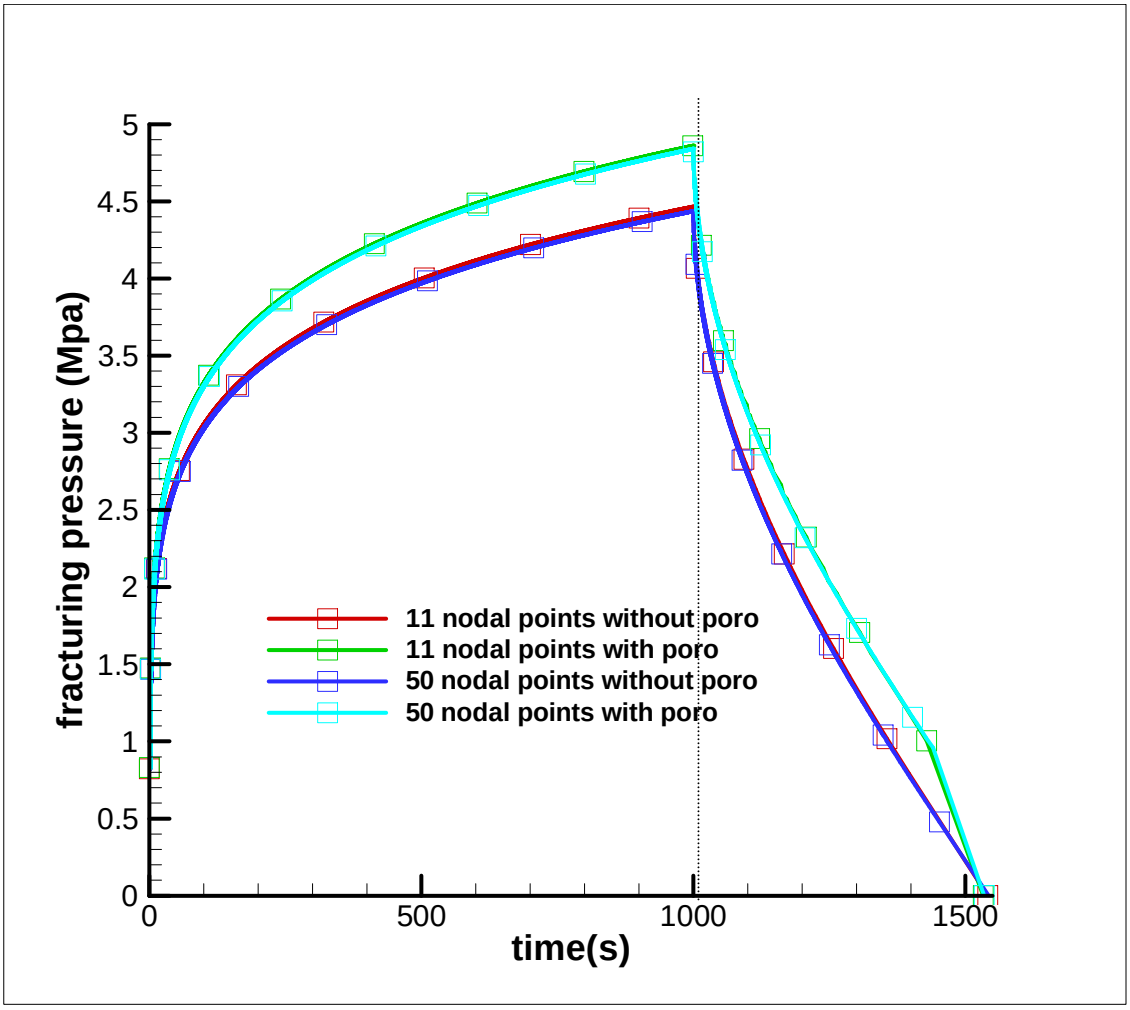

Fig. A.3 Fracturing pressure history with 11 and 50 nodal points.

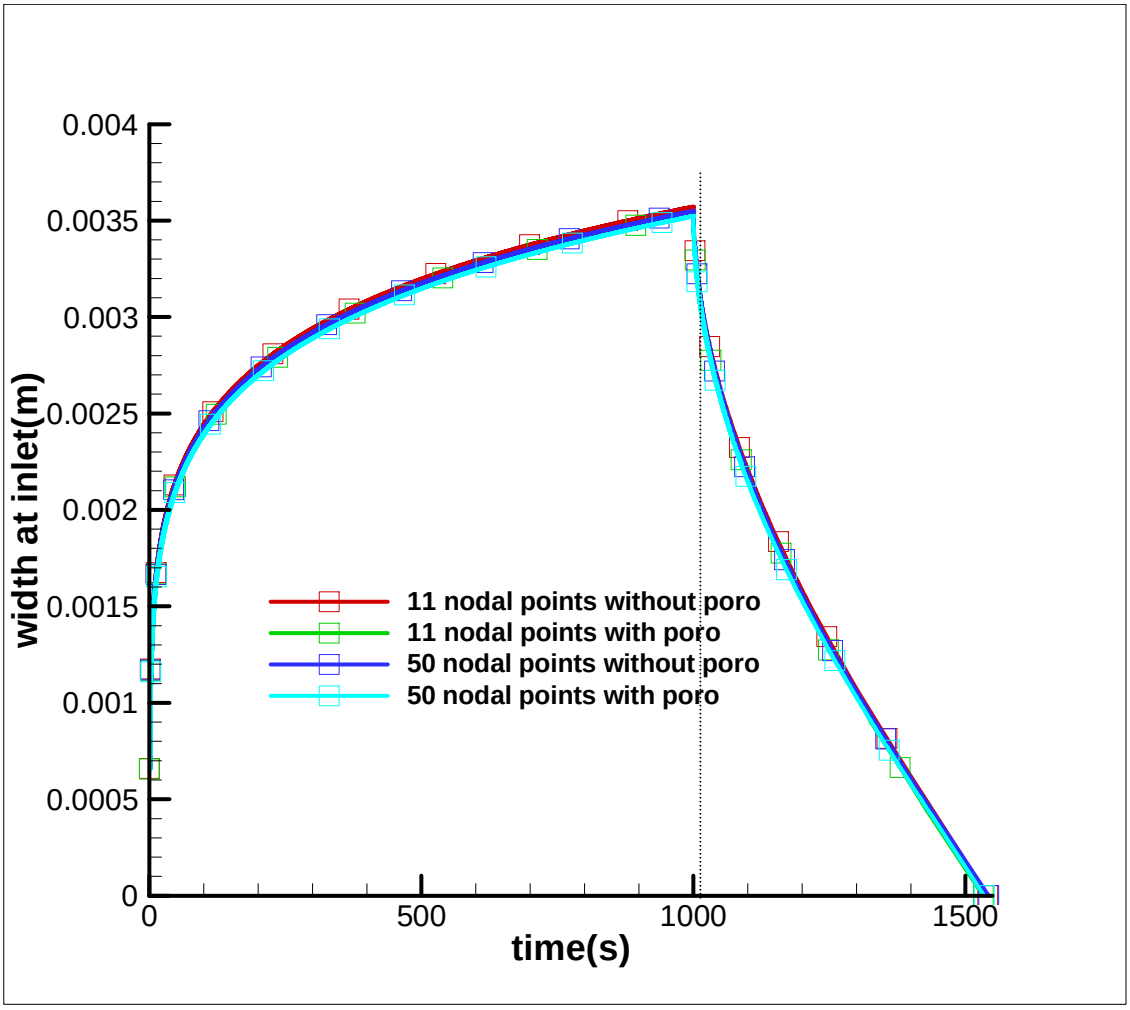

Fig. A.4 Fracture maximum width history with 11 and 50 nodal points.

A. 4 The Fracture Arrival Time

The fracture arrival time $\tau(x)$ is the time when fracture tip arrives at location x. It is the inverse function of fracture length $x = \theta L(t)$. Since there is a corresponding fracture length at every time step; inverse, these time steps, which are the fracture arrival times, corresponding to different fracture lengths. In the moving coordinate system, it is discrete as:

$$\tau(\theta,t)=L^{-1}\left(\theta L(t)\right) \quad \text{……...……..(A.7)}$$

In finite-difference scheme, $\tau_i^{k+1}=L^{-1}(\theta_i L^k)$ is evaluated corresponding to L^k, since the current length L^{k+1} is unknown, by interpolating method based on the fracture arrival time in previous time step τ_i^k.

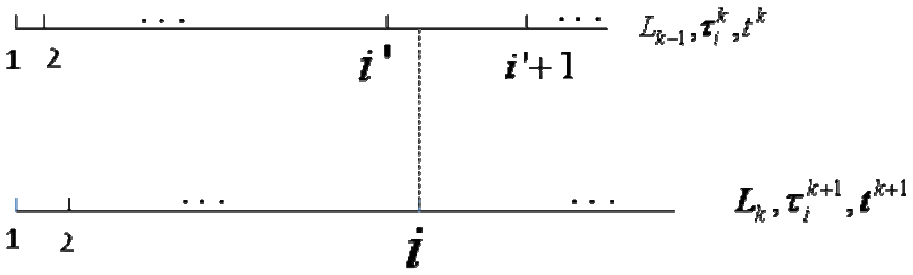

Fig. A.5 Calculation of fracture arrival time by interpolation.

If $\theta_{i'}L^{k-1} \le \theta_i L^k \le \theta_{i'+1}L^{k-1}$, τ_i^{k+1} is linearly interpolated between $\tau_{i'}^k$ and $\tau_{i'+1}^k$:

$$\tau_i^{k+1}=\tau_{i'}^k+\frac{\tau_{i'+1}^k-\tau_{i'}^k}{\theta_{i'+1}L^{k-1}-\theta_{i'}L^{k-1}}(\theta_i L^k-\theta_{i'}L^{k-1}) \quad \text{…….....} \ (A.8)$$

If $L^{k-1} < \theta_i L^k < L^k$, τ_i^{k+1} is linearly interpolated between t^k and t^{k+1}:

$$\tau_i^{k+1}=t^k+\frac{t^{k+1}-t^k}{L^k-L^{k-1}}(\theta_i L^k-L^{k-1}) \quad \text{……..(A.9)}$$

A. 5 Comparison with Published Results for Constant Jeak-off Coefficient Model

To compare the results of this study with the results of Detournay et al. 1990, the plots from the published paper are listed in the following:

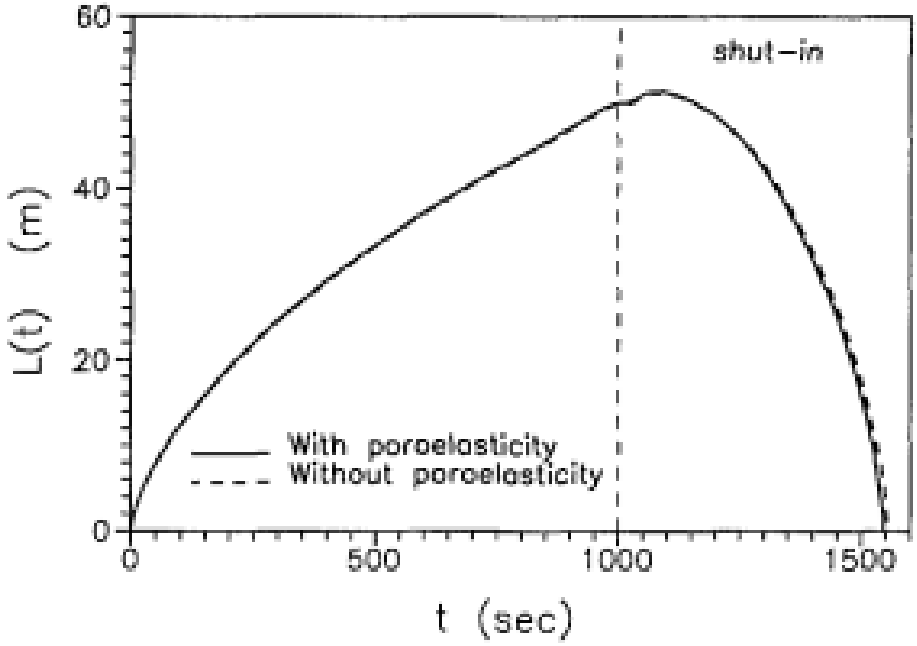

Fig. A.6 Variation of fracture length with time(Detournay et al. 1990).

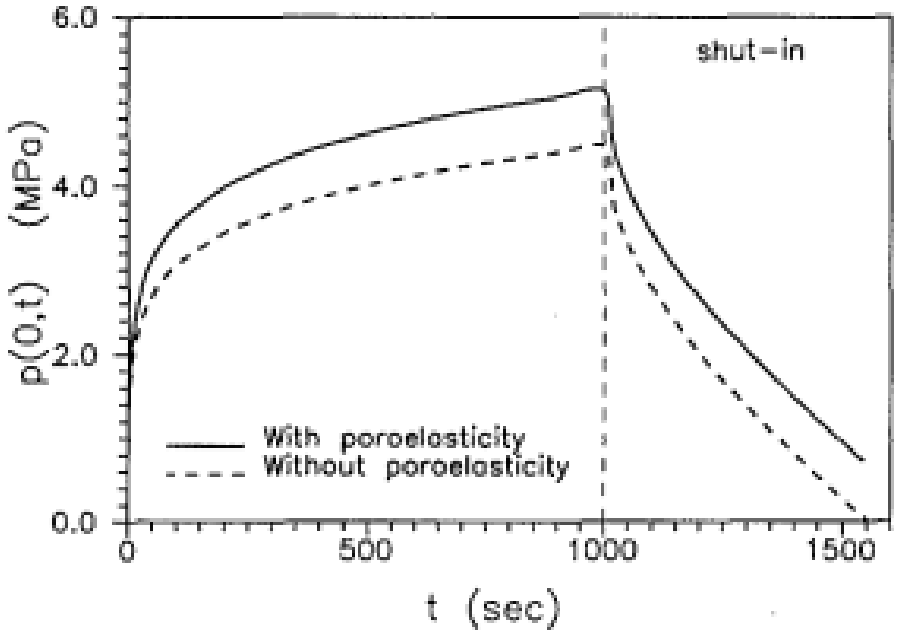

Fig. A.7 Variation of net fracturing pressure with time(Detournay et al. 1990).

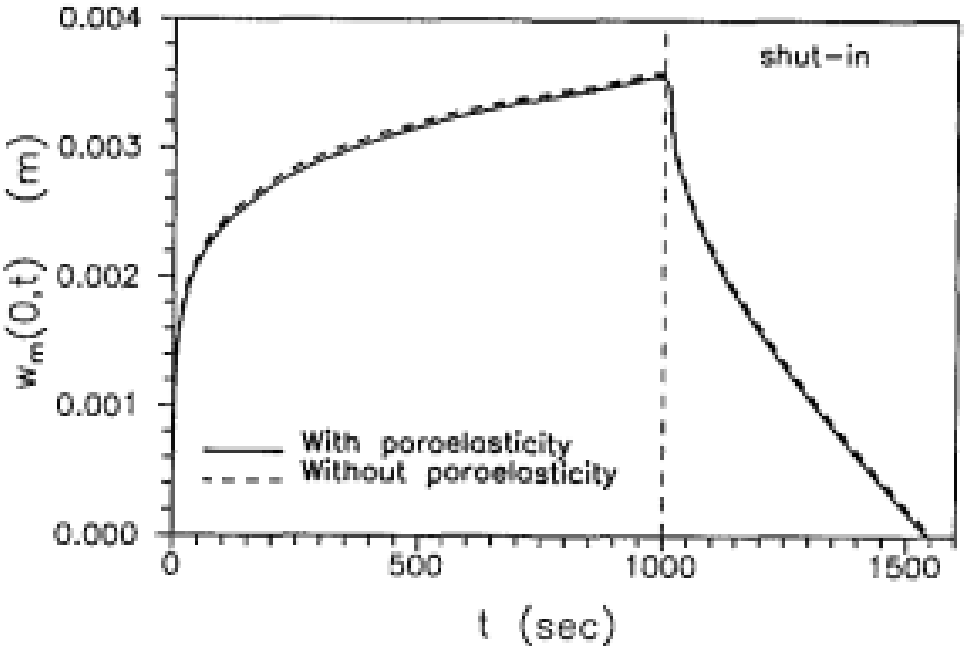

Fig. A.8 Variation of maximum fracture width with time(Detournay et al. 1990).

The following table shows the comparison between the plots above with the Figs. 2.8, 2.9 and 2.10.

Table A.1 Summary of the results from this study and published paper(constant leak-off coefficient)

cases	Maximum fracture length (m)		Maximum $w_m(0,t)$ (m)		Maximum $p(0,t)$ (MPa)		Fracture closure time (sec)	
	$\eta = 0.25$	$\eta = 0$	$\eta = 0.25$	$\eta = 0$	$\eta = 0.25$	$\eta = 0$	$\eta = 0.25$	$\eta = 0$
This study	50.0	50.0	0.00358	0.00358	4.95	4.5	1533	1533
Published paper	52.0	52.0	0.0036	0.0036	5.2	4.5	1550	1550

From Table A.1, it shows that the simulation results of the net fracturing pressure, the fracture length, maximum width and the fracture closure time are close to the published paper, with the differences less than 5%.

A. 6 Pressure Dependent Leak-off Equation

The flow of the fracturing fluid (assumed Newtonian and incompressible) into the porous formation (fluid leakoff) is assumed to be linear and perpendicular to the face of the fracture. The local volumetric rate response of the fracture to a unit step pressure on an element dz along the fracture height H , and accounting for the two sides of the fracture from Carslaw and Jaeger (Carslaw and Jaeger 1956) is written as:

$$v''(t-\tau(x)) = \frac{2\kappa dz}{\sqrt{\pi c(t-\tau(x))}} \quad \text{.....(A.10)}$$

where κ is the mobility coefficient defined as the ratio of the permeability k to the viscosity μ, t is the time at which the volume rate response is evaluated, and $\tau(x)$ is the time at a given location x on the fracture face at which the pressure step was applied. The diffusivity coefficient c can be approximated by the known expression:

$$c = \frac{\kappa}{\phi C_p} \qquad \text{(A.11)}$$

where ϕ is the porosity of the rock, and C_p is the compressibility of the pore and pore fluid system. Since we assume that the PKN fracture propagates at a constant height (confined between the barriers), then H is independent of time t. The total fluid volume $v(t)$ contributed by an element dz is obtained as:

$$v(t) = \int_{\tau(x)}^{t} \frac{2\kappa p(\tau')dz}{\sqrt{\pi c(t-\tau')}} d\tau' \qquad \text{(A.12)}$$

where $p(\tau')$ is the history of uniform pressures applied on the surface of the fracture between time $\tau(x)$ and t and where $p(x,t) = p_f(x,t) - \sigma_o$

Integrating by parts the above integral, we obtain:

$$v(t) = \frac{2\kappa}{\sqrt{\pi c}} \left[-2p(\tau')dz\sqrt{t-\tau'} \Big|_{\tau(x)}^{t} + \int_{\tau(x)}^{t} 2p'(\tau')dz\sqrt{t-\tau'}d\tau' \right] \qquad \text{(A.13)}$$

$$v(t) = \frac{2\kappa}{\sqrt{\pi c}} \left[2p(\tau(x))dz\sqrt{t-\tau(x)} + 2\int_{\tau(x)}^{t} p'(\tau')dz\sqrt{t-\tau'}d\tau' \right] \qquad \text{(A.14)}$$

The local value of the flow rate, q, that corresponds to the rate at which the fluid is invading the reservoir, can be written as:

$$q_l = \frac{dv}{dt} \quad \text{.....(A.15)}$$

and we can write

$$q_l = \frac{2\kappa p(\tau(x))dz}{\sqrt{\pi c\left(t-\tau(x)\right)}} + \int_{\tau(x)}^{t} \frac{2\kappa p'(\tau')dz}{\sqrt{\pi c\left(t-\tau'\right)}} d\tau' \quad \text{.....(A.16)}$$

Since $\tau(x)$ is the time at a given location x, this is equivalent to the arrival time of the fracture tip at that section of the formation, the pressure at that point needed for the fracture opening is equal to the in situ effective stress (assuming rack strength and thus toughness in tension as negligible)

$$p(\tau(x)) = \sigma_o - p_o \quad \text{.....(A.17)}$$

In this case the fracture is assumed to open along the formation height instantaneously, and the individual pressure histories for each element dz is assumed to start at the same time $\tau(x)$. The summation of the element dz along the fracture height (to calculate the total fluid leakoff at a given cross section), will result in replacing dz by H in the above expression and we define the fluid leakoff velocity $u = q_l / H$ as follows

$$u = \frac{2\kappa(\sigma_o - p_o)}{\sqrt{\pi c(t-\tau(x))}} + \frac{2\kappa}{\sqrt{\pi c}} \int_{\tau(x)}^{t} \frac{\partial p(x,t')}{\partial t'} \frac{1}{\sqrt{t-t'}} dt' \quad \text{.....(A.18)}$$

where p is the 'net stress' defined as $p = p_f - \sigma_o$, σ_o is the minimum in situ stress, p_o is the virgin pore pressure.

A. 7 Comparison with Published Results for Pressure-dependent Leak-off

To compare the results of this study with the results of Abousleiman 1991, the plots from his dissertation are listed in the following:

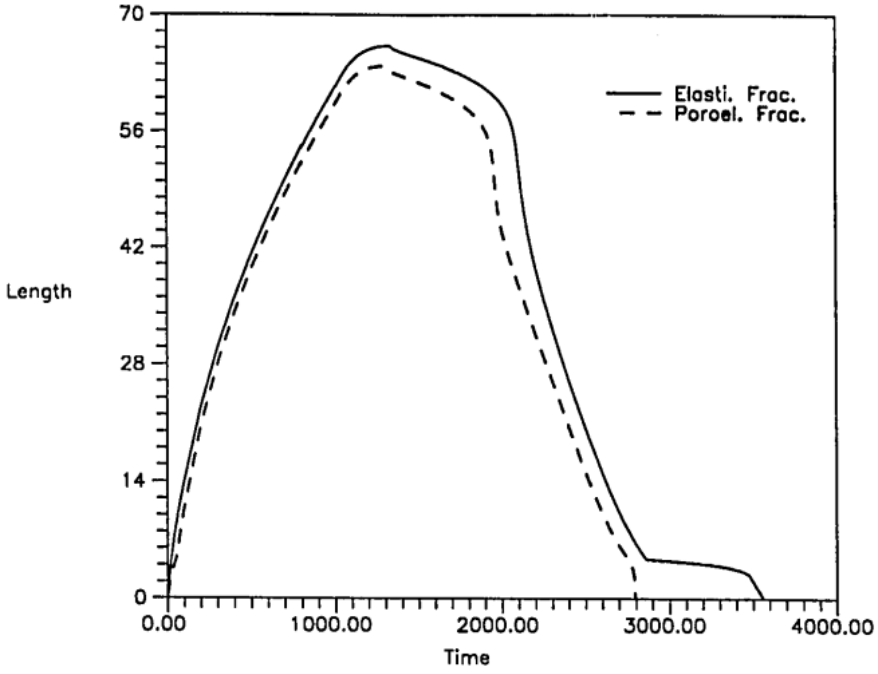

Fig. A.9 Variation of fracture length with time(Abousleiman 1991).

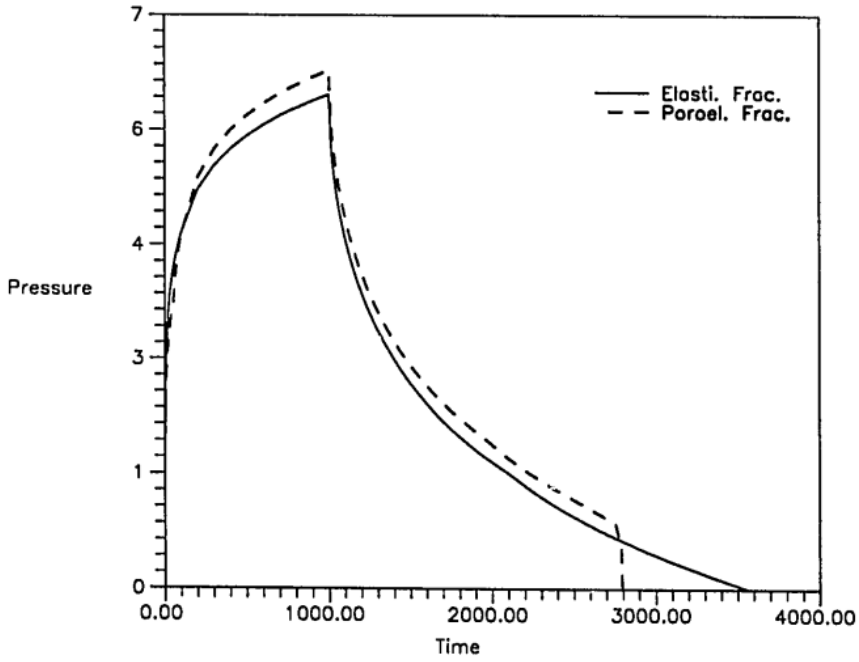

Fig. A.10 Variation of net fracturing pressure with time(Abousleiman 1991).

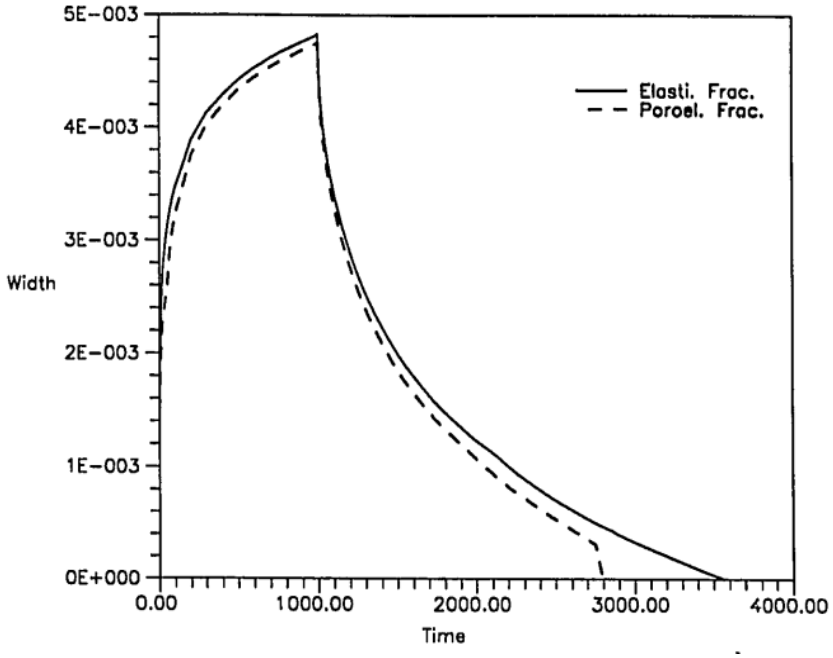

Fig. A.11 Variation of maximum fracture width with time(Abousleiman 1991).

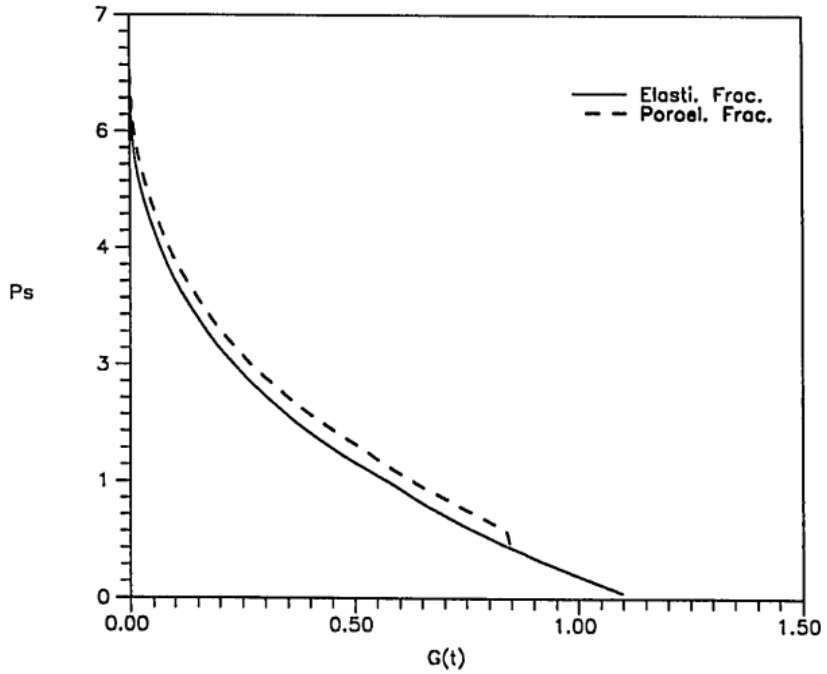

Fig. A.12 The G-function for pressure dependent leak-off case(Abousleiman 1991).

Compare the plots above with the Figs. 3.2, 3.3 and 3.4, and the results are listed as follow:

Table A.2 Summary of the results from this study and published paper(pressure-dependent leak-off)

cases	Maximum fracture length (m)		Maximum $w_m(0,t)$ (m)		Maximum $p(0,t)$ (MPa)		Fracture closure time (sec)	
	$\eta = 0.15$	$\eta = 0$	$\eta = 0.15$	$\eta = 0$	$\eta = 0.15$	$\eta = 0$	$\eta = 0.15$	$\eta = 0$
This study	55.3	59.2	0.00453	0.00474	6.97	5.98	4436	6981
disserta-tion	61.5	66.0	0.00475	0.00481	6.37	6.21	2800	3550

From Table A.2, it shows that the simulation results of the net fracturing pressure, the fracture length, and maximum width are different from Abousleiman's dissertation, with the differences around 10%. I got smaller fracture length and width for both with and without poroelasticity effect simulation, and the maximum fracturing pressure difference between these two situations is larger. While the fracture closure time is much larger than Abousleiman's result.

A. 8 Upwind Scheme Used for Width Discrete Equation

In computational fluid dynamics, upwind schemes denote a class of numerical discretization methods for solving hyperbolic partial differential equations. Upwind schemes use an adaptive or solution-sensitive finite difference stencil to numerically simulate more properly the direction of propagation of information in a flow field. The

upwind schemes attempt to discretize hyperbolic partial differential equations by using differencing biased in the direction determined by the sign of the characteristic speeds. Historically, the origin of upwind methods can be traced back to the work of Courant, Isaacson, and Rees who proposed the CIR method (Courant et al. 1952).

To illustrate the method, consider the following one-dimensional linear wave equation:

$$\frac{\partial u}{\partial t}+a\frac{\partial u}{\partial x}=0 \quad \text{.....(A.19)}$$

The first-order upwind scheme of the above equation is:

$$\begin{aligned}&(1)\ \frac{u_i^{n+1}-u_i^n}{\Delta t}+a\frac{u_i^n-u_{i-1}^n}{\Delta x}=0 \quad for\ \ a>0\\ &(2)\ \frac{u_i^{n+1}-u_i^n}{\Delta t}+a\frac{u_{i+1}^n-u_i^n}{\Delta x}=0 \quad for\ \ a<0\end{aligned} \quad \text{.....(A.20)}$$

similarly, equation (2.20) would be written as:

$$\frac{\partial w}{\partial t}-\frac{\theta \dot{L}}{L}\frac{\partial w}{\partial \theta}+\frac{1}{L}\frac{\partial q}{\partial \theta}+u=0 \quad \text{.....(A.21)}$$

During the fracture propagation, according to the upwind scheme, since $\frac{\theta \dot{L}}{L}>0$, equation (A.21) can be expressed as:

$$\begin{aligned}&\frac{w_i^{k+1}-w_i^k}{\Delta t^{k+1}}-\left(\frac{\theta_i \dot{L}^k}{L^k}\frac{w_{i+1}^k-w_i^k}{\theta_{i+1}-\theta_i}\right)+\frac{2}{L^k}\left(\frac{q_{i+1/2}^k-q_{i-1/2}^k}{\theta_{i+1}-\theta_{i-1}}\right)+u_i^k=0;\ i=2,N\text{-}2 \Rightarrow\\ &w_i^{k+1}=w_i^k+\Delta t^{k+1}\left[\left(\frac{\theta_i \dot{L}^k}{L^k}\frac{w_{i+1}^k-w_i^k}{\theta_{i+1}-\theta_i}\right)-\frac{2}{L^k}\left(\frac{q_{i+1/2}^k-q_{i-1/2}^k}{\theta_{i+1}-\theta_{i-1}}\right)-u_i^k\right];\ i=2,N\text{-}2\end{aligned} \quad \text{...(A.22)}$$

At node $n-1$ the forward difference formula for $\frac{\partial w}{\partial \theta}$ is unstable during simulation and

a backward difference formula is used instead:

$$w_{N-1}^{k+1} = w_{N-1}^{k} + \Delta t^{k+1}\left[\left(\frac{\theta_{N-1}\dot{L}^{k}}{L^{k}}\frac{w_{N-1}^{k} - w_{N-2}^{k}}{\theta_{N-1} - \theta_{N-2}}\right) - \frac{2}{L^{k}}\left(\frac{q_{N-1/2}^{k} - q_{N-3/2}^{k}}{\theta_{N} - \theta_{N-2}}\right) - u_{N-1}^{k}\right];\ i = N\text{-}1$$

……(A.23)

At the first node, equation (A.23) is simplified as

$$w_{1}^{k+1} = w_{1}^{k} - \Delta t^{k+1}\left[\frac{2}{L^{k}}\frac{q_{3/2}^{k} - q_{o}^{k}}{\theta_{2}} + u_{1}^{k}\right]\text{…...……..(A.24)}$$

and the last node, it's assumed that

$$w_{N}^{k+1} = 0\text{ ……..(A.25)}$$

For a receding fracture, since $\frac{\theta \dot{L}}{L} < 0$, equation (A.21) can be expressed as:

$$\frac{w_{i}^{k+1} - w_{i}^{k}}{\Delta t^{k+1}} - \left(\frac{\theta_{i}\dot{L}^{k}}{L^{k}}\frac{w_{i}^{k} - w_{i-1}^{k}}{\theta_{i} - \theta_{i-1}}\right) + \frac{2}{L^{k}}\left(\frac{q_{i+1/2}^{k} - q_{i-1/2}^{k}}{\theta_{i+1} - \theta_{i-1}}\right) + u_{i}^{k} = 0;\ i = 2, N\text{-}1 \Rightarrow$$

$$w_{i}^{k+1} = w_{i}^{k} + \Delta t^{k+1}\left[\left(\frac{\theta_{i}\dot{L}^{k}}{L^{k}}\frac{w_{i}^{k} - w_{i-1}^{k}}{\theta_{i} - \theta_{i-1}}\right) - \frac{2}{L^{k}}\left(\frac{q_{i+1/2}^{k} - q_{i-1/2}^{k}}{\theta_{i+1} - \theta_{i-1}}\right) - u_{i}^{k}\right];\ i = 2, N\text{-}1 \quad \text{….(A.26)}$$

The equations of the first and last node during recession are the same as equation (A.24) and (A.25).

VITA

Name:	Jing Xiang
Permanent Address:	Harold Vance Department of Petroleum Engineering, 3116 TAMU, College Station, TX 77843-3116
Email Address:	jing.xiang6@gmail.com
Education:	Texas A&M University, College Station, Texas, USA M.S., Petroleum Engineering, December 2011 Chinese University of Petroleum, Beijing, China B.S., Petroleum Engineering, June 2008
Affiliation:	Society of Petroleum Engineers